KEK Report 2007-1
June 2007
H

Measurement of Dijet Production in Diffractive Deep Inelastic Scattering at HERA

Toshinari Tawara

Department of Physics, University of Tokyo
7-3-1 Hongo, Bunkyo-ku, Tokyo 113-0033 Japan

High Energy Accelerator Research Organization

KEK Reports are available from:

High Energy Accelerator Research Organization (KEK)
1-1 Oho, Tsukuba-shi
Ibaraki-ken, 305-0801
JAPAN

Phone: +81-29-864-5124
Fax: +81-29-864-4602
E-mail: irdpub@mail.kek.jp
Internet: http://www.kek.jp

序文

この論文は俵寿成氏が東京大学大学院理学系研究科物理学専攻の在学中に行った研究をまとめたものであり、この研究により同氏は 2007 年 3 月学位を取得した。

ドイツ DESY 研究所での電子・陽子衝突装置 HERA を用いた国際共同実験 ZEUS において、電子と陽子の深非弾性散乱の中から回折反応事象を選択した上でジェット生成断面積を測定した論文である。

HERA でハードな電子・陽子回折反応が観測されて以来、回折反応を摂動論的量子色力学のモデルで説明する研究が急激に進んだ。深非弾性散乱の実験データからは回折反応に関与するクォークの振舞いを精度よく測定できていたが、グルーオンの関与を決めるには大きな不定性があった。この論文では主状態に 2 つ以上のジェットが出る事象を選択することによってグルーオンへの感度をあげ、新しい摂動的量子色力学の計算との比較を通して、回折反応への陽子内グルーオンの関与が大きいことを明らかにした。

この結果は ZEUS 実験グループの論文として公表するが、そこでは解析の詳細に関して記述することができない。俵氏の開発した多くの解析手法と系統誤差の見積方法は、今後の研究を進める上で重要であるので、ここに同氏の論文を学術資料として広く公開する。

2007 年 6 月

素粒子原子核研究所教授

徳宿　克夫

Measurement of Dijet Production in Diffractive Deep Inelastic Scattering at HERA

Toshinari Tawara

Department of Physics, University of Tokyo
7-3-1 Hongo, Bunkyo-ku, Tokyo 113-0033 Japan

Abstract

The dijet production in diffractive deep inelastic scattering, $ep \to e'p$ jet1 jet2 X', has been measured with the ZEUS detector at HERA using an integrated luminosity of 65.2 pb^{-1}. This process is sensitive to the partonic structure of the diffractive exchange between the proton and the virtual photon emitted from the electron. The dijet cross section for such processes has been measured for virtualities of the exchanged boson, $5 < Q^2 < 100$ GeV^2 and photon-proton centre-of-mass energies, $100 < W < 250$ GeV. The jets were identified using the inclusive k_T algorithm in the γ^*-p frame. The two highest transverse energy jets identified in each event were required to satisfy $E^*_{T,\mathrm{jets}} > 5$ and 4 GeV, respectively in the pseudorapidity range $-3.5 < \eta^*_{\mathrm{jets}} < 0$, as measured in the γ^*-p frame. The differential cross sections have been measured and compared to the predictions from leading order Monte Carlo models and next-to-leading order QCD calculations based on recent diffractive parton densities extracted from inclusive diffractive deep inelastic scattering data.

Contents

Chapter 1

Introduction

Today, we consider that there are four different kinds of fundamental forces in nature, namely, gravitation, electromagnetism, week interaction, and strong interaction. The strong interaction is the force between the quarks (anti-quarks) and the gluons in hadrons such as protons, neutrons, and pions. In the standard model, it is successfully described by the Quantum Chromodynamics (QCD).

The inside of hadrons has been probed by high energy leptons, (electrons, muons, or neutrinos). As the energy and the momentum transfer increase, the scattering becomes more and more inelastic. In the end of the 1960s, Deep-Inelastic Scattering (DIS) process was observed in an electron-proton experiment at SLAC. The result of this experiment indicated that there were point-like charges (partons) in the proton. Combining with the results of neutrino scattering experiments, the parton was identified as the quark. Thus, quark-parton picture of the proton has started. The cross section of DIS of a proton and a lepton is described with a convolution of universal parton density functions (PDFs) of the proton and hard scattering cross sections between the partons and the lepton. The hard scattering of the proton, such as the lepton pair production (Drell-Yan process), has also been successfully explained in this framework as the incoherent sum of the scattering of the partons.

On the other hand, the soft interaction in the proton-proton collision at high energy cannot be explained by the quark parton model. In small angle scattering, a pattern similar to the diffraction in the optical light is observed, and hence it is analogically called diffraction.

In the Regge theory which considers the soft interaction by the superposition of the exchange of various particles [1], the total cross section of the hadron-hadron interaction (σ_{tot}) is a power of the squared centre-of-mass energy (s) by the optical theorem; $\sigma_{\mathrm{tot}} \sim s^{\alpha(0)-1}$, where $\alpha(0)$ is the intercept of the trajectory of the exchange particles.

In the hadron-hadron interaction, the total cross section gently increases as a function of centre-of-mass energy at high energy. This shows that the intercept of the trajectory of

the dominant exchange particle is about 1. The exchange particle corresponding to this trajectory is not found, but is called the pomeron trajectory.

Many feature of diffractive scattering was explained with the pomeron trajectory. After a compilation of various hadron-hadron interactions, A. Donnachie and P.V. Landshoff [2] extracted the pomeron trajectory $\alpha_{I\!P}(t) = 1.08 + 0.25t$, where t is the squared momentum transfer. On the other hand, it is also shown experimentally that, the diffractive scattering looks two steps; first the proton emits an exchange particle, and then the particle, often called a pomeron, interacts. So, the framework that treats pomerons as a quasi-particle was developed. G. Ingelman and P.E. Schlein [3] pushed further by proposing that the pomeron has a partonic structure when hard scattering is involved.

In 1988, the first jet signal in the diffractive scattering was observed in $p\overline{p}$ interactions with the $\sqrt{s} = 630$ GeV by UA8 experiment [4]. The production cross sections of jets whose transverse energy was between 5 and 13 GeV were measured. Adapting the Ingelman-Schlein model, the results indicated that the parton distribution in the pomeron was very hard. A parton might carry the entire momentum of the pomeron.

The parton structure in the pomeron can be much well measured from diffractive DIS at HERA. In 1992, the first events with a large rapidity gap between hadronic final states and the proton remnant were observed in DIS of electron and proton at $\sqrt{s} = 296$ GeV by both H1 and ZEUS experiments [5, 6]. The amount of such kind of events was $\sim 10\%$ in all DIS events, and almost independent to Q^2. Diffractive process can be explained that the interaction between the virtual photon and a colourless object (pomeron) emitted from the proton. It was proven that the diffractive cross section of DIS factorizes into diffractive PDFs and the hard scattering [7] as like the inclusive DIS.

Recently, several diffractive PDFs have been extracted by fitting H1 and ZEUS results of the inclusive diffractive DIS data. From these results, the gluon seems to be the dominant component. However, the gluon distributions for each result are quite different depending on which inclusive diffractive DIS data to use. Therefore, it is important to constraint the gluon distribution with different types of reactions.

Dijet is produced by the boson gluon fusion (BGF) and QCD compton (QCDC) processes. The BGF process in diffraction is the interaction between a gluon emitted from the pomeron and the virtual photon emitted from the electron. Thus, the BGF process is directly related to the gluon in the pomeron. The measurement of the dijet cross section in diffractive DIS gives important information on the gluon contents of the pomeron through a comparison with the prediction of the next-to-leading order (NLO) QCD calculation which include the BGF and QCDC processes. In this thesis, the dijet cross section is measured as functions of various kinematic variables. Especially, it is important to measure the dijet cross section as a function of the longitudinal momentum fraction of the parton in the pomeron. This has a large sensitivity to the parton distribution in the pomeron.

The structure of this thesis is the following. In Chapter 2, kinematics in diffraction in DIS are introduced, the feature of diffraction at HERA, the theory of diffraction and the aim of this analysis are explained. In Chapter 3, HERA accelerator and ZEUS experimental setup used in this analysis are given. In Chapter 4, Monte Carlo simulation programs used in this analysis are given. In Chapter 5, the procedure of event reconstruction and event selection is explained. In Chapter 6, the procedure of the cross section measurement is given, and the diffractive cross sections as functions of various kinematic variables are presented. The systematic uncertainties are also estimated. In Chapter 7, the procedure of NLO calculation in diffraction is given, and the comparison of data with NLO prediction with various diffractive PDFs is given and explained in detail. Finally, in Chapter 8, the conclusion of this thesis is given.

Chapter 2

Diffraction in deep-inelastic scattering

This chapter describes the kinematics of diffraction in deep-inelastic scattering (DIS), the feature of diffraction at HERA, the theory of diffraction and the aim of this analysis.

2.1 Deep-inelastic scattering

Figure 2.1 shows the diagram of the inclusive DIS process $ep \to eX$. The four-vectors of the momentum of the incoming lepton (k) and the proton (P) can be written as;

$$\begin{aligned} k &= (E_e, 0, 0, -E_e) \ , \\ P &= (E_p, 0, 0, E_p) \ , \end{aligned}$$

where the E_e is the initial electron energy and E_p is the initial proton energy. The mass term is neglected. Kinematics of the DIS process are described by variables, Q^2, x, y, s, and W^2. These variables are defined by the following formula;

$$Q^2 \equiv -q^2 = -(k - k')^2 \ , \tag{2.1}$$

$$x \equiv \frac{Q^2}{2P \cdot q} \ , \tag{2.2}$$

$$y \equiv \frac{P \cdot q}{P \cdot k} \ , \tag{2.3}$$

$$s \equiv (k + P)^2 \ , \tag{2.4}$$

$$W^2 \equiv (q + P)^2 \ , \tag{2.5}$$

where k' is the four-momentum of the final lepton and q ($\equiv k - k'$) is the four-momentum transfer. Q^2 is the virtuality of the exchanged photon. $\sqrt{s}$ is the centre-of-mass energy of the ep system. W is the centre-of-mass energy of the virtual photon-proton system.

x, y are the Bjorken scaling variables. x corresponds to the proton momentum fraction carried by the struck quark in the naive quark parton model. y is called the inelasticity of the interaction.

s is described by the E_e and E_p as the following;

$$s = 4E_eE_p \, . \tag{2.6}$$

Once the s is fixed by E_e and E_p, only two variables among these kinematic variables are independent because of the following relations;

$$Q^2 = sxy \, , \tag{2.7}$$
$$W^2 = sy - Q^2 \, . \tag{2.8}$$

The inclusive differential cross section in DIS is described by any two variables. With x and Q^2, it is written as;

$$\frac{d^2\sigma}{dxdQ^2} = \frac{2\pi\alpha^2}{xQ^4}\Big([1+(1-y)^2]F_2(x,Q^2) - y^2F_L(x,Q^2)\Big) \, , \tag{2.9}$$

where α is the fine structure constant, F_2 are F_L are called the structure functions which contain the information of the internal structure of the proton as described in Section 2.2.

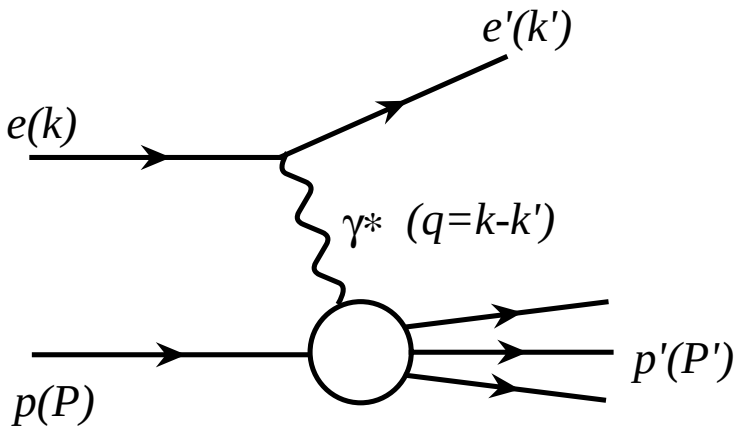

Figure 2.1: Diagram of Deep-inelastic scattering

2.2 Quark parton model

In the naive quark parton model where the proton is made from "free" moving quarks, anti-quarks and gluons, the proton structure functions are directly connected to the mo-

mentum distribution of the quark and anti-quark;

$$F_2(x) = \sum_i e_i^2 x(q_i(x) + \overline{q}_i(x)) \,, \tag{2.10}$$

$$F_L(x) = 0 \,, \tag{2.11}$$

where e_i is the charge and $q_i(x)$, $\overline{q}_i(x)$ are the momentum distribution of quarks and anti-quarks with flavor i in the proton, respectively. If the quarks move freely, F_2 has dependence on only x and is independent to Q^2. This is called the "Bjorken scaling".

2.3 DGLAP equation

When the interaction between the quarks are taken into account, $q_i(x)$, $\overline{q}_i(x)$ are no longer constant as Q^2 changes. Indeed, it was experimentally observed that F_2 is slowly changing with Q^2 (so called "Bjorken scaling violation"). In the perturbative quantum chromodynamics (QCD), the Dokshitzer - Gribov - Lipatov - Altarelli - Parisi (DGLAP) evolution equation [8–10] describes how the parton density functions (PDFs) evolve with Q^2. The cross section of ep collision is still described as a convolution of the PDFs in the proton ($f_{i/p}$) and the cross section between the parton and the electron ($\hat{\sigma}_{ie}$). This relation is denoted as following;

$$\sigma_{ep} = \sum_{i=\text{partons}} f_{i/p} \otimes \hat{\sigma}_{ie} \,. \tag{2.12}$$

Or, reversely, the PDFs can be extracted from the experimental data by fitting to the perturbative QCD calculation.

2.4 Feature of diffraction

DIS processes can be considered as collisions between the proton and the virtual photon (γ^*) emitted from the electron (i.e. $\gamma^* p \to X.$), as seen in Figure 2.3. Among such processes, the events are called diffractive processes where the final state particles are separated to two objects in the rapidity space, $\gamma^* p \to XY$, where the system X is the photon dissociated system and Y is the proton dissociated system. Such characteristics indicate that an object with colour-neutral state is exchanged between the system X and Y.

The diffractive processes are characterized by a large rapidity gap between X and Y, and small mass of the system X and Y with respect to W. The produced hadrons are sorted in rapidity in the photon-proton centre-of-mass system. The largest rapidity gap between two neighboring particles then separates the system X and Y.

Figure 2.2 shows the display of a non-diffractive DIS event and a diffractive event taken by the ZEUS detector. In the upper figure, there are energy deposits up to the very forward part of the CAL and no large rapidity gap down to the current jet. On the other hand, in the lower figure, there is no energy deposit around the forward beam pipe and hence there is a large rapidity gap between the hadronic particles detected in the calorimeter and the unseen system Y escaped in the forward beam pipe.

At present, these are many accumulation of the experimental results that the diffractive process can be regarded as a two step processes. First, a colour neutral quasi-particle is emitted from proton and next it interacts with partons. G. Ingelman and P. E. Schlein propose a model that the exchanged particle, called a pomeron ($I\!P$), has a partonic structure [3]. In this thesis, this model is referred as the resolved pomeron model. In this framework, the cross section measurement of diffractive DIS gives information on the partonic structure of the pomeron.

2.5 Kinematics of diffraction

Figure 2.3 shows the inclusive diffractive DIS process $ep \to eXY$. The event is called proton dissociative process if the system Y is dissociated into the low mass. On the other hand, when system Y is a single proton, it is called the photon dissociative diffraction, which is the main subject in this thesis. Since there are two hadronic system in the final state, three more kinematic variables, t, $x_{I\!P}$, β, are needed to describe the photon dissociative process, in addition to the two variables (such as x, Q^2) already introduced for inclusive DIS.

The squared proton four-momentum transfer t is defined as the following;

$$t \equiv (P - P')^2 \,, \tag{2.13}$$

where P' is the four-momentum of the outgoing proton.

The variable $x_{I\!P}$ is defined as the following;

$$\begin{aligned} x_{I\!P} &\equiv \frac{q \cdot (P - P')}{q \cdot P} \\ &= \frac{M_X^2 + Q^2 - t}{W^2 + Q^2 - m_p^2} \\ &\approx \frac{M_X^2 + Q^2}{W^2 + Q^2} \,, \end{aligned} \tag{2.14}$$

where m_p and M_X are the invariant mass of the proton and the hadronic system X respectively. The mass of the electron m_e has been neglected in the approximation. In the resolved pomeron model, $x_{I\!P}$ corresponds to the longitudinal proton momentum fraction carried by the pomeron.

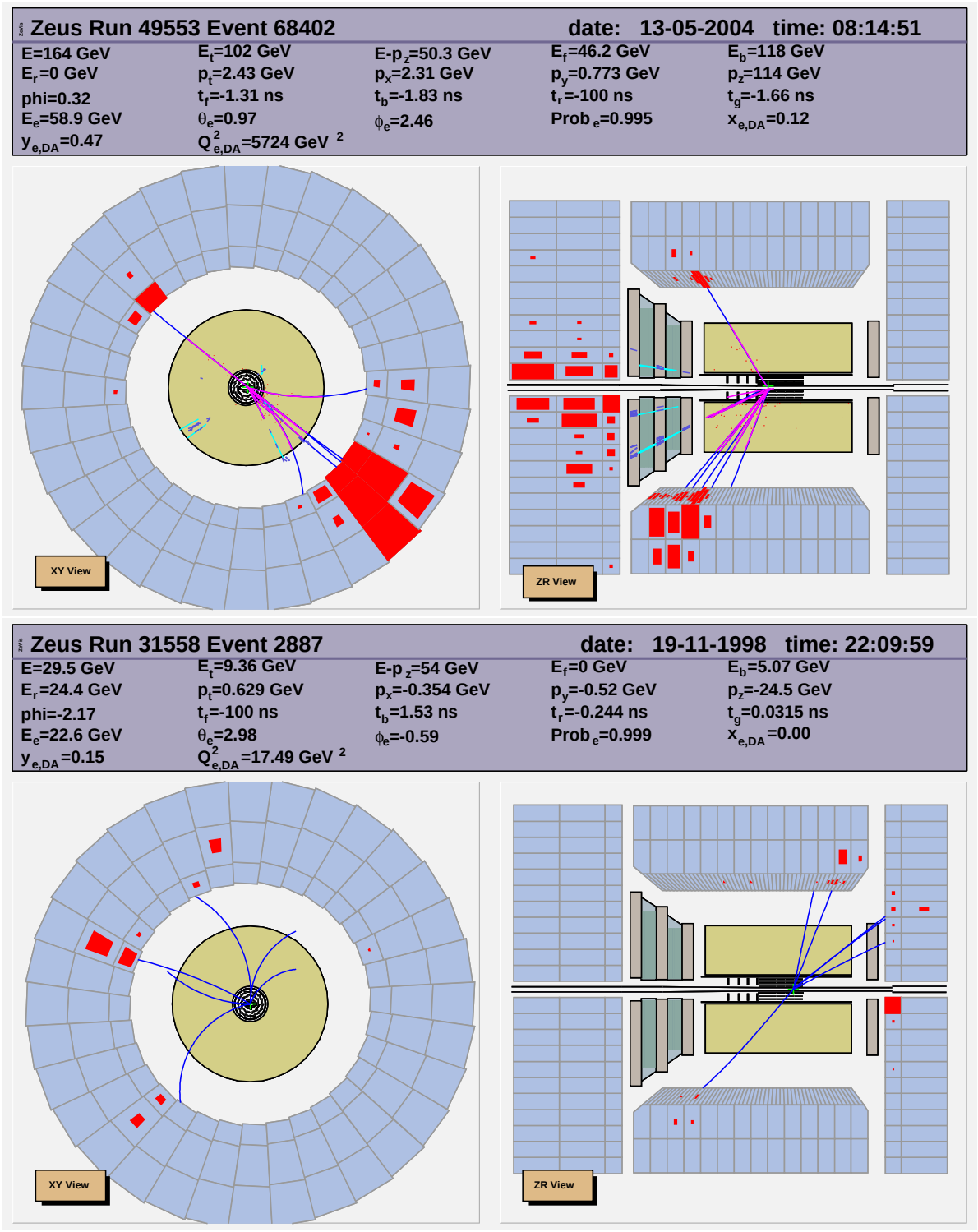

Figure 2.2: Event displays taken by ZEUS detector for a non-diffractive DIS event (upper plot) and a diffractive DIS event (lower plot).

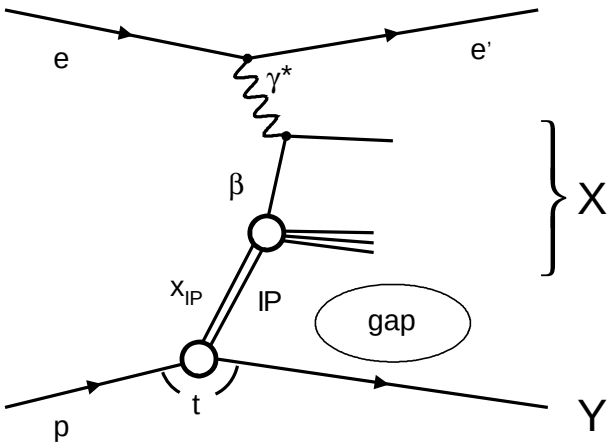

Figure 2.3: Diagram of inclusive diffractive deep-inelastic scattering.

The variable β is defined as:

$$\begin{aligned} \beta &\equiv \frac{Q^2}{2q\cdot(P-P')} = \frac{x}{x_{I\!P}} \\ &= \frac{Q^2}{M_X^2+Q^2-t} \\ &\approx \frac{Q^2}{Q^2+M_X^2}\,. \end{aligned} \tag{2.15}$$

It corresponds to the longitudinal momentum fraction of the pomeron carried by the struck quark in the resolved pomeron model.

2.6 Diffractive structure function

In analogy to the DIS cross section, the four-hold differential cross section of diffractive DIS, $ep \to eXp$, is described with a diffractive structure functions $F_2^{D(4)}(x, Q^2, x_{I\!P}, t)$ and $F_L^{D(4)}(x, Q^2, x_{I\!P}, t)$;

$$\begin{aligned} \frac{d^4\sigma_{ep\to eXp}}{dx_{I\!P}dtdQ^2dx} &= \frac{2\pi\alpha^2}{xQ^4}\Big([1+(1-y)^2]F_2^{D(4)} - y^2F_L^{D(4)}\Big) \\ &\approx \frac{2\pi\alpha^2}{xQ^4}\Big([1+(1-y)^2]F_2^{D(4)}\Big)\,. \end{aligned} \tag{2.16}$$

F_L is expected to be small in the kinematic range, hence it is usually neglected.

If the resolved pomeron model holds, we expect that $F_2^{D(4)}$ can be separated to a part which describes the emission of the pomeron and the other to describe the deep-inelastic scattering of the pomeron (Regge factorisation). The diffractive structure function is then

factorized to the pomeron flux factor $f_{I\!P/p}(x_{I\!P}, t)$ and the pomeron structure function $F_2^{I\!P}(\beta, Q^2)$ as follows;

$$F_2^{D(4)}(x, Q^2, x_{I\!P}, t) = f_{I\!P/p}(x_{I\!P}, t) F_2^{I\!P}(\beta, Q^2) \ . \tag{2.17}$$

The pomeron structure function $F_2^{I\!P}$ is a function of β and Q^2. The diffractive quark and anti-quark densities of the proton are related to the $F_2^{I\!P}$ as following;

$$F_2^{I\!P}(\beta, Q^2) = \sum_i e_i^2 \beta (q_i(\beta, Q^2) + \overline{q}_i(\beta, Q^2)) \ , \tag{2.18}$$

where the sum runs over all quark flavours.

As like DIS, diffractive processes are expected to obey the DGLAP evolution equation in perturbative QCD [7].

According to the Regge theory, the pomeron flux factor is written as;

$$f_{I\!P/p}(x_{I\!P}, t) = \frac{e^{B_{I\!P} t}}{x_{I\!P}^{2\alpha_{I\!P}(t)-1}} \ , \tag{2.19}$$

where $B_{I\!P}$ is a slope parameter and $B_{I\!P} = 4.6$ GeV^{-2} was obtained from [11]. The trajectory of the pomeron, $\alpha_{I\!P}(t)$, is assumed to be a linear function of t as following;

$$\alpha_{I\!P}(t) = \alpha_{I\!P}(0) + \alpha'_{I\!P} t \ . \tag{2.20}$$

where $\alpha_{I\!P}(0) = 1.085$ and $\alpha'_{I\!P} = 0.25$ were obtained from diffraction in $p\overline{p}$ collision [2].

2.6.1 Alternative model based on QCD

There are other models based on QCD. The colourless exchange (pomeron) is regarded as two-gluon at t-channel exchange. Wüsthoff Golec-Biernat (WGB) built a model connecting diffractive DIS and the normal DIS. The model is implemented in a Monte Carlo program called SATRAP which is described in Section 4.1.2.

2.7 Diffractive parton density functions

As like inclusive DIS, inclusive diffractive cross section in DIS can be written by a convolution of the universal partonic cross sections and the diffractive parton distributions. Using Eq.(2.17), the parton density of the pomeron was obtained from inclusive diffractive DIS cross section with the DGLAP evolution equation.

In recent years, various kinds of diffractive PDFs have been extracted from H1 and ZEUS data. The following three diffractive PDFs are compared in this thesis.

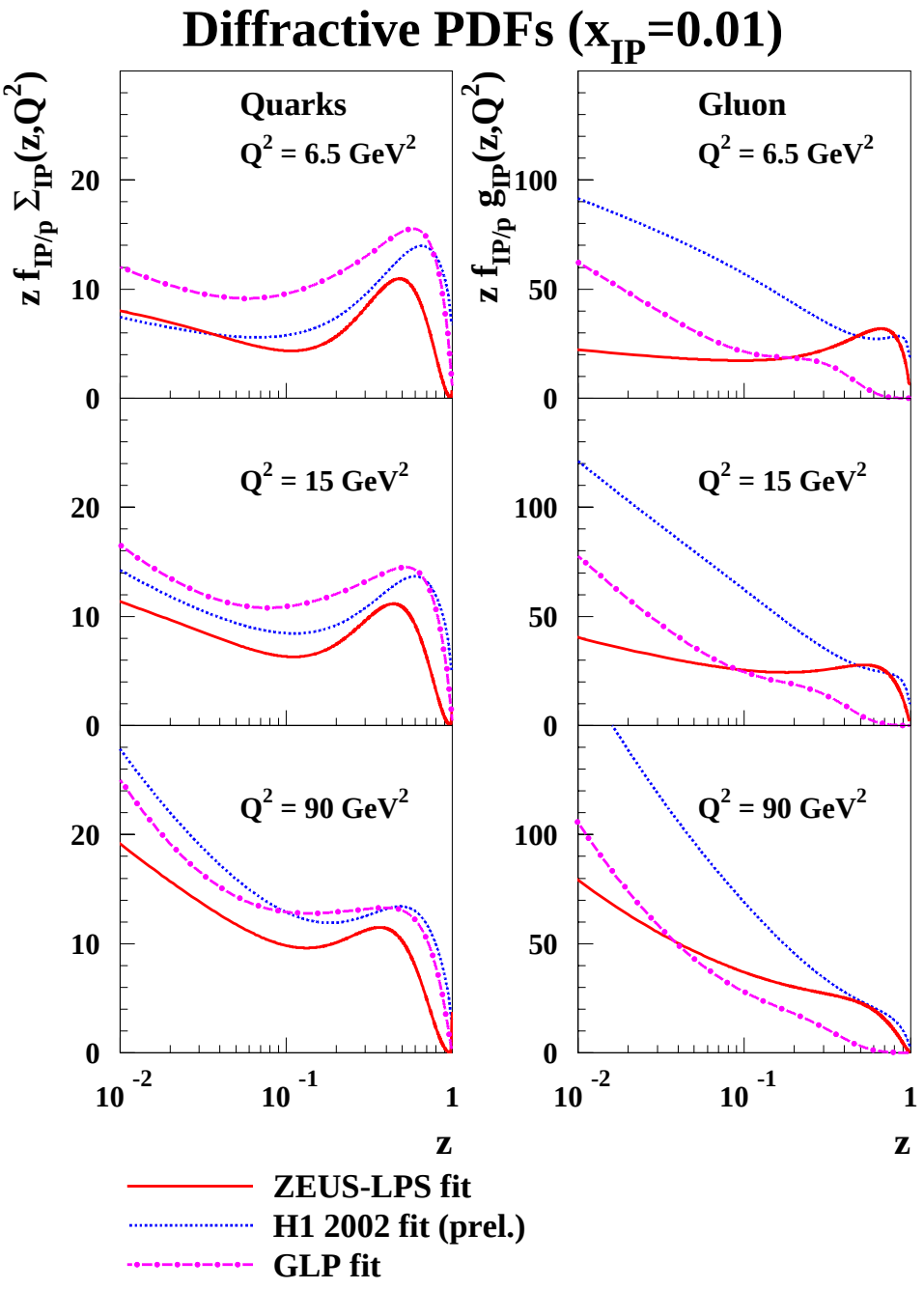

Figure 2.4: The predicted diffractive PDFs from the different NLO QCD fits. Both the quark and gluon distributions are shown for $x_{I\!P} < 0.01$ and for different values of Q^2. The solid lines represent the predictions from ZEUS-LPS fit, while the dotted lines represent H1 2002 fit. GLP fit is shown as the dash-dotted lines.

- **H1 2002 fit**
  The H1 2002 fit [12] is a result of the H1 collaboration on the NLO DGLAP QCD fit to the F_2^D data, obtained using the large rapidity gap method. $\alpha_s(M_Z) = 0.1085$ was used for α_s calculation, corresponding to $\Lambda^{\overline{\rm MS}}_{\rm QCD} = 200$ MeV for four flavours. This value of $\alpha_s(M_Z)$ is significantly smaller than the world average of $\alpha_s(M_Z) = 0.118$. The values of the pomeron flux factor as shown in Section 2.6 were used. $\alpha_{I\!P}(0)$ was set to 1.173.

- **ZEUS-LPS fit**
  The ZEUS-LPS fit [13] is a result of the NLO DGLAP QCD fit to the F_2^D data taken with the ZEUS leading proton spectrometer. In order to better constrain the diffractive PDFs, the charm contribution of the diffractive cross sections measured through D^* production were also included in the fit [14]. $\alpha_s(M_Z) = 0.118$ was used for α_s calculation, corresponding to $\Lambda^{\overline{\rm MS}}_{\rm QCD} = 338$ MeV for four flavours. The pomeron flux was taken to be the Donnachie-Landshoff form [15];

$$f_{I\!P}(x_{I\!P}, t) = \frac{9\beta_0^2}{4\pi^2 x_{I\!P}^{2\alpha_{I\!P}(t)-1}} F_1(t)^2 \ , \tag{2.21}$$

  where $\beta_0 = 1.8$ GeV^{-1}, $\alpha_{I\!P}(0) = 1.16$ and $\alpha'_{I\!P} = 0.25$ GeV^{-2} were used. $F_1(t)$ is the elastic form factor of the proton, given as;

$$F_1(t) = \frac{4m_p^2 - 2.79t}{4m_p^2 - t} \frac{1}{(1 - t/0.71)^2} \ . \tag{2.22}$$

- **GLP fit**
  The Groys-Levy-Proskuryakov (GLP) fit [16] is a result of the NLO DGLAP QCD fit to F_2^D data with the M_X method [17] measured by the ZEUS collaboration. $\alpha_s(M_Z) = 0.119$ was used for α_s calculation, corresponding to $\Lambda^{\overline{\rm MS}}_{\rm QCD} = 356$ MeV for four flavours. The pomeron flux factor was used as shown in Section 2.6. $\alpha_{I\!P}(0) = 1.13$ was used.

Figure 2.4 shows these diffractive PDFs as a function of z, the momentum fraction of the proton entering the hard sub process. The left side plots are the singlet quark distribution. The right side plots are the gluon distributions. The gluon density is clearly dominant in all PDFs. At the same time, the most significant differences between the different fits lie in the gluons. It is amazing that the gluon density between three diffractive PDFs are quite different. Although the comparison of these data themselves are still consistent, the difference are very large, especially at high z. The difference can be considered as an indication of the uncertainty in extracting the diffractive gluon density from the F_2^D data.

According to the previous analysis of F_2^D data the gluon component is likely dominant in the pomeron. However, there is still a large variation between these diffractive PDFs.

Therefore, it is important to investigate the amount of gluons using reactions which are more directly sensitive to gluons.

2.8 Dijets in diffraction

The dijet process in diffractive DIS is directly sensitive to the gluons in the pomeron. Thus, in this thesis, the dijet process in diffractive DIS has been studied.

The dijet production in diffraction, $ep \to e'p$ jet1 jet2 X', is factorized to the cross section of electron-parton and the parton density functions in the pomeron (the diffractive parton density functions) as following;

$$\sigma_{ep\to e'p \text{ jet1 jet2 } X'} = \sum_{i=\text{partons}} f_{i/I\!P} \otimes \hat{\sigma}_{ie} \ , \tag{2.23}$$

where i is summed up for the partons. Dijets processes in diffractive DIS include the boson gluon fusion (BGF) process and the QCD compton (QCDC) process at leading-order (LO) QCD as shown in Figure 2.5. Dijets mainly come from these processes. Therefore, the rate of diffractive dijet production depends on directly related to the gluon distribution in the pomeron.

An observable variable $z_{I\!P}^{\text{obs}}$ is introduced, denoted as following;

$$z_{I\!P}^{\text{obs}} = \beta\Big(1 + \frac{\hat{s}}{Q^2}\Big) \ , \tag{2.24}$$

where $\hat{s}$ is the invariant mass squared of the dijet. In the leading-order diagram as shown in Figure 2.6, $z_{I\!P}^{\text{obs}}$ is related to the four-momentum of the parton originating from the colourless exchange (v) in the following way,

$$z_{I\!P}^{\text{obs}} \ = \ \frac{q \cdot v}{q \cdot (P - P')} \ . \tag{2.25}$$

Thus, $z_{I\!P}^{\text{obs}}$ corresponds to the longitudinal momentum fraction of the pomeron used in the jet production.

The purpose of this thesis is to measure the dijet cross section in diffractive DIS as functions of various kinematic variables and to compare with the prediction from the next-to-leading order (NLO) QCD with the diffractive PDFs obtained by the inclusive diffraction F_2^D data. The cross section as a function of $z_{I\!P}^{\text{obs}}$ is especially important since it directly reflects to the longitudinal distribution of the partons in the pomeron.

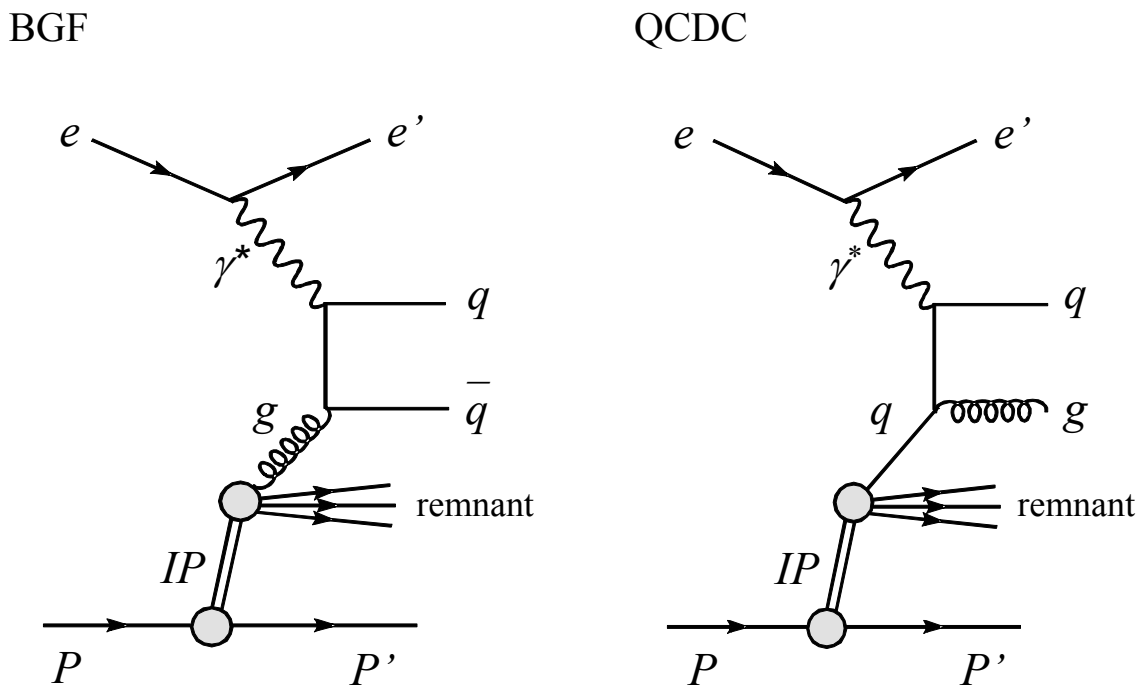

Figure 2.5: Diagrams of boson gluon fusion (BGF) process and QCD compton (QCDC) process in diffractive DIS.

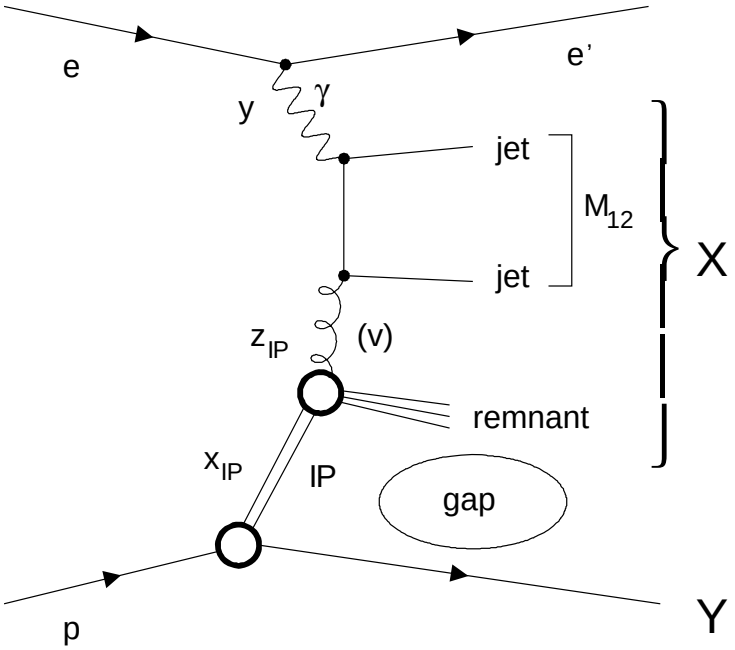

Figure 2.6: A diagram of diffractive boson gluon fusion (BGF) process.

2.8.1 Direct and Resolved photon process

In addition to the process like Figure 2.6, one could consider processes where the virtual photon fluctuates into a hadronic system and one of the parton interacts with the partons in the proton as shown in Figure 2.7. Such processes are called the resolved photon processes. The process like Figure 2.6 is called a direct photon process.

The following observable variable $x_\gamma^{\rm obs}$ can be defined from the final dijet system;

$$x_\gamma^{\rm obs} = \frac{\sum\limits_{i=1,2} E_{T,{\rm jet}\ i}\ e^{-\eta_{{\rm jet}\ i}}}{\sum\limits_{i={\rm hadrons}} E_{T,i}\ e^{-\eta_i}}\ , \tag{2.26}$$

where the sum i of the denominator indicates dijets, $E_{T,{\rm jet}i}$ is the transverse energy of jet i, and $\eta_{{\rm jet}i}$ is the pseudo-rapidity of jet i. The sum i of the numerator indicates the hadronic final state particles, $E_{T,i}$ is the transverse energy of the hadronic final states particle i, and η_i is the pseudo-rapidity of the hadronic final states particle i.

For the resolved process, a variable $x_\gamma^{\rm obs}$ is related to for the leading-order (LO) level;

$$x_\gamma^{\rm obs} = \frac{P \cdot u}{P \cdot q}, \tag{2.27}$$

where u is the four-momentum of the parton originating from the virtual photon, and q is the four-momentum of the virtual photon. x_γ corresponds to the longitudinal momentum fraction of the parton involved in the hard interaction to the photon. If an event is from the direct photon process, $x_\gamma^{\rm obs} = 1$. On the other hand, if the resolved photon process, $x_\gamma^{\rm obs} < 1$.

The resolved photon process exists in dijet process in inclusive DIS at high Q^2 [18]. Therefore, dijet process in diffractive DIS should be considered.

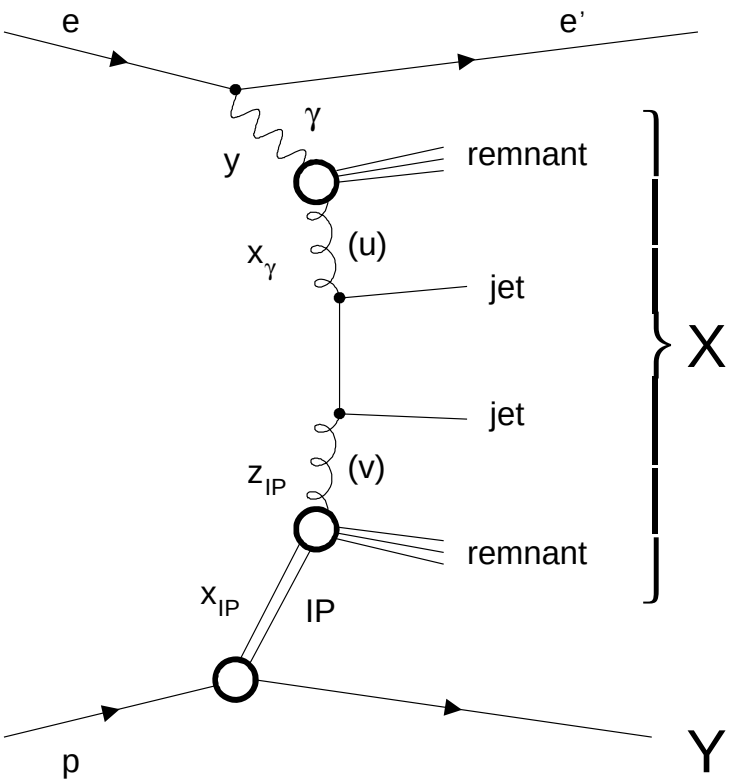

Figure 2.7: A diagram of diffractive resolved photon process.

Chapter 3

Experimental setup

This analysis is based on the data taken with the ZEUS detector at the HERA electron(e)-proton(p) collider. This chapter describes the HERA and the ZEUS detector in this analysis.

3.1 HERA accelerator

HERA (Hadron-Elektron Ring Anlage) in Germany is the unique electron(e)-proton(p) collision accelerator in the world. It was constructed at the DESY (Deutsches Elektronen-Synchrotron) laboratory in Hamburg, Germany. HERA has four experimental sites. There are the H1 and ZEUS detectors for collision experiments, the HERMES and HERA-B for fixed target experiments.

The overview of HERA is shown as Figure 3.1. HERA is an about 2 km diameter ring, 6336 m in circumference and located about 10 m - 25 m deep underground. PETRA, a pre-HERA accelerator, accelerates protons up to 40 GeV and electron (or positrons) to 12 GeV. These beams are injected to the two storage rings of the HERA accelerator. At HERA, protons are further accelerated to 920 GeV and electrons (or positrons) to 27.5 GeV. The collision of the two particles gives a centre-of-mass energy of $\sqrt{s} = 318$ GeV. There are 220 bunches of protons and electrons in the HERA ring crossing in the time interval of 96 ns.

The magnets of the electron storage ring are made of normal conductors. The magnets of the proton storage ring are super-conducting magnets, producing a magnetic field of 4.7 Tesla for the high momentum proton beam.

The integrated luminosity taken by the ZEUS detector in 1994-2000 year is shown as Figure 3.2 as a function of the days of the run. The basic operational parameters of HERA are given in Table 3.1. The maximum instantaneous luminosity achieved in the above running period was $\mathcal{L} = 1.69 \times 10^{31}$ cm^{-2}s^{-1}.

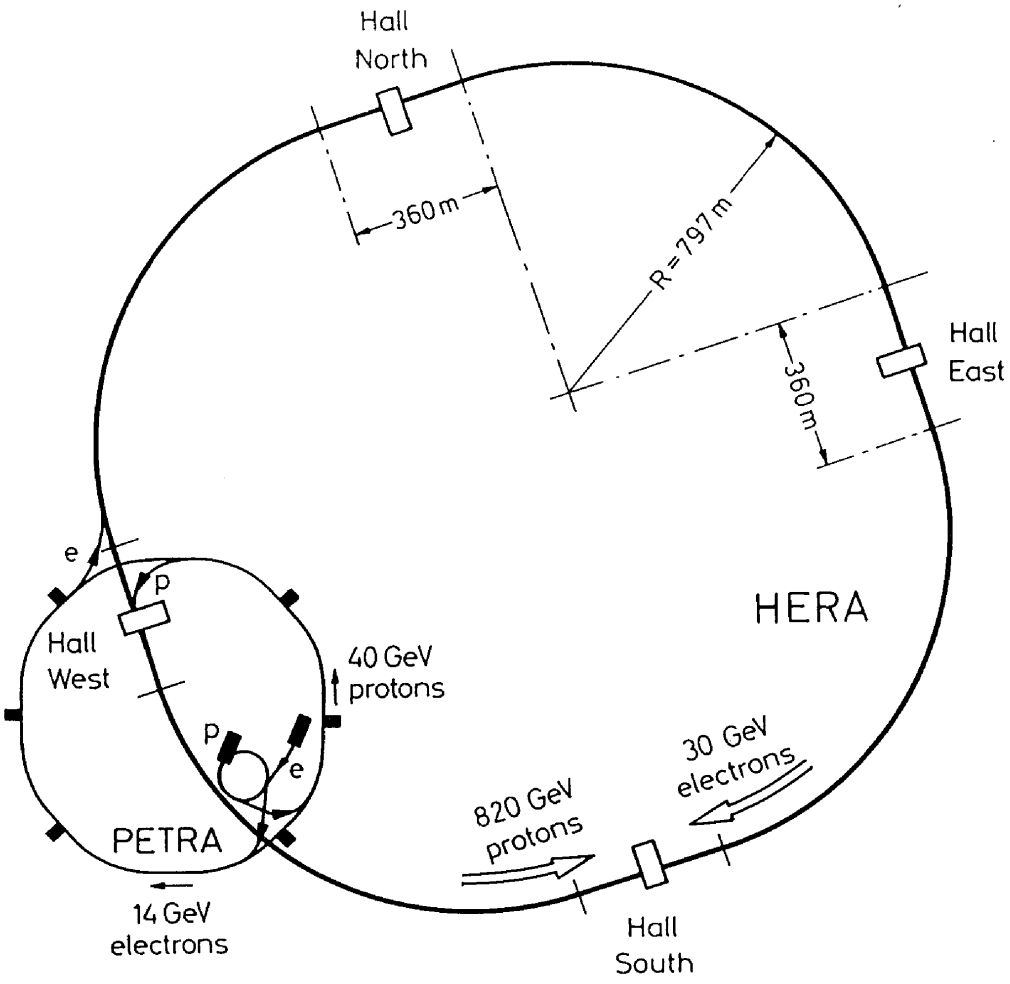

Figure 3.1: HERA accelerator

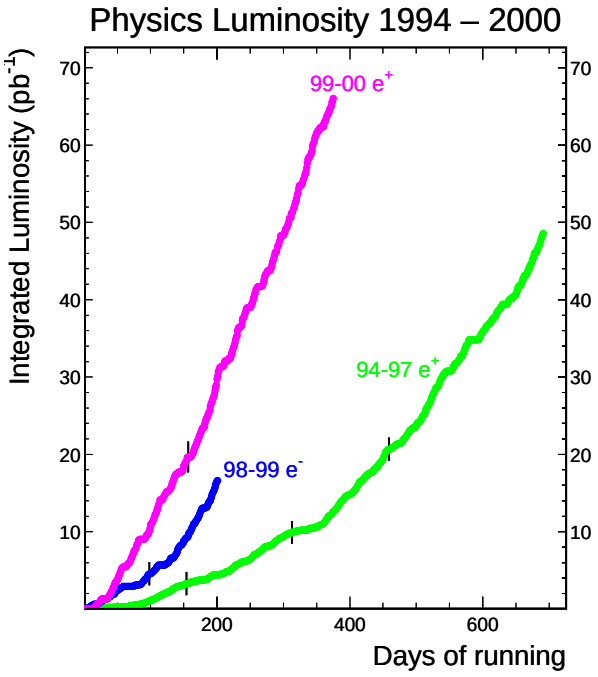

Figure 3.2: The integrated luminosity taken by ZEUS detector as a function of the day of the run.

Parameter	**HERA-e**	**HERA-p**
E(GeV)	27.5	920
I(mA)	50	100
$N_{ppb}(10^{10})$	3.5	7.3
n_{tot}/n_{col}	189/174	180/174
β_x/β_y(m)	0.90/0.60	7.0/0.5
ϵ_x(nm)	41	$5000/\beta\gamma$
ϵ_y/ϵ_x	10%	1
$\sigma_x/\sigma_y(\mu$m)	192/50	189/50
σ_z(mm)	11.2	191
$2\Delta\nu_x$	0.024	0.0026
$2\Delta\nu_y$	0.061	0.0007
$\mathcal{L}(\text{cm}^{-2}\text{s}^{-1})$	16.9×10^{30}	
$\mathcal{L}_s(\text{cm}^{-2}\text{s}^{-1}\text{mA}^{-2})$	0.66×10^{30}	

Table 3.1: HERA main parameters

3.2 The ZEUS detector

3.2.1 Overview

This analysis uses a data sample taken by the ZEUS detector [19], which is located in the south hall of HERA (see Figure 3.1). Figure 3.3 shows the schematic layout of the ZEUS detector. In this section, the components of the ZEUS detector are described.

The ZEUS coordinate system is a right-handed Cartesian system, with the Z axis is pointing toward the proton beam direction, referred to as the forward direction, and the X axis is horizontal pointing towards the center of HERA. The coordinate origin is at the nominal interaction point. The pseudorapidity is defined as;

$$\eta = -\ln\left(\tan\frac{\theta}{2}\right),$$

where the polar angle, θ, is measured with respect to the proton beam direction.

Jet reconstruction was performed using the information from the central tracking detector (CTD) and the uranium-scintillator calorimeter (CAL). Diffractive events were selected by requiring a large rapidity gap in the forward region of the CAL and in the forward plug calorimeter (FPC) which was placed in an open space of the forward hole of the CAL, which accommodates the beam pipe. The electron reconstruction was performed by the information of the CAL and the small angle rear tracking detector (SRTD) which is located around the rear beam pipe on the face of the rear calorimeter. The C5 counter (C5) and the veto wall (VETO) reject the backgrounds of the beam-gas interaction. These detectors are located at the up stream of the proton beam. The luminosity monitors are located at the down stream of the electron beam in order to measure the luminosity.

In this section, main detectors which were mainly used by this analysis, CTD, CAL, FPC, SRTD, Luminosity monitors, and data acquisition system are explained in detail.

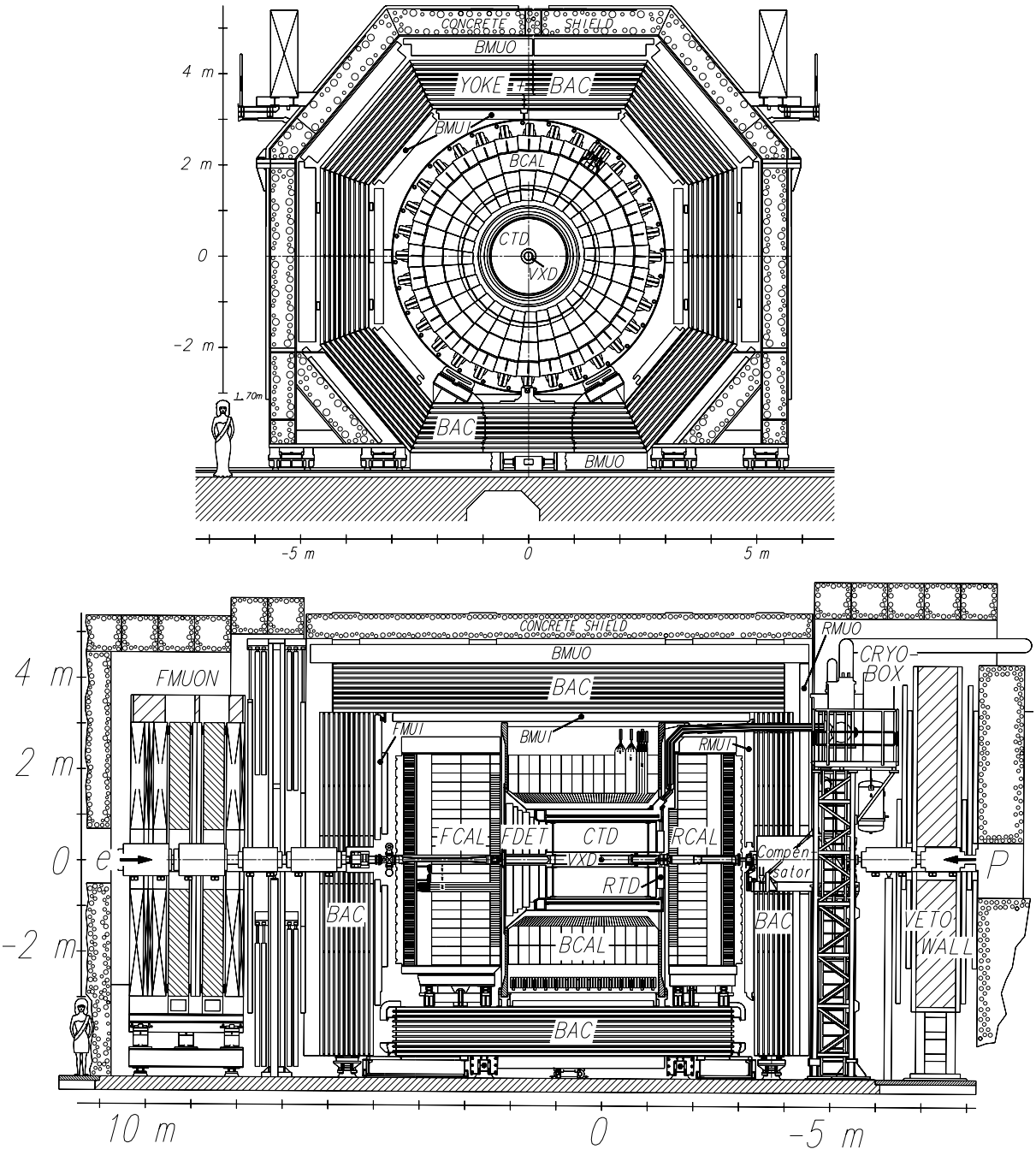

Figure 3.3: ZEUS detector

3.2.2 Central Tracking Detector

The central tracking detector (CTD) [20] is a system to track charged particles. It covers the polar angle range of $15° < \theta < 164°$. It is located in a superconducting solenoid inside the CAL. Figure 3.4 shows the wire layout of a 45° sector (octant). The CTD consists of the nine superlayers. The layers are numbered from the inner side as shown in the figure. The wires of the superlayer with the odd numbers are strung in parallel to the Z-axis. The wires of the superlayer with the even numbers have a tilt to about 5° (stereo angle) for measuring the Z position of tracks with a better precision, where the Z position was measured by timing. Ar(90%), CO_2(8%) and C_2H_6(2%) are used for the gas inside the chamber. The resolution of p_T in the CTD is as following;

$$\frac{\sigma(p_T)}{p_T} = 0.0058 p_T \oplus 0.0065 \oplus \frac{0.0014}{p_T}, \tag{3.1}$$

where p_T is in a unit of GeV [21].

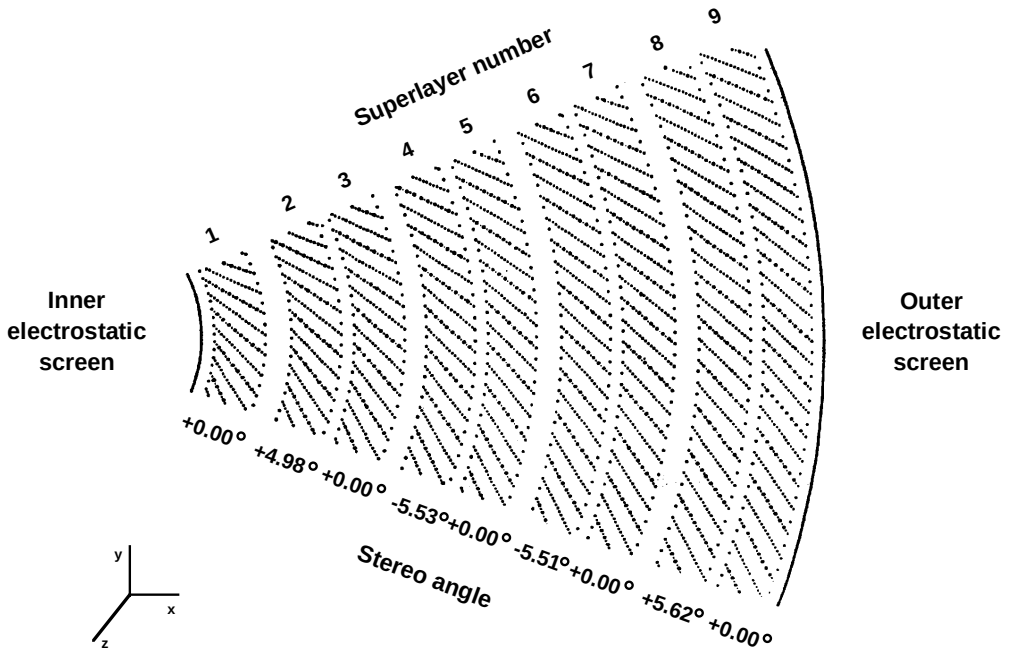

Figure 3.4: Layout of wires in the CTD

3.2.3 Uranium Calorimeter

The ZEUS calorimeter (CAL) is a uranium-scintillator sandwich calorimeter [22]. The CAL surrounds the solenoid and tracking detectors almost hermetically, as shown in Figure 3.5. The solid angle coverage is 99.8 % in the forward hemisphere and 99.5 % in the backward hemisphere. The CAL mechanically consists of three components:

- the forward calorimeter (FCAL) covering polar angles of $2.2° < \theta < 39.9°$,
- the barrel calorimeter (BCAL) extending to $36.7° < \theta < 129.2°$, and
- the rear calorimeter (RCAL) extending to $128.1° < \theta < 176.5°$.

The structure of the three calorimeter components is similar. They are subdivided longitudinally into two parts. The inner part is the electromagnetic calorimeter (EMC) with a depth of about $26X_0$ (or 1λ), where X_0 is the radiation length and λ is the absorption length. The outer part is called the hadronic calorimeter (HAC). It varies in depth from 6λ in the very forward region to about 3λ in the rear region. In FCAL and BCAL, the HAC is further divided into two sections (HAC1 and HAC2).

The thickness of the DU plate is 3.3 mm, corresponding to about $1X_0$, The thickness of the plastic scintillator is 2.6 mm. These are chosen to have an equal response to hadron and electron particles.

FCAL, BCAL and RCAL consist of modules. Each module consists of towers which have a transverse size of 20×20 cm^2. The tower is divided by EMC and HAC section according to the distance from the interaction point. Further, for FCAL and BCAL, EMC section is divided by four cells. For RCAL, EMC section is divided by two cells. Three dimensional view of a FCAL module in shown in Figure 3.6.

The energy resolution (σ_E) of the CAL is measured in the test beam;

$$\frac{\sigma_E}{E} = \frac{18\%}{\sqrt{E}} \oplus 1\% \quad \text{(for electrons)} , \tag{3.2}$$

$$\frac{\sigma_E}{E} = \frac{35\%}{\sqrt{E}} \oplus 2\% \quad \text{(for hadrons)} , \tag{3.3}$$

where E is the energy with a unit of GeV, and $\oplus$ indicates a quadratic sum. The response for electrons and hadrons is:

$$e/h = 1.00 \pm 0.03 . \tag{3.4}$$

	FCAL			BCAL			RCAL	
Calorimeter sections	EMC	HAC1	HAC2	EMC	HAC1	HAC2	EMC	HAC1
Number of layer	25	80	80	21	49	49	25	80
Radiation length	25.9	84.2	84.2	22.7	52.4	52.5	25.9	84.2
Absorption length	0.96	3.09	3.09	1.05	2.03	2.04	0.95	3.09

Table 3.2: Summary of Calorimeter parameters. The number of layer, the radiation length and the absorption length are shown separately for each calorimeter sections.

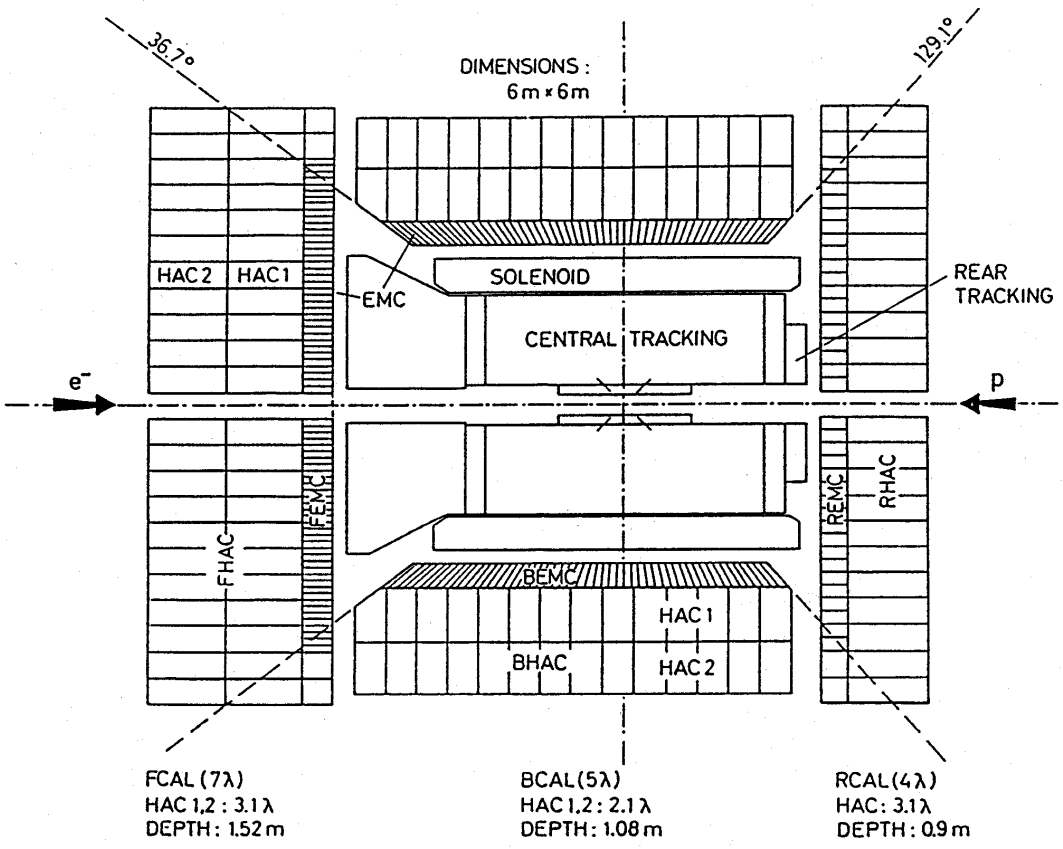

Figure 3.5: Overview of uranium calorimeter

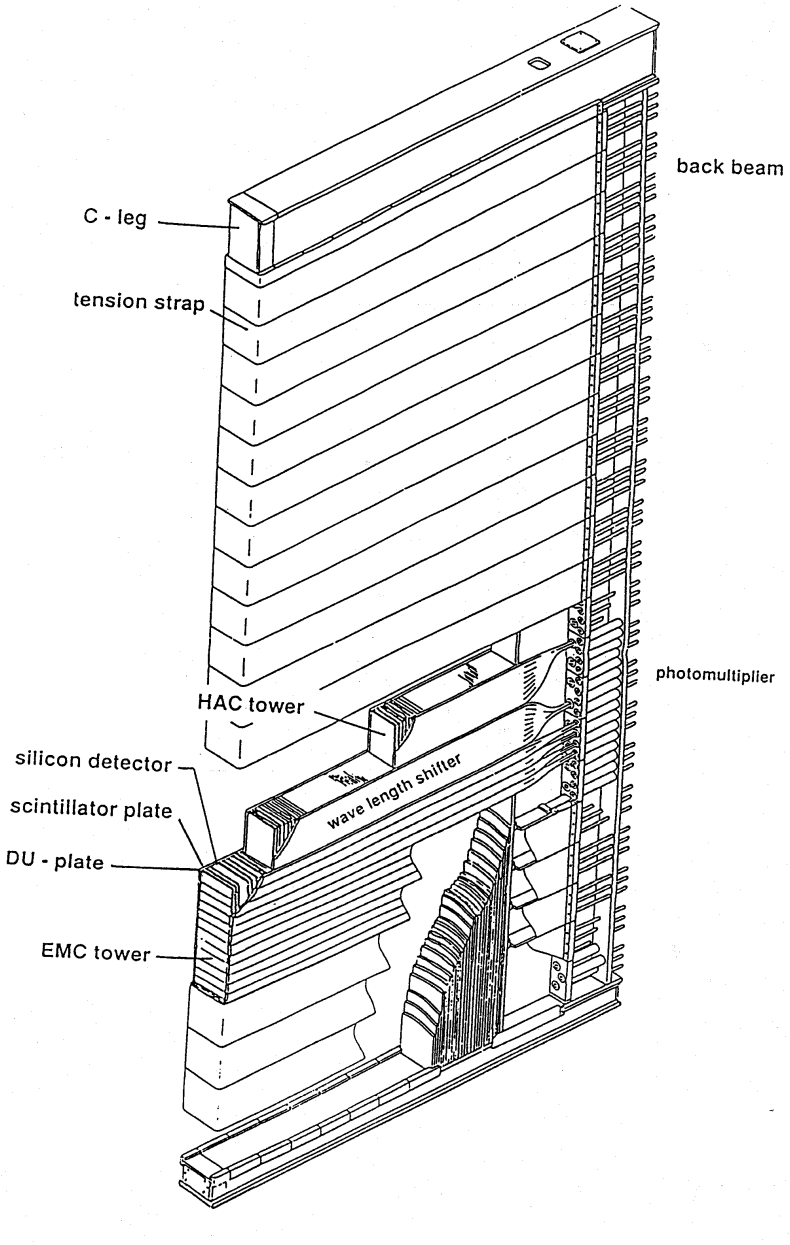

Figure 3.6: Overview of FCAL module

3.2.4 Forward Plug Calorimeter

The forward plug calorimeter (FPC) [23, 24] is the lead-scintillator sandwich calorimeter read out by wave length shifting (WLS) fibers and photomultipliers (PMT). It is installed in 1998, in the $20 \times 20\text{cm}^2$ beam hole of the FCAL to extend forward calorimetric coverage in pseudorapidity from $\eta = 3.8$ to $\eta = 5.0$. A front view of the FPC is shown in Figure 3.7. The FPC has a 63 mm diameter hole and dimensions of $192 \times 192 \times 1080$ mm^3. Lead plates of 15 mm thickness alternate with scintillator layers of 2.6 mm. The WLS fibers are inserted in the lead and scintillator layers. The holes are located in a 12 mm step square grid. The FPC has 232 fiber holes. In addition, there are four brass tubes (1.4 mm inner diameter) for guiding a ^{60}Co source, placed on the tip of a long steel wire, for the monitoring of the calibration. The FPC is also expected to provide equal response to hadrons and electrons, i.e. $e/h = 1$.

With the layer structure chosen, the FPC has approximately the same X_0 and λ per unit depth as the FCAL; X_0(FPC) = 0.68 cm and X_0(FCAL) = 0.74 cm ; λ(FPC) = 20 cm and λ(FCAL) = 21.0 cm. This minimizes the fluctuations in the energy measurement.

The FPC is subdivided longitudinally into an electromagnetic (EMC) and a hadronic (HAC) section which are read out separately as shown in Figure 3.7. The electromagnetic section consists of 10 layers of lead and scintillator corresponding to $26.5X_0$ and 0.9λ. The hadronic section of the FPC consists of 50 layers and represents 4.5λ leading to a total for the FPC of 5.4λ as shown in Table 3.3.

The scintillator layers consist of tiles and form cells which are read out individually as shown in Figure 3.7. The cell cross sections are $24 \times 24\text{mm}^2$ in the EMC and $48 \times 48\text{mm}^2$ in the HAC section. The 8(4) inner most cells in EMC (HAC) surrounding the beam hole follow circular shape given by the beam hole.

The energy resolution (σ_E) of the FPC is:

$$\frac{\sigma_E}{E} = \frac{0.41 \pm 0.02}{\sqrt{E}} \oplus 0.062 \pm 0.002 \quad \text{(for electrons)} , \tag{3.5}$$

$$\frac{\sigma_E}{E} = \frac{0.65 \pm 0.02}{\sqrt{E}} \oplus 0.06 \pm 0.01 \quad \text{(for pions)} , \tag{3.6}$$

where E has a unit of GeV.

	FPC		
Calorimeter sections	EMC	HAC	Total
Number of layer	10	50	60
Radiation length	26.5	133.0	159.5
Absorption length	0.9	4.5	5.4

Table 3.3: Summary of FPC parameters. The number of layer, the radiation length and the absorption length are shown separately for each calorimeter sections.

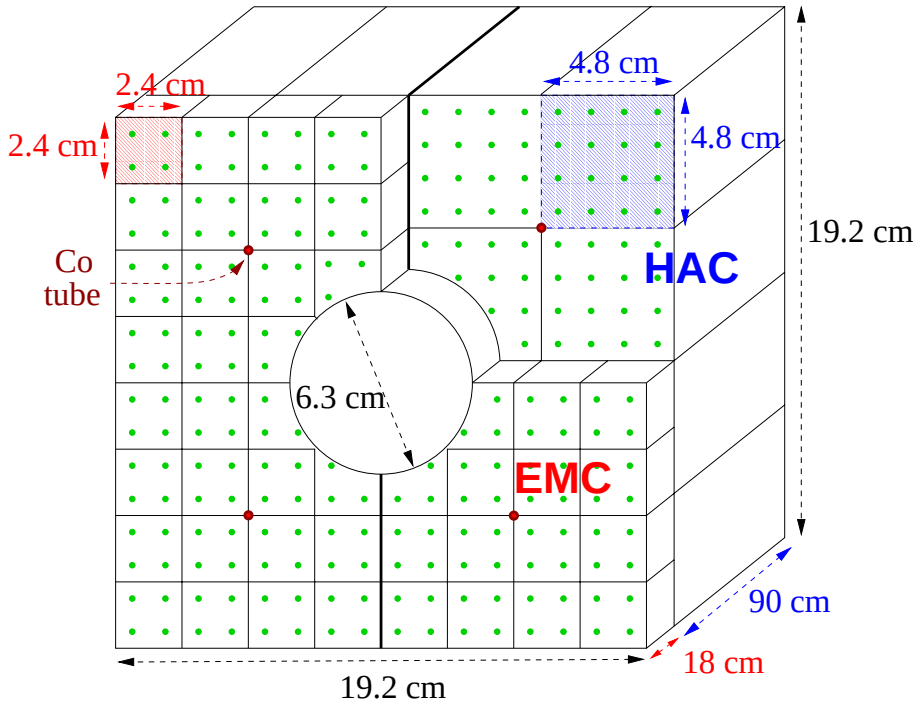

Figure 3.7: Front view of the FPC. The readout cells and the position of WLS fibers are shown. Notice that there is one hadronic readout cell behind 2×2 electromagnetic cells, except for the cells near the beam hole.

3.2.5 Small angle Rear Tracking Detector

The small angle rear tracking detector (SRTD) [25, 26] is located around the beam pipe on the face of the RCAL. The SRTD consists of four quadrants of scintillator strips with a width of 1 cm. The arrangement of four quadrants are shown in Figure 3.8. The four quadrants are located with the hole for the beam pipe of 20×8 cm^2. The SRTD improves the position of the electron and charged particles, and corrects the electron energy at small angle.

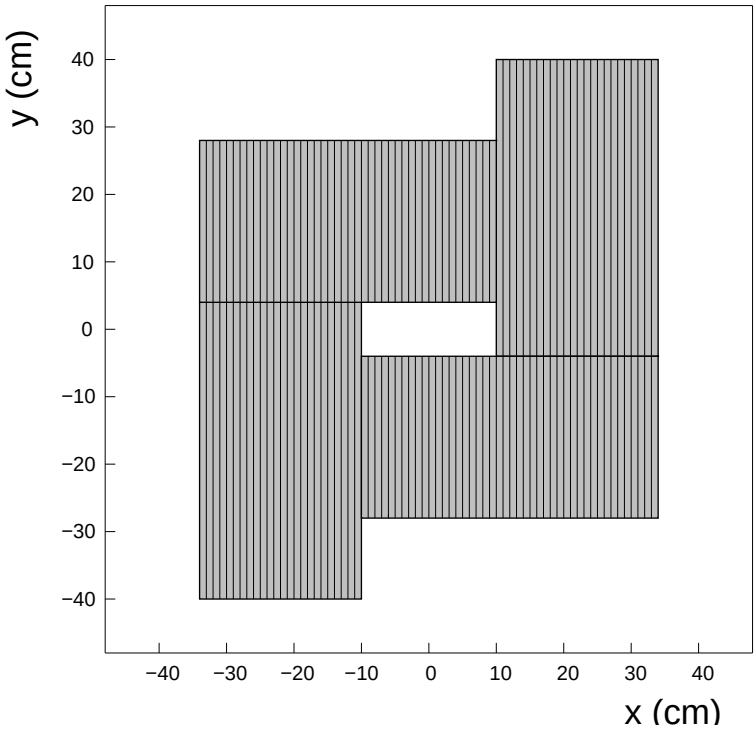

Figure 3.8: Schematic picture of the layers of SRTD.

3.2.6 Luminosity monitors

The luminosity is measured from the event rate of the bremsstrahlung process, $ep \rightarrow ep\gamma$. The large cross section of this process allows for the continuous measurements during the experiments. Since the photons and the electrons from the bremsstrahlung are emitted at small angle, the photons and the electrons travel initially inside the beam pipe. Therefore, the photon calorimeter and the electron calorimeter are located far from the ZEUS main calorimeter. Figure 3.9 shows the top view for the luminosity monitors on the beam line of HERA. The photon calorimeter is located at $Z = -107$ m, and the electron calorimeters are located at $Z = -8, -35, -44$ m. Since the photons travel straightly, the photon calorimeter is located on the beam line. On the other hand, since the electron from the bremsstrahlung is curved by the magnets, the electron calorimeter is located outside on the beam line. The photon calorimeter is mainly used, and the electron calorimeter is used for the systematic check [27].

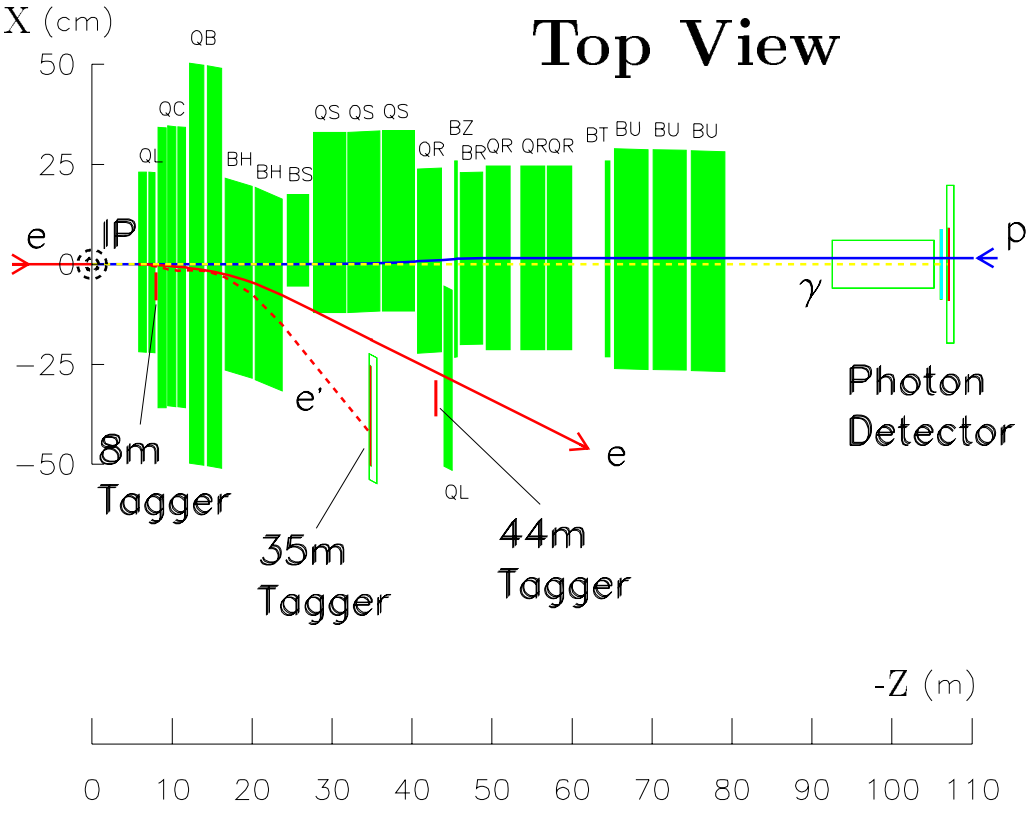

Figure 3.9: Top of view for luminosity monitors

3.2.7 Data Acquisition System

Since the physics event rate is much lower than the rate of background which mainly come from the interactions between proton beam and residual gas in the beam pipe, the ZEUS trigger system [28] adopted a three-level trigger in order to reduce the event rate by effectively removing the background. The data flow of the ZEUS trigger and data acquisition system is shown as Figure 3.10.

First Level Trigger

The first level trigger (FLT) uses special hardware for trigger decision. The FLT is able to reduce from 10 MHz of the bunch crossing rate to 200 Hz trigger rate. Since the interval time between the bunch crossings is only 96 nsec and the FLT need to make a decision to all bunch crossings, the FLT has a pipeline structure. The FLT is divided into component FLTs providing trigger signals from each component, and the global FLT (GFLT) which makes finally a decision whether the event is taken or not. GFLT has a output of 64 bits. Each bit makes a decision of a trigger logic, which is called "slot".

Second Level Trigger

The second level trigger (SLT) gives the trigger decision by software. The SLT also has a pipeline structure. Each detector components calculate independently the SLT information. These data are sent to the global SLT (GSLT) which makes final decisions. The trigger rate is reduced from about 200 Hz to about 50 Hz. At this stage, a large fraction of the beam gas events are removed.

Third Level Trigger

The third level trigger (TLT) consists of the software trigger located after the event builder, which collects all the detector information of an event and build a event database entry. Each CPU deals with each events with complete data from all detector components. An event reconstruction program which is close to the offline reconstruction runs for event selection. For example, tracking of charged particle, finding electron and jet in the CAL are done for tight selection of physics events. On the TLT, the trigger rate is reduced from 50 Hz to about 10 Hz. These results are saved to a mass storage.

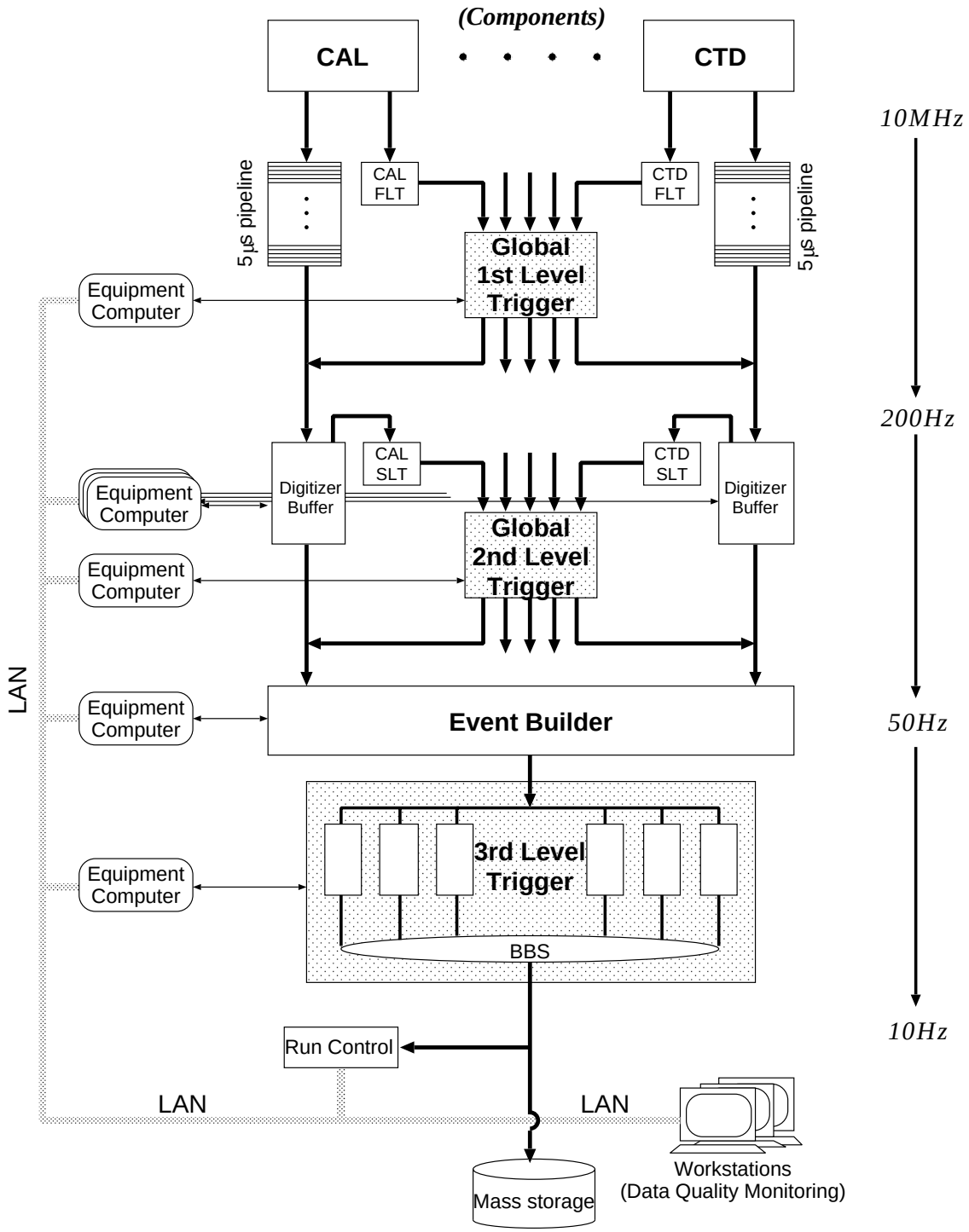

Figure 3.10: Flow of Data Acquisition System

Chapter 4

Monte Carlo simulation

Monte Carlo (MC) simulation programs are used to correct the data to the hadron level by estimating the acceptance and efficiency of the detector. They are also used to estimate the quantity of the background process. In this analysis, RAPGAP and SATRAP programs are used to simulate diffractive processes. For the background processes, DJANGO program is used for non-diffractive DIS, and EPSOFT program is used to study the proton dissociation. In this chapter, these MC programs are briefly explained.

4.1 Simulation of diffractive deep-inelastic scattering

4.1.1 RAPGAP

The RAPGAP MC event generator [29] is based on the resolved pomeron model as explained in Section 2.4. The photon-parton scattering is calculated from the QCD matrix element at the leading-order, i.e. BGF processes and QCD compton processes are included. The higher order QCD radiation at both initial and final states is simulated by the parton shower (PS) model [30]. RAPGAP are interfaced to the HERACLES [31] event generator for the simulation of QED radiative processes and to JETSET [32] for the simulation of the hadronization based on the Lund string model [33]. The version of RAPGAP used in this analysis is 2.08/18.

In this analysis, RAPGAP is used to generate the diffractive DIS event samples. The samples are generated using the pomeron structure functions "H1 fit 2" diffractive parton density functions (PDFs) obtained by fitting to the F_2^D data taken in 1994 for H1 collaboration [34]. The resolved photon processes in DIS are also generated separately. GRV-G-HO [35] is used as the virtual photon PDFs. The sample of the resolved photon processes is added to the direct photon event sample with a ratio predicted by the RAPGAP.

4.1.2 SATRAP

SATRAP event generator [36, 37] is based on the WGB model to describe the diffractive process. In this model, diffractive processes are regarded as the interaction between the proton and the partonic system fluctuated from the photon as shown in Figure 4.1. The exchange of two gluon is considered to satisfy the colour neutral exchange. In addition to $q\bar{q}$ state, $q\bar{q}g$ state has to be taken into account for the photon system. The $q\bar{q}$ state is dominant in the region $Q^2 \approx M_X^2$. On the other hand, the $q\bar{q}g$ state is important in $Q^2 \ll M_X^2$. In the measured range of this analysis, the $q\bar{q}g$ state is dominant.

In contrast to the resolved pomeron model, pomeron PDF is not an input to SATRAP. The model is tuned with F_2^D data by changing the ratio between the $q\bar{q}$ and $q\bar{q}g$ states. SATRAP effectively shows the gluon dominance in the pomeron.

SATRAP has the interface of the RAPGAP 2.08/18 framework. The parton shower in SATRAP is based on the colour dipole model (CDM) [38]. The CDM is implemented by ARIADNE program [39]. This MC does not include the resolved photon contribution to the γ^*-p cross section. The QED radiative effects are implemented in HERACLES [31] and the hadronization is implemented in the Lund string model in JETSET [40].

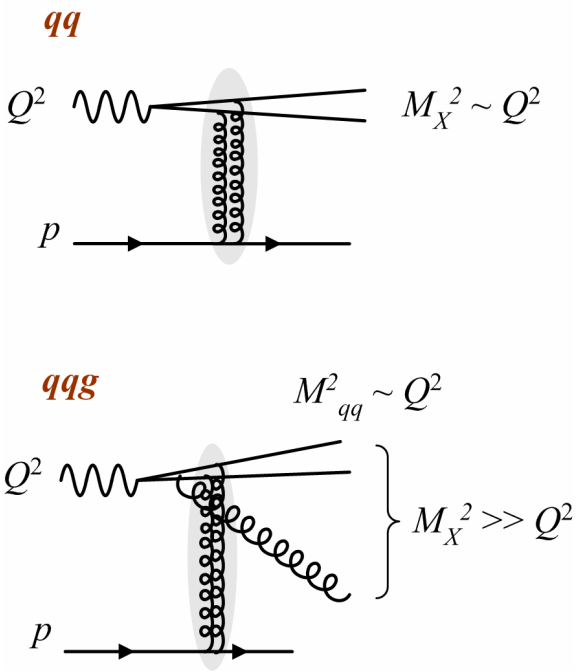

Figure 4.1: Diagram of $q\bar{q}$ and $q\bar{q}g$ states.

4.2 Simulation of the other processes

4.2.1 DJANGO

DJANGO [41] is the program to simulate the non-diffractive DIS processes. DJANGO is a combined package of the HERACLES 4.5 and the LEPTO 6.5. The QED radiation is simulated using HERACLES, and the QCD radiation is simulated by the CDM using ARIADNE implemented inside LEPTO. The hadronization is simulated by JETSET. CTEQ4D in PDFLIB package is used for the proton density function.

4.2.2 EPSOFT

EPSOFT [42] is the MC program for simulating soft diffractive photon-proton collisions based on the vector meson dominance model in which the photon has the hadronic structure and fluctuates into a virtual vector meson state. After the collision, both photon and proton system dissociates to high mass states, based on the Regge model. This program has been developed in the framework of HERWIG 5.8 [43] program package, in which most of the QCD and QED processes in $p\overline{p}$, e^+e^-, and ep collisions can be simulated. In this analysis, EPSOFT is used for estimating the proton dissociation background as mentioned in Section 5.8.2.

4.3 Simulation of the ZEUS detector

The event generated by these MC programs pass through the MOZART program, which simulates the ZEUS detector implemented using the GEANT 3.21 program [44]. After this simulation, the trigger simulation is performed by ZGANA, the simulation program package of ZEUS trigger. Finally, these simulated events have the same format as the data through the same event reconstruction program.

Chapter 5

Reconstruction and Event selection

This chapter describes the reconstruction of kinematic variables and the event selection for dijet processes in diffractive DIS.

5.1 Event sample

The event sample used in this analysis corresponds to an integrated luminosity of 65.2 pb^{-1} taken by the ZEUS detector in the period of 1999-2000 year. In this period, HERA was running with the proton beam energy 920 GeV and the electron beam energy 27.5 GeV. The sample is a mixture of 3.2 pb^{-1} of e^-p running and 62.0 pb^{-1} of e^+p running.

5.2 Online event selection

Online event selections are performed by three level triggers as described in Section 3.2.7. Different logic were imposed depending on the e^+p or e^-p running. The trigger logic during the e^-p running was required only the DIS condition, i.e. presence of a scattered electron. For the e^+p running, a diffractive requirement was imposed in addition, such that the energy deposit of the FPC detector is less than 20 GeV. The detailed trigger logics used in this analysis are described in Appendix A.

5.3 Offline event selection

The offline event selection of this analysis can be classified into the following three steps;

- DIS event selection,
- Diffractive event selection,

- Dijet event selection.

The reconstruction and the event selection are described in the following sections.

5.4 Event reconstruction

5.4.1 Reconstruction of the event vertex

An event vertex is found from the reconstructed tracks found by the CTD. The Z component of the vertex is to lie around the nominal interaction point at $Z = 0$. Figure 5.1 shows the distribution for the Z position of the vertex after the DIS selection (see Section 5.5) before requiring a cut on the vertex point. The Monte Carlo sample is normalized to data in Figure 5.1. The vertex requirement is the following as;

$$-50 \text{ cm} < Z_{\text{vertex}} < 50 \text{ cm} \ .$$

This cut rejects the background events originated from beam gas interactions or cosmic showers.

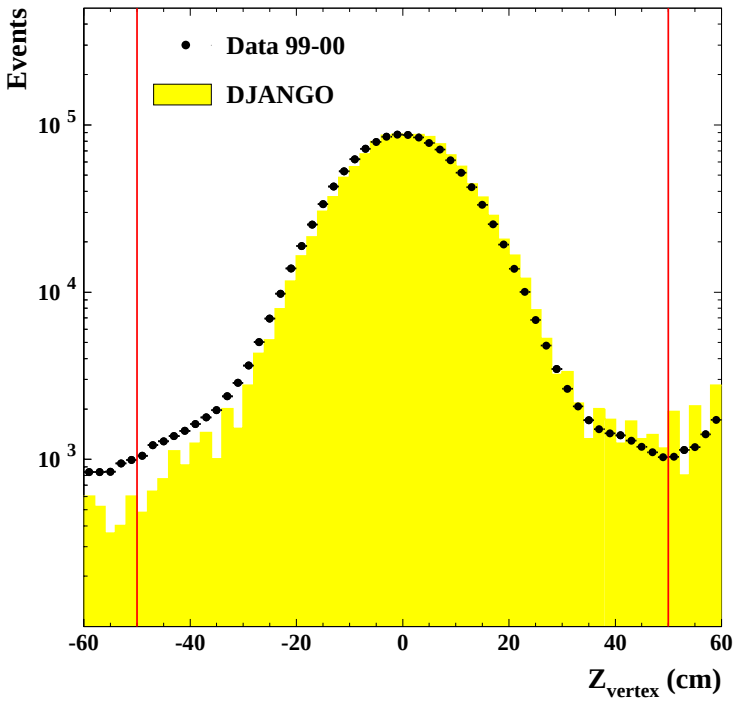

Figure 5.1: The reconstructed Z position of the vertex. The dots are data and the histogram is DJANGO Monte Carlo sample.

5.4.2 Reconstruction of electron

A scattered electron is searched for in CAL energy deposits by SINISTRA, an electromagnetic cluster finding algorithm [45]. SINISTRA uses a neural network to judge whether an electromagnetic cluster in the CAL is from an electromagnetic particles. The candidate with the highest electron probability is selected as the scattered electron. If the electron candidate is inside the CTD acceptance in the polar angle θ range of $15^\circ < \theta < 164^\circ$, an associated track for the CTD is required.

Due to the presence of the dead materials in front of the CAL, the electron energy correction is applied using the SRTD detector. When the electron is showered by the dead materials, the energy deposits in the SRTD increase, and at the same time the energy deposits in the CAL are loss. Thus, the electron energy is corrected as the following formula;

$$E_{\text{corrected } e'} = E_{\text{CAL}} + \alpha E_{\text{SRTD}}, \tag{5.1}$$

where α is a constant, and is set to 0.017, E_{CAL} is the energy deposits in the CAL, and E_{SRTD} is the energy deposits in the SRTD. $E_{\text{corrected } e'}$ and E_{CAL} have a unit of GeV, and E_{SRTD} has a unit of mip.

In this analysis, in order to reduce the contamination from other particles, the cut is applied to the energy of the scattered electron in DIS;

$$E_{e'} > 10 \text{ GeV} . \tag{5.2}$$

The efficiency to find the scattered electron after the selection is $\sim 100\%$ [46]. Figure 5.2 shows the distribution of E_e and θ_e after the DIS selection. The data is described fairly well by DIS MC sample generated by DJANGO.

5.4.3 Reconstruction of hadronic final state

The information of the CAL and the CTD is used for the reconstruction of the hadronic final state. Charged tracks in the CTD and energy deposits in the CAL are combined to form Energy Flow Objects (EFOs) [47].

The procedure of making the EFOs is the following. First, cells with the energy deposits in EMC, HAC1 and HAC2 sections are separately clustered into objects named as "cell islands". The cell islands are combined to form three dimensional objects called "cone islands". Then, charged tracks are extrapolated to the inner surface of the CAL and associated to the cone islands. Finally, the energy and momentum of the objects are determined either from the energy deposits in the CAL or from the momentum measured in the CTD, depending on the resolution in the measurements. For particles with charged track within the CTD acceptance and low momentum, the track information is used. On

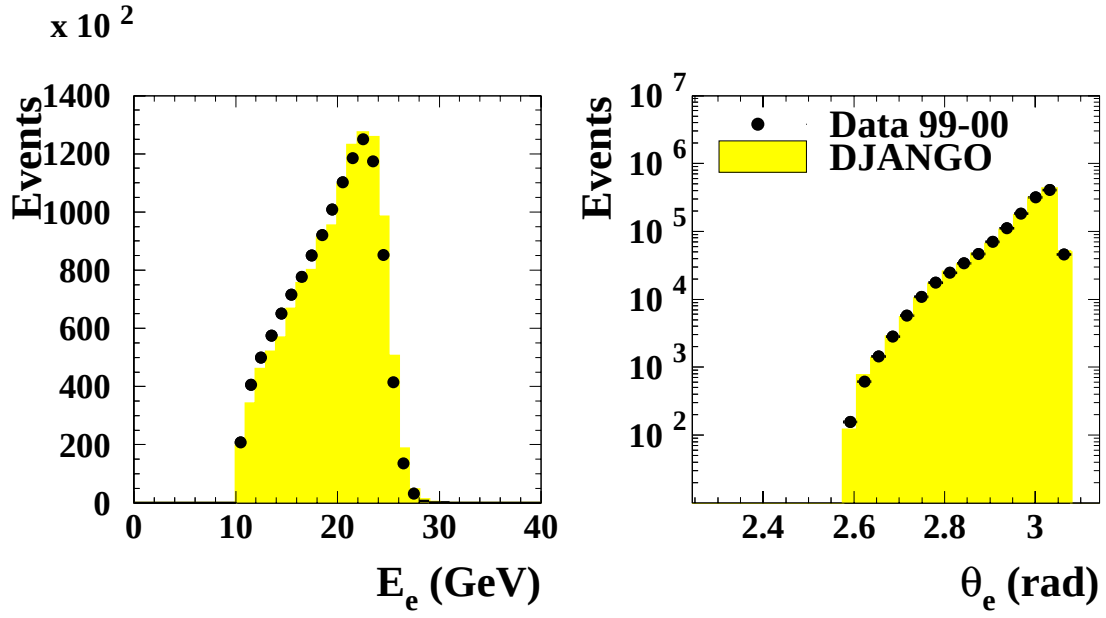

Figure 5.2: Distribution of the energy and angle of electron candidate

the other hand, for neutral particles, particles outside the CTD acceptance or particles with high momentum, the CAL energy is used. The reconstructed event vertex is used to determine the direction. Each EFO is assumed to be a massless particle.

Figure 5.3 shows an example of making EFOs from EMC and HAC sections in CAL. In figure, we can see four EMC cell islands and one HAC cell island clustered from the cells in EMC and HAC. The "2" and "3" EMC cell islands adjoin the "1" HAC cell island, and these three cell islands are joined and form one cone island. This combines a charged track and forms one EFO.

Energy correction for hadronic final state

It is necessary to correct EFOs to compensate the energy loss due to the dead materials in front of the CAL. The energy correction is applied to the EFOs whose energy is determined by the CAL energy. The energy correction for each EFO was performed with the following function formula;

$$E_{\text{corrected EFOs}} = f(E_{\text{EFO}}, \theta_{\text{EFO}}) E_{\text{EFO}} \ , \tag{5.3}$$

where E_{EFO} is the energy of the EFO, θ_{EFO} is the polar angle of the EFO, and the energy correction function $f(E_{\text{EFO}}, \theta_{\text{EFO}})$ is the following;

$$f(E_{\text{EFO}}, \theta_{\text{EFO}}) = 1 + \frac{\alpha}{E_{\text{EFO}}^{\beta}} \ , \tag{5.4}$$

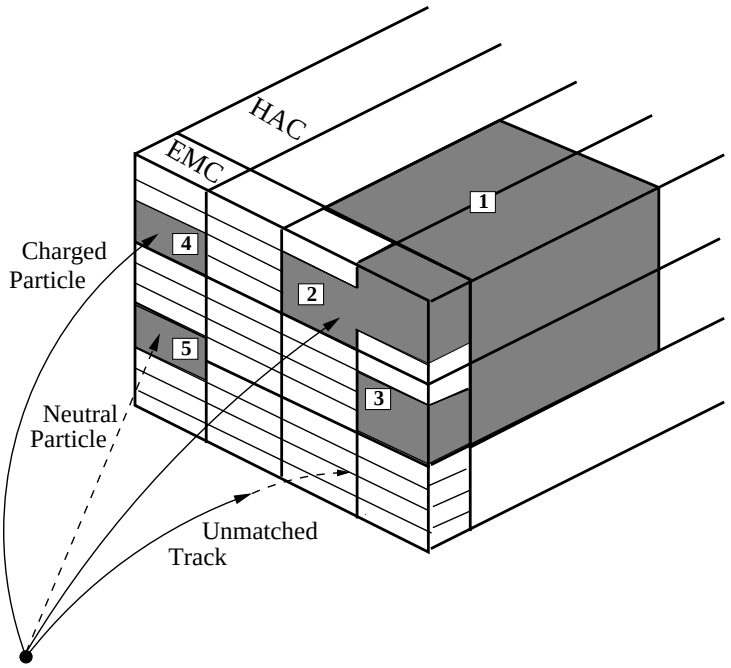

Figure 5.3: Schematic picture of EFOs

where α and β are functions of $\theta_{\rm EFO}$. These parameters are determined by using the energy and momentum conservation and the measurement of the electron energy. Data and Monte Carlo are corrected differently as shown in Figure 5.4. The fit is performed to minimize the difference of the transverse momentum P_T and y between the EFOs and the scattered electron.

5.4.4 Reconstruction of $E - p_Z$

From the energy and momentum conservation, the sum of $E - p_Z$ for all final particles is twice the electron beam energy;

$$\begin{aligned} E - p_Z &\equiv \sum_i (E_i - p_{Z,i}) \\ &= E_e - (-E_e) + E_p - E_p \\ &= 2E_e = 55 \text{ GeV} , \end{aligned} \tag{5.5}$$

where the sum i runs over all final state particles.

The reconstruction of $E - p_Z$ is done in the following way;

$$E - p_Z = (E_{e'} - p_{Z,e'}) + \sum_{i=\text{EFOs}} (E_i - p_{Z,i}) , \tag{5.6}$$

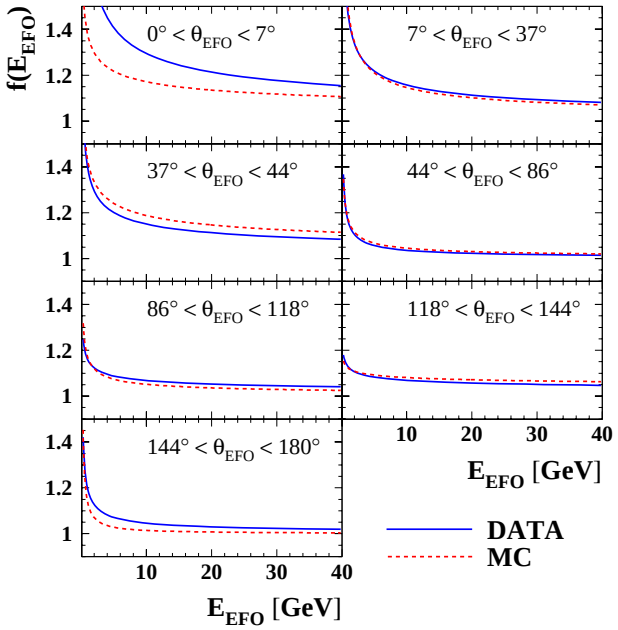

Figure 5.4: Distribution of the energy correction functions obtained for data and Monte Carlo in different θ_{EFO} regions.

where $E_{e'}$ and $p_{Z,e'}$ are the energy and the Z component of the momentum of the scattered electron, and E_i and $p_{Z,i}$ are the energy and Z component of momentum of EFOs. The sum i runs over the EFOs excluding the scattered electron. Figure 5.5 shows the distribution of $E - p_Z$.

In case of the photoproduction events, the scattered electron escapes to the rear beam hole. Then, $E - p_Z = 2E_e - 2E_{e'}$ is lower than the DIS events. Therefore, the photoproduction backgrounds can be reduced by requiring a large $E - p_Z \approx 2E_e$ (see Section 5.5).

5.4.5 Reconstruction of kinematic variables

As described in Section 2.1, it is enough to determine two kinematical variables to describe the DIS. Because the energy and angle of the hadronic final state can be measured as well as those of the scattered electron in the ZEUS detector, the kinematic variables in the DIS can be redundantly reconstructed by these two energies and two angles.

In this analysis, the double angle method (DA) [48] is mainly used to reconstruct the kinematic variables. This method relies on the θ_e and the hadronic angle (γ) which

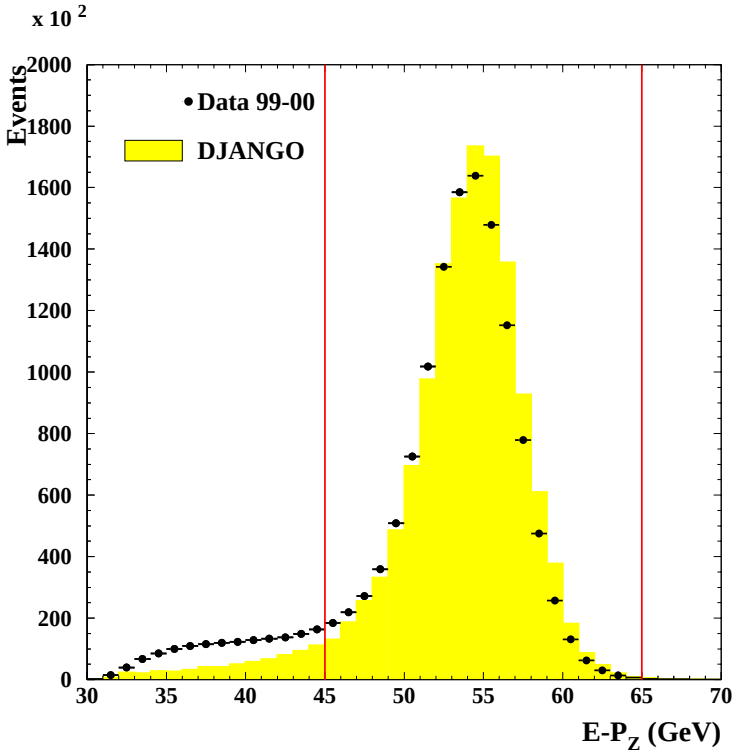

Figure 5.5: Distribution of $E - p_Z$

characterizes the hadronic final state. The angle γ is defined as:

$$\cos\gamma = \frac{\Big(\sum_{i=\mathrm{EFOs}} p_{T,i}\Big)^2 - \Big(\sum_{i=\mathrm{EFOs}} (E_i - p_{z,i})\Big)^2}{\Big(\sum_{i=\mathrm{EFOs}} p_{T,i}\Big)^2 + \Big(\sum_{i=\mathrm{EFOs}} (E_i - p_{z,i})\Big)^2} \tag{5.7}$$

where the sums are taken for all EFOs excluding that for the scattered electron. γ corresponds the polar angle of the struck quark in the simple quark parton model. The kinematic variables Q^2 and x are estimated from θ_e and γ as the following;

$$Q^2_{DA} = 4E_e^2 \cdot \frac{\sin\gamma(1+\cos\theta_e)}{\sin\gamma + \sin\theta_e - \sin(\theta_e+\gamma)} , \tag{5.8}$$

$$x_{DA} = \frac{E_e}{E_p} \cdot \frac{\sin\gamma + \sin\theta_e + \sin(\theta_e+\gamma)}{\sin\gamma + \sin\theta_e - \sin(\theta_e+\gamma)} . \tag{5.9}$$

The kinematic variable W for the DA can be reconstructed by the variable Q^2_{DA} and x_{DA} as following;

$$W^2_{DA} = \Big(\frac{1}{x_{DA}} - 1\Big) Q^2_{DA} . \tag{5.10}$$

The advantage of this DA method is that the method has little sensitivity to the uncertainty in the absolute energy measurement of the scattered electron and the EFOs, since the hadronic angle γ is obtained from the ratio of the energy of the EFOs.

5.5 DIS event selection

To summarize, DIS events are selected with the following selection cuts.

- The vertex requirement;

$$-50 \text{ cm} < Z_{\text{vertex}} < 50 \text{ cm} . \tag{5.11}$$

  This cut rejects the beam-gas and cosmic background

- $E - p_Z$ cut;

$$45 \text{ GeV} < E - p_Z < 65 \text{ GeV} . \tag{5.12}$$

  This cut eliminates the photoproduction background.

- The cut of the electron energy;

$$E_{e'} > 10 \text{ GeV} . \tag{5.13}$$

  In addition, the electron candidates entered in the following region are excluded in this analysis. This so-called Box cut is applied since it is difficult precisely to measure the electron around the rear beam pipe because of the presence of the large dead materials in front of the RCAL. The range of the cut [49] is specified with the X, Y position of the electron on the surface of the RCAL;

$$\begin{array}{lrcrcl}
(& -7 < X < 3 \text{ cm} & \text{and} & -10 < Y < 10 \text{ cm} &) & \text{or} \\
(& -14 < X < -7 \text{ cm} & \text{and} & -12 < Y < 12 \text{ cm} &) & \text{or} \\
(& 3 < X < 12 \text{ cm} & \text{and} & -12 < Y < 12 \text{ cm} &) & \text{or} \\
(& -16 < X < -14 \text{ cm} & \text{and} & 4 < Y < 12 \text{ cm} &) & \text{or} \\
(& -16 < X < -14 \text{ cm} & \text{and} & -12 < Y < -4 \text{ cm} &) & .
\end{array}$$

  Figure 5.6 shows the range of the cut on the surface of the RCAL.

- The kinematical cuts;

$$5 \text{ GeV}^2 < Q^2_{DA} < 100 \text{ GeV}^2 , \tag{5.14}$$

$$100 \text{ GeV} < W_{DA} < 250 \text{ GeV} . \tag{5.15}$$

  As shown in Figure 5.7, the acceptance to the low Q^2 region is small, mainly due to the Box cut. In this analysis, $Q^2_{DA} > 5$ GeV^2 is applied to keep high acceptance. The efficiency is $\sim 70\%$ at $Q^2_{DA} = 5$ GeV^2.

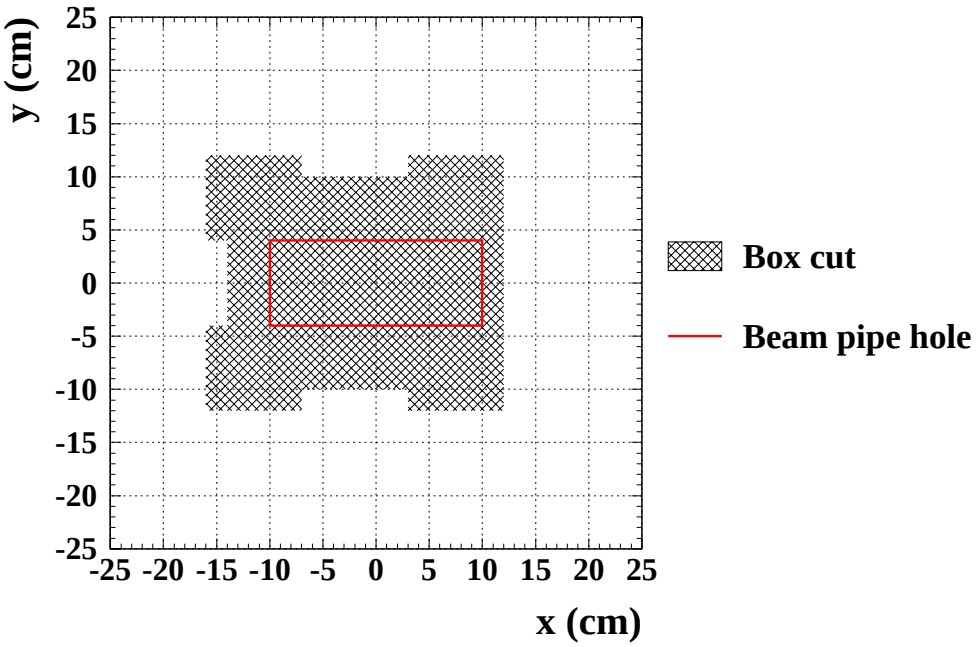

Figure 5.6: Overview of the shape of the Box cut

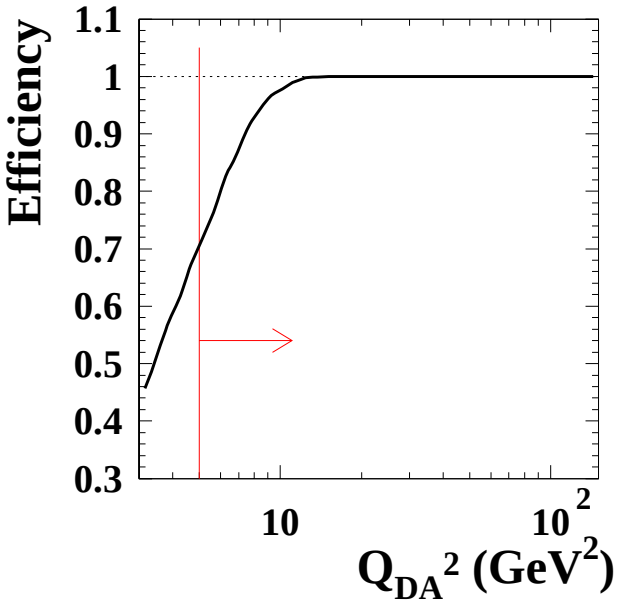

Figure 5.7: Efficiency of the Box cut

5.6 Diffractive event selection

The feature of diffractive events is a large rapidity gap between the undetected hadronic system with a small mass (typically just an intact proton) escaping in the forward beam pipe and the rests of the hadronic system. In the ZEUS detector, the FPC around the beam pipe in the forward direction helps to find the gap. It covers the range of the pseudorapidity η from $\eta \approx 3.8$ to $\eta \approx 5$ as described in Section 3.2.4.

5.6.1 $\eta_{\max}$ cut

$\eta_{\max}$ is defined as the pseudo-rapidity η of the most forward EFOs which has the energy deposit above 400 MeV. The distribution of $\eta_{\max}$ is in the upper figure of Figure 5.8. Non-diffractive DIS MC sample generated by DJANGO is also shown, normalized to the luminosity of data. The peak at $\eta_{\max} \approx 3.5$ corresponds to the non-diffractive events in which the proton remnant deposits the energy of the forward edge of the CAL. In the lower $\eta_{\max}$ region, the MC events significantly fall down and an excess at low values of $\eta_{\max}$ exists in the data. These are the diffractive events. Therefore, the cut of $\eta_{\max} < 2.8$ is used to the diffractive selections.

5.6.2 FPC energy cut

E_{FPC} is the total energy deposit in the FPC detector. The noise level of E_{FPC} is well below 1.0 GeV. $E_{\mathrm{FPC}} < 1.0$ GeV is imposed in addition to the $\eta_{\max}$ cut. This cut in combination with the $\eta_{\max}$ cut strongly suppresses the remaining non-diffractive events as shown in the lower figure of Figure 5.8.

5.6.3 Reconstruction of diffractive variables

M_X is the invariant mass of hadronic system, which is calculated from the four-momentum of EFOs as following;

$$M_X = \sqrt{\Big(\sum_{i=\mathrm{EFOs}} E_i\Big)^2 - \Big(\sum_{i=\mathrm{EFOs}} P_{x,i}\Big)^2 - \Big(\sum_{i=\mathrm{EFOs}} P_{y,i}\Big)^2 - \Big(\sum_{i=\mathrm{EFOs}} P_{z,i}\Big)^2}\,, \qquad (5.16)$$

where the sum i runs over all EFOs excluding the scattered electron. The diffractive variables, $x_{I\!P}$ and β, as described in Section 2.5, are calculated from Q^2_{DA}, W_{DA} and M_X;

$$x_{I\!P} = \frac{M_X^2 + Q^2_{DA}}{W^2_{DA} + Q^2_{DA}}\,, \qquad (5.17)$$

$$\beta = \frac{Q^2_{DA}}{Q^2_{DA} + M_X^2}\,. \qquad (5.18)$$

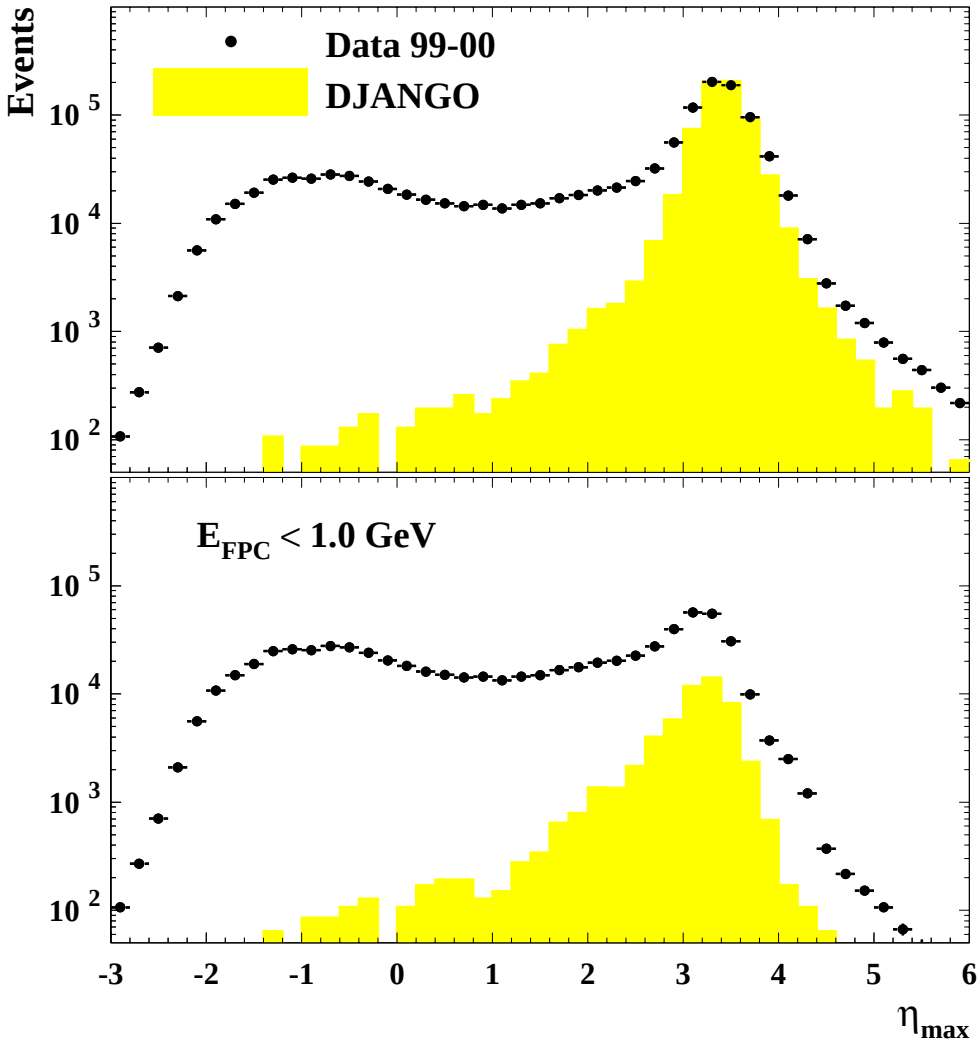

Figure 5.8: Distribution of $\eta_{\max}$ for DIS events (upper plot) and distribution of $\eta_{\max}$ after $E_{\mathrm{FPC}} < 1$GeV cut (lower plot).

Diffraction is characterized with small $x_{I\!P}$. For high $x_{I\!P}$, contributions from the other Reggeon exchange become dominant. $x_{I\!P} < 0.03$ is imposed in this analysis.

5.6.4 Summary of diffractive event selection

To summarize, following cuts are imposed to the selected diffractive DIS samples.

- $\eta_{\max} < 2.8$ and $E_{\mathrm{FPC}} < 1.0$ GeV
- $x_{I\!P} < 0.03$

Figure 5.9 shows the distribution of $x_{I\!P}$ as function of $\eta_{\max}$ for RAPGAP MC samples. The solid lines indicate the cut value of $x_{I\!P}$ and $\eta_{\max}$. $x_{I\!P}$ cut is applied in order to select a kinematic region in which the other reggeon contribution is reduced. These is a strong correlation between $\eta_{\max}$ and $x_{I\!P}$. The applied $\eta_{\max}$ cut keeps a good acceptance to the $x_{I\!P}$ region studied.

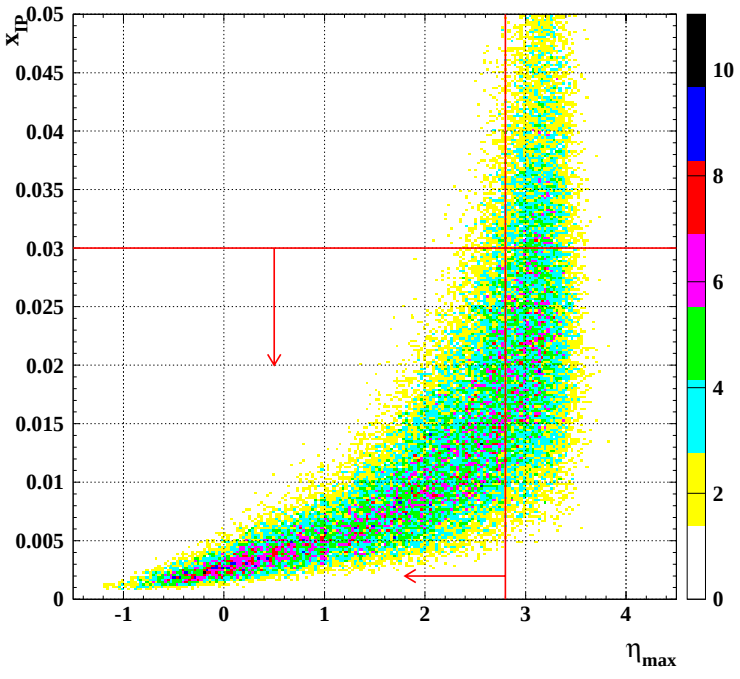

Figure 5.9: Distribution of $x_{I\!P}$ as function of $\eta_{\max}$. The dash lines indicate the cut values of $x_{I\!P}$ and $\eta_{\max}$.

5.7 Dijet event selection

5.7.1 Boost to γ^*-p frame

In the DIS, the electron is scattered with a significant transverse momentum. Since the hadronic system has p_T in the lab frame to balance with the scattered electron, this Lorentz frame is not suitable to find dijet events in DIS. Therefore, the jets are searched for in the γ^*-proton frame (γ^*-p frame). The axis of a collision between the virtual photon and the proton is aligned to the Z direction in this frame. The four-vectors of the hadronic final state particles are Lorentz transformed to the γ^*-p frame. Lorentz boost four-vectors for γ^*-p frame are the following;

$$\beta_x = \frac{P_x^{had}}{E^{had}} = \frac{-p_{X,e'}}{E_e + E_p - E_{e'}} , \tag{5.19}$$

$$\beta_y = \frac{P_y^{had}}{E^{had}} = \frac{-p_{Y,e'}}{E_e + E_p - E_{e'}} , \tag{5.20}$$

$$\beta_z = \frac{P_z^{had}}{E^{had}} = \frac{-E_e + E_p - p_{Z,e'}}{E_e + E_p - E_{e'}} , \tag{5.21}$$

$$\gamma = \frac{E^{had}}{W} = \frac{E_e + E_p - E_{e'}}{W_{el}} , \tag{5.22}$$

where P_x^{had},P_y^{had},P_z^{had} and E^{had} are the four-momentum of the hadronic system, which are estimated from the four-momentum of the scattered electron ($E_{e'}$, $p_{X,e'}$, $p_{Y,e'}$, $p_{Z,e'}$), using the energy and the momentum conservation. W_{el} is the invariant mass of hadronic system calculated using the electron information as following;

$$W_{el}^2 = 4E_eE_p - 2E_e(E_{e'} + p_{Z,e'}) - 2E_p(E_{e'} - p_{Z,e'}) . \tag{5.23}$$

5.7.2 Inclusive k_T algorithm

In this analysis, the inclusive k_T algorithm [50] in the longitudinal invariant mode [51] is used to find jets. This algorithm is explained here.

For every i and j pair of objects (such as particles), a closeness is defined as;

$$d_{ij} = \min(E_{Ti}^2, E_{Tj}^2)\Delta R^2 , \tag{5.24}$$

where $\Delta R^2 \equiv (\eta_i - \eta_j)^2 + (\phi_i - \phi_j)^2$. Considering $\Delta R \ll 1$ for small opening angle, the closeness d_{ij} is denoted as following;

$$d_{ij} = \min(E_{Ti}^2, E_{Tj}^2)\Delta R^2 \approx \min(E_i^2, E_j^2)\Delta\theta^2 \approx k_T^2 . \tag{5.25}$$

In addition to every object i, a closeness to the beam particles is defined as the following;

$$d_{ib} = E_{Ti}^2 R^2 , \tag{5.26}$$

where R is an adjustable parameter of the algorithm introduced in [51] and set to $R = 1$. If $\min\{d_{ij}\} < \min\{d_{ib}\}$, objects i and j are merged. In this analysis, the "p_T-scheme" is used to merge two objects like the following;

$$E_{Tij} = E_{Ti} + E_{Tj} , \tag{5.27}$$
$$\eta_{ij} = (E_{Ti}\eta_i + E_{Tj}\eta_j)/E_{Tij} , \tag{5.28}$$
$$\phi_{ij} = (E_{Ti}\phi_i + E_{Tj}\phi_j)/E_{Tij} . \tag{5.29}$$

If $\min\{d_{ib}\} < \min\{d_{ij}\}$, object i becomes a jet and is removed from the list. These steps are repeated until all objects become jets. Jets are reconstructed by three variables, the transverse energy of jets $E_{T,\mathrm{jets}}$, the pseudo-rapidity of jets η_{jets} and the azimuthal angle of jets ϕ_{jets}.

5.7.3 Reconstruction and selection of dijets

The procedure of the reconstruction and selection of jets is described here. First, all EFOs are boosted to the γ^*-p frame as described in Section 5.7.1. Next, the boosted EFOs in γ^*-p frame are used to reconstruct jets using k_T algorithm as described in Section 5.7.2. The energy threshold of $E_{T,\mathrm{jet}}$ is required in the γ^*-p frame as following;

$$E^*_{T,\mathrm{jet1}} > 5 \text{ GeV} \text{ and } E^*_{T,\mathrm{jet2}} > 4 \text{ GeV} , \tag{5.30}$$

where $E^*_{T,\mathrm{jet1}}$ is the transverse energy of jets with the highest $E^*_{T,\mathrm{jet}}$ and $E^*_{T,\mathrm{jet2}}$ is the transverse energy of jets with the second highest $E^*_{T,\mathrm{jet}}$. The superscript "*" indicates that it was reconstructed in the γ^*-p frame. The thresholds of E_T on the two jets are asymmetric in this analysis since the NLO QCD prediction is not stable when the two thresholds are identical [52].

To avoid a bias from the detector uncoverage, the jets need to be well confined in the ZEUS detector. Therefore, these jets in the γ^*-p frame are boosted back to the lab frame and a cut on η_{jets} is set as following;

$$-2.0 < \eta^{\mathrm{lab}}_{\mathrm{jets}} < 2.0 , \tag{5.31}$$

where the superscript "lab" indicates that it is reconstructed in the laboratory frame.

5.7.4 Reconstruction of dijet variables

From the four-momentum of the jets, $z^{\mathrm{obs}}_{I\!P}$ and $x^{\mathrm{obs}}_{\gamma}$ can be reconstructed.

Reconstruction of $z_{I\!P}^{\mathbf{obs}}$

$z_{I\!P}^{\rm obs}$ is reconstructed by:

$$z_{I\!P}^{\rm obs} = \frac{Q_{DA}^2 + M_{12}^2}{Q_{DA}^2 + M_X^2} \,, \tag{5.32}$$

where M_{12} is the invariant mass of two highest E_T jets and M_X is the mass of the hadronic system.

Reconstruction of $x_\gamma^{\mathbf{obs}}$

$x_\gamma^{\rm obs}$ is reconstructed by:

$$x_\gamma^{\rm obs} = \frac{\sum\limits_{i=1,\,2} (E_{{\rm jet}i}^{\rm lab} - p_{z,{\rm jet}i}^{\rm lab})}{\sum\limits_{i={\rm EFOs}} (E_i - p_{z,i})} \,. \tag{5.33}$$

5.8 Backgrounds

Non-diffraction and the proton dissociation events are considered as the background events in this analysis. These background events need to be subtracted from the selected events sample. The estimation of a amount of these backgrounds is described in this section.

5.8.1 Subtraction of non-diffractive background

The non-diffractive background is estimated by using DJANGO MC sample. The fraction of non-diffractive background after all selection cuts is $2.3 \pm 0.6\%$(stat.) on average. Since this value is small, non-diffractive background is neglected in this analysis.

5.8.2 Subtraction of the proton dissociation

In this analysis, the cross sections are measured for the single diffraction, where the forward system consists of a proton only. It is possible that low mass double dissociation events pass the diffractive selection cuts, when all forward particles are escaped to the beam pipe.

Since either RAPGAP or SATRAP cannot simulate the proton dissociation, the contribution is estimated with a soft diffraction model, EPSOFT MC, assuming that the behaviour of the forward system is independent whether the rests contain a hard collision or not.

In this estimation, the absolute value of the proton dissociation needs to be determined experimentally. For this purpose, an event selection to select the proton dissociation is made. For the proton dissociation events with high mass, the part of the forward system can be caught by the FPC and the first inner ring of the FCAL. To find a gap between the forward system and the rests, a new $\eta'_{\rm max}$ is introduced. $\eta'_{\rm max}$ is determined in the same way as $\eta_{\rm max}$ except that the calculation of $\eta'_{\rm max}$ dose not include the particles in $\eta > 2.37$ to allow the proton dissociation system to deposit some energy for $\eta > 2.37$, which correspond approximately the outer edge of the first inner ring of the FCAL (see Figure 5.10). To ensure a large rapidity gap between the proton dissociation and the hadronic system X, the cut of $\eta'_{\rm max} < 0.5$ was applied. Then, the following two samples are selected;

- $E_{\rm FPC} + E_{\rm FCAL\ 1st\ IR} < 1.0$ GeV, corresponding to the final sample,
- $E_{\rm FPC} + E_{\rm FCAL\ 1st\ IR} > 1.0$ GeV, corresponding to the proton dissociation enriched sample,

where $E_{\rm FCAL\ 1st\ IR}$ is the energy deposit of the first inner ring of FCAL. For the second sample, $E_{\rm FPC}+E_{\rm FCAL\ 1st\ IR}$ is plotted in Figure 5.11. The normalization factor of EPSOFT is determined by fitting the measured energy spectrum.

The determination procedure of the normalization factor is the following. The selected events in the range of $0 < E_{\rm FPC} + E_{\rm FCAL\ 1st\ IR} < 30$ GeV is divided into 30 bins. The χ^2 is determined as:

$$\chi^2 = \sum_i \Big(\frac{A \cdot N_i^{\rm EPSOFT} + B \cdot N_i^{\rm SATRAP} - N_i^{\rm data}}{\sigma_i^{\rm data}} \Big)^2 , \tag{5.34}$$

where A and B are the two free parameters in the fit, $N_i^{\rm EPSOFT}$ and $N_i^{\rm SATRAP}$ are the number of selected events in the bin i of EPSOFT and SATRAP, respectively. $\sigma_i^{\rm data}$ is the statistical error of data in the bin i. For this χ^2, The minimisation for the two free parameters in the fit is performed. SATRAP and EPSOFT are normalized using the normalization factor obtained by these procedure.

From the result of the fit, 43.7 events remained in the range of $E_{\rm FPC} + E_{\rm FCAL\ 1st\ IR} <$ 1.0 GeV, and 28.1 events remained in the range of $E_{\rm FPC} + E_{\rm FCAL\ 1st\ IR} > 1.0$ GeV. On the other hand, for data, 249 events remained in the range of $E_{\rm FPC} + E_{\rm FCAL\ 1st\ IR} < 1.0$ GeV, and 27 events were in the range of $E_{\rm FPC} + E_{\rm FCAL\ 1st\ IR} > 1.0$ GeV. From these obtained values, the fraction of the proton dissociation is determined as following;

$$f_{p\,\rm diss} = \frac{43.7}{249} \times \frac{27}{28.1} = 16.8 \pm 3.4\% , \tag{5.35}$$

where the error is statistical only. The results is consistent with the value $16\pm4\%$ obtained by a previous analysis in D^* production [53], where the better statistics (about 2%) were

available. Assuming that the contribution of the proton dissociation is independent of all kinematic variables, the fraction 16% of the proton dissociation is subtracted from all measured cross sections. 4% is used for the check of the systematic uncertainty. The subtraction of the proton dissociation is performed later in Chapter 6.

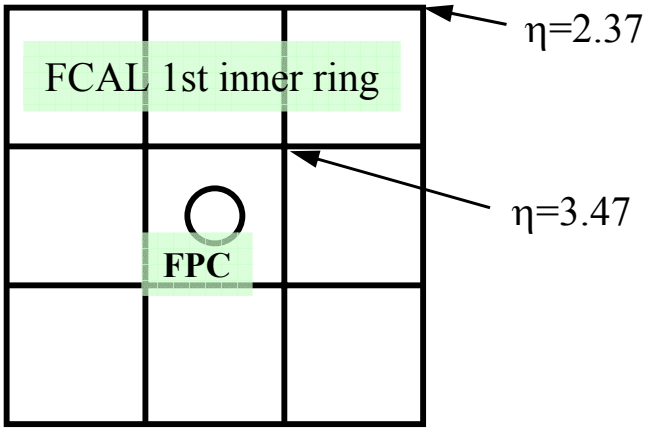

Figure 5.10: η of the points at the face of FPC and FCAL 1st inner ring

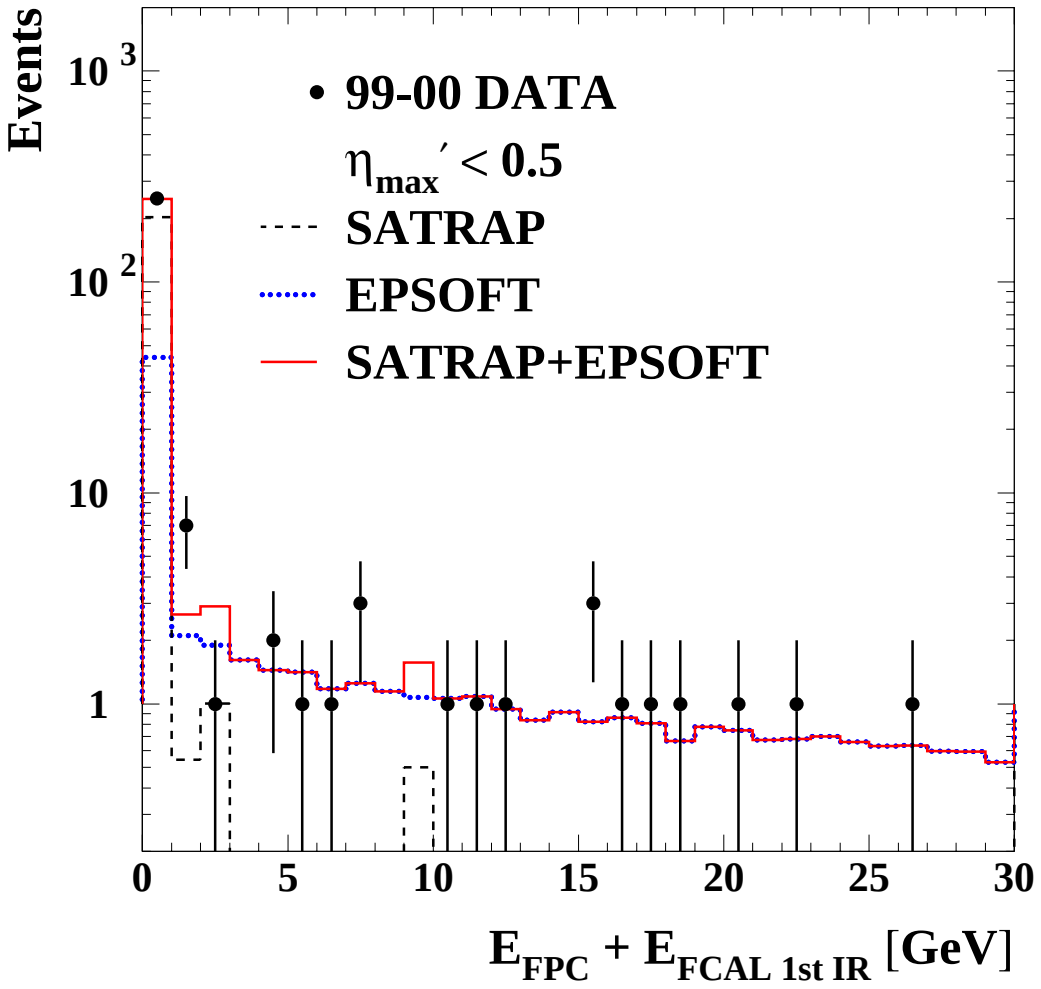

Figure 5.11: Distribution of the sum of the energy deposit in FPC and FCAL first inner ring.

5.9 Summary of event selections

Table 5.1 shows a summary of event selections. After all selections, 3711 events remains. Figure 5.12–5.14 shows the comparison of data with RAPGAP MC sample after the selections. RAPGAP MC samples are normalized to the data. The subtraction of the proton dissociation is not performed in these figure. Figure 5.12 shows the distribution of the event kinematic variables, Q^2_{DA}, W_{DA}, $\log_{10} x_{I\!P}$ and $\log_{10} \beta$. The data tends to have more higher Q^2 events than the MC. The other distribution are reasonably well reproduced by the MC. Figure 5.13 show the distribution of the jet variables, $E^*_{T,\mathrm{jet}}$, η^*_{jet}, and M_X. In these plots, both the first and second jets are included. $E^*_{T,\mathrm{jet}}$ and η^*_{jet} distributions are reproduced by the MC. In η^*_{jet} distribution, data is slightly shifted in forward direction. The distribution of M_X is well described by the MC. The average value of M_X is ~ 20 GeV. Figure 5.14 is the distribution of the $z^{\mathrm{obs}}_{I\!P}$ and $x^{\mathrm{obs}}_{\gamma}$. $x^{\mathrm{obs}}_{\gamma}$ peaks at 1, which suggest that the resolved photon contribution is small. The MC describes the distribution of $x^{\mathrm{obs}}_{\gamma}$ well. In summary, the data is reasonable described by RAPGAP MC.

	Event Selections
DIS selection	-50 cm $< Z_{\mathrm{vertex}} < 50$ cm 45 GeV $< E - p_Z <$ 65 GeV Number of electron candidate ≥ 1 $E_{e'} > 10$ GeV The Box cut 5 GeV$^2 < Q^2_{DA} <$ 100 GeV^2 100 GeV $< W_{DA} <$ 250 GeV
Diffractive selection	$\eta_{\mathrm{max}} < 2.8$ $E_{\mathrm{FPC}} < 1.0$ GeV $x_{I\!P} < 0.03$
Jets selection	$N^*_{\mathrm{jet}} \geq 2$ $E^*_{T,1\mathrm{jet}} > 5$ GeV and $E^*_{T,2\mathrm{jet}} > 4$ GeV $-2.0 < \eta^{\mathrm{lab}}_{\mathrm{jets}} < 2.0$

Table 5.1: Summary of event selections

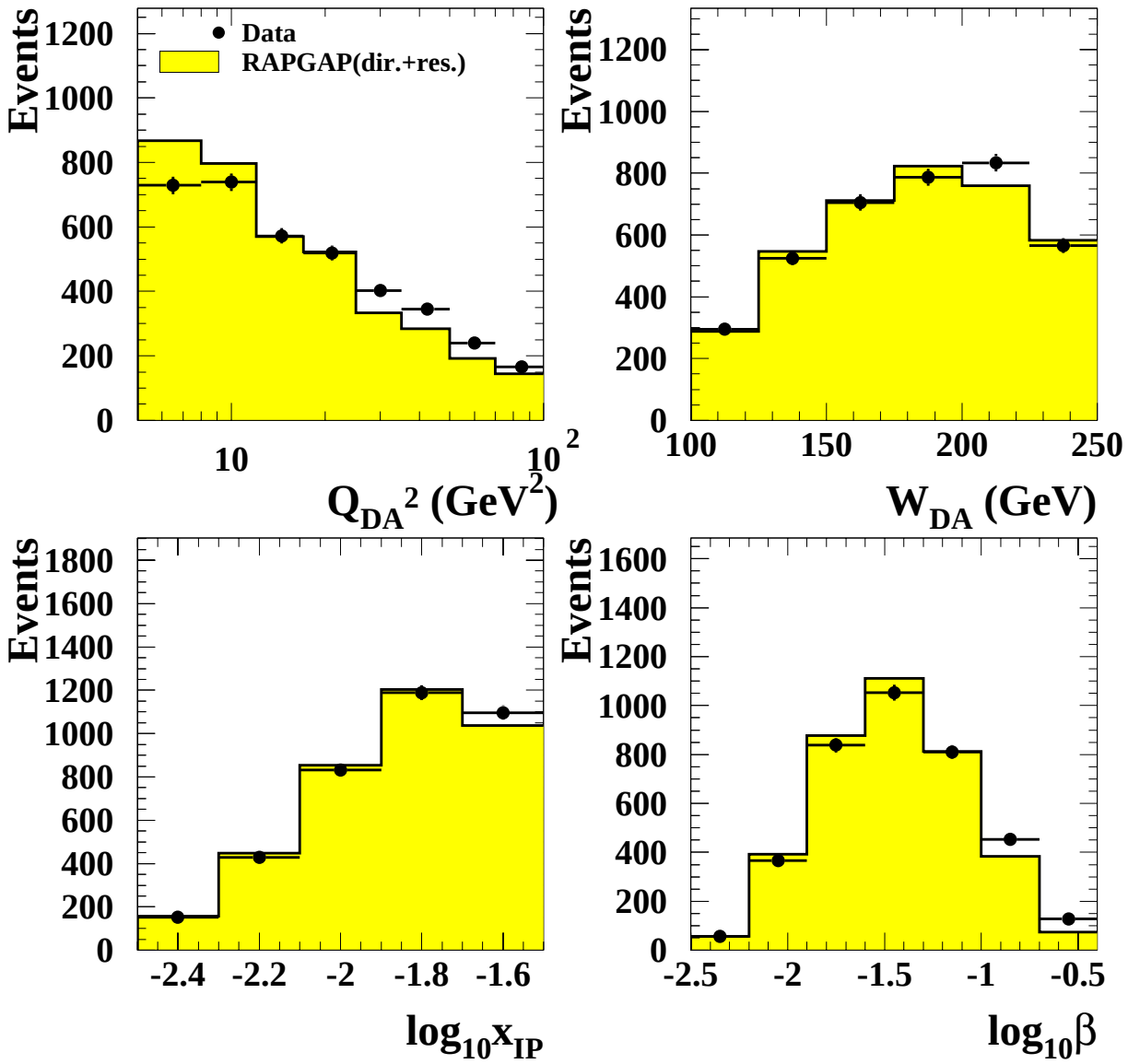

Figure 5.12: Control plots for Q^2_{DA}, W_{DA}, $\log_{10} x_{I\!P}$ and $\log_{10} \beta$. The data are shown as dots and the error bars represent the statistical uncertainty. The shaded histogram is RAPGAP Monte Carlo with resolved photon processes. RAPGAP is normalized to data.

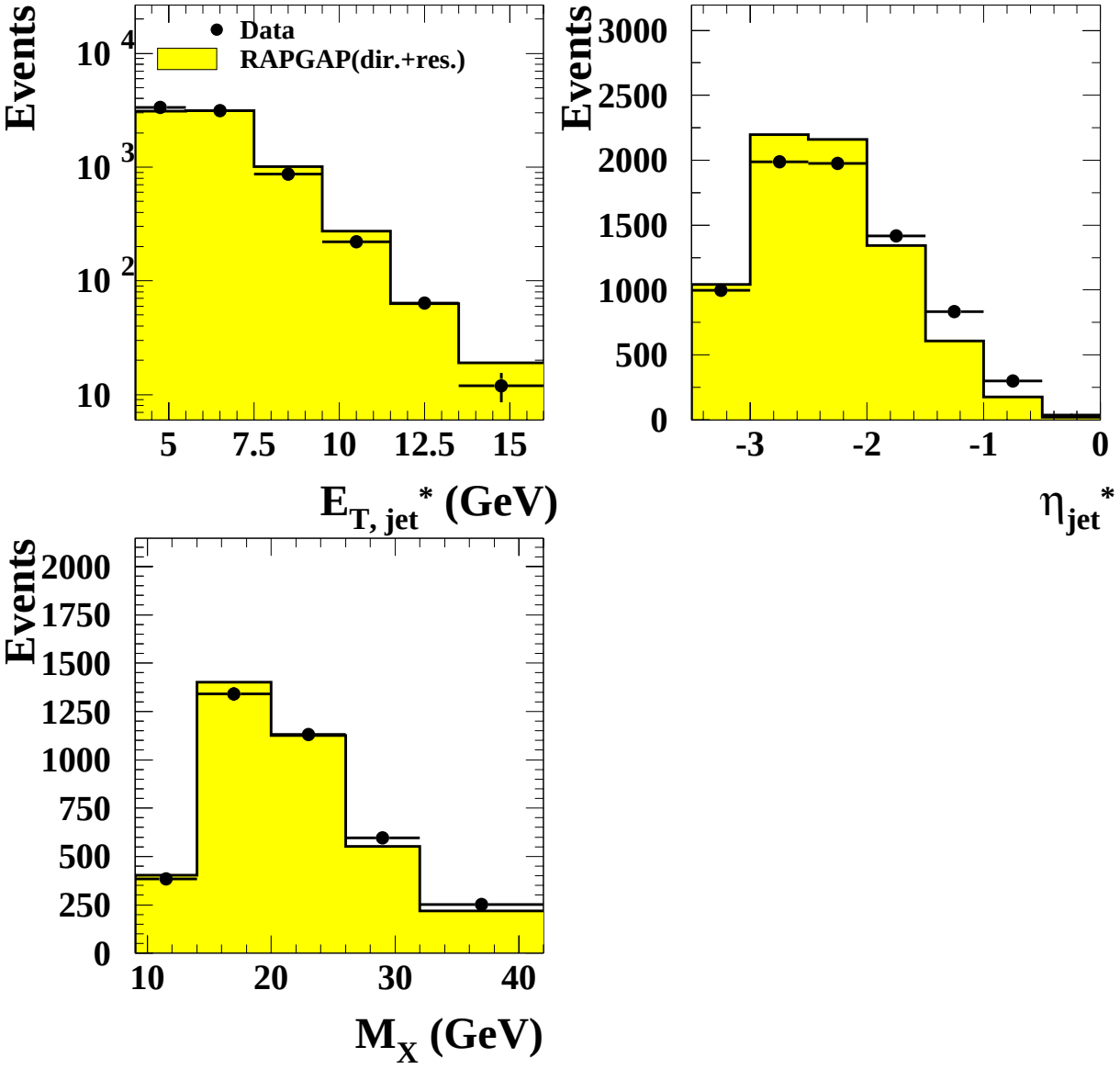

Figure 5.13: Control plots for $E^*_{T,\text{jets}}$, η^*_{jets} and M_X. The data are shown as dots and the error bars represent the statistical uncertainty. The shaded histogram is RAPGAP Monte Carlo with resolved photon processes. RAPGAP is normalized to data.

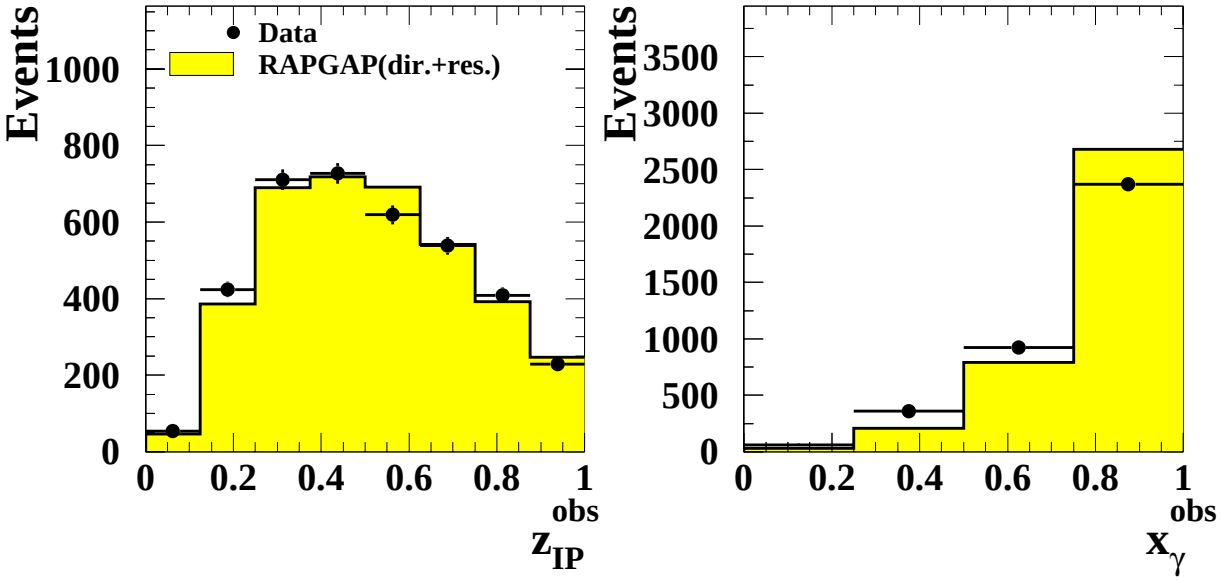

Figure 5.14: Control plots for $z_{I\!P}^{\rm obs}$ and $x_\gamma^{\rm obs}$. The data are shown as dots and the error bars represent the statistical uncertainty. The shaded histogram is RAPGAP Monte Carlo with resolved photon processes. RAPGAP is normalized to data.

Chapter 6

Cross section measurement

From the selected diffractive dijet sample, the cross sections of dijet process in diffractive DIS as functions of Q^2, W, $\log_{10} x_{I\!P}$, $\log_{10} \beta$, $E^*_{T,\mathrm{jets}}$, η^*_{jets}, M_X, $z^{\mathrm{obs}}_{I\!P}$ and $x^{\mathrm{obs}}_{\gamma}$ are measured. This chapter describes the procedure of the cross section measurement and the estimation of systematic uncertainties.

6.1 Definition of cross sections

By using data samples selected by the cuts in Table 5.1 in Chapter 5, the cross section of dijets in diffractive deep-inelastic scattering are measured in the following kinematic range.

- $5 < Q^2 < 100$ GeV^2
- $100 < W < 250$ GeV
- $x_{I\!P} < 0.03$
- $N^*_{\mathrm{jets}} \geq 2$
- $E^*_{T,\mathrm{jet1}} > 5$ GeV and $E^*_{T,\mathrm{jet2}} > 4$ GeV
- $-3.5 < \eta^*_{\mathrm{jet}} < 0.0$

where the superscript "*" indicates that the variable is in the γ^*-p frame.

In this kinematic range, cross sections are measured as functions of Q^2, W, $\log_{10} x_{I\!P}$, $\log_{10} \beta$, $E^*_{T,\mathrm{jets}}$, η^*_{jets}, M_X, $z^{\mathrm{obs}}_{I\!P}$ and $x^{\mathrm{obs}}_{\gamma}$. These cross sections are measured at hadron level, and corrected for the QED radiative effect (see Section 6.2.2). The kinematic ranges given above are taken as the same as the range used in the event selections.

6.2 Cross section calculation

The cross section in bin i is calculated with the following formula using the selected events;

$$\left(\frac{d\sigma}{dX}\right)_i = \frac{(1 - f_{p\,\mathrm{diss}}) \cdot \mathcal{C}_i^{\mathrm{rad}} \cdot \mathcal{C}_i^{\mathrm{acc}} \cdot N_i^{\mathrm{data}}}{\mathcal{L}_{\mathrm{data}} \cdot \Delta X_i} \,, \tag{6.1}$$

where N_{data} is the number of selected events in the bin i, $\mathcal{L}_{\mathrm{data}} = 65.2$ pb^{-1} is the integrated luminosity of the data, ΔX is the width of the bin i, $\mathcal{C}_i^{\mathrm{rad}}$ is the radiative correction factor, $\mathcal{C}_i^{\mathrm{acc}}$ is the acceptance correction factor, and $f_{p\,\mathrm{diss}}$ is the fraction of the proton dissociation. $f_{p\,\mathrm{diss}}$ is applied to $16 \pm 4\%$ (see Section 5.8.2). The correction factors $\mathcal{C}_i^{\mathrm{rad}}$ and $\mathcal{C}_i^{\mathrm{acc}}$ are explained in Section 6.2.1 in detail.

6.2.1 Bin-by-bin correction

Since RAPGAP MC samples describe data well (see Chapter 5), the acceptance can be estimated using this MC. The hadron level cross sections were obtained from detector level distributions for each bin by using the correction factors for RAPGAP MC sample.

The acceptance correction factor in bin i is calculated as

$$\mathcal{C}_i^{\mathrm{acc}} = \frac{N_i^{\mathrm{had}}}{N_i^{\mathrm{det}}} \,, \tag{6.2}$$

where N_i^{had} is the number of events generated in hadron level in the bin i, and N_i^{rec} is the number of events reconstructed in detector level in bin i.

The purity is defined as

$$\mathcal{P}_i = \frac{N_i^{\mathrm{had}\cap\mathrm{det}}}{N_i^{\mathrm{det}}} \,, \tag{6.3}$$

where $N_i^{\mathrm{had}\cap\mathrm{det}}$ is the number of events generated in hadron level in bin i and reconstructed in detector level in the same bin. High purity indicates that the migration to outside the measured bin is small. The efficiency is defined as

$$\mathcal{E}_i = \frac{N_i^{\mathrm{had}\cap\mathrm{det}}}{N_i^{\mathrm{had}}} \,, \tag{6.4}$$

The relation between these quantities are the following:

$$\mathcal{C}_i^{\mathrm{acc}} = \frac{\mathcal{P}_i}{\mathcal{E}_i} \,. \tag{6.5}$$

For each bins of all variables, acceptance correction factor, purity and efficiency are calculated.

To optimize the width of the bin, the migration efficiency is introduced. The migration efficiency is calculated as:

$$\mathcal{E}_i^{\rm mig} = \frac{N_i^{\rm had\cap det}}{N_i^{\rm had\cap (all\ cuts)}} \ , \tag{6.6}$$

where $N_i^{\rm had\cap (all\ cuts)}$ is the number of events generated in hadron level in the bin i and passed all selection cuts in detector level. The selection efficiency is calculated as:

$$\mathcal{E}_i^{\rm sel} = \frac{N_i^{\rm had\cap (all\ cuts)}}{N_i^{\rm had}} \ , \tag{6.7}$$

These values have the following relation to the efficiency $\mathcal{E}$;

$$\mathcal{E} = \mathcal{E}^{\rm sel} \cdot \mathcal{E}^{\rm mig} \ . \tag{6.8}$$

Figure 6.1–6.9 shows $\mathcal{P}$, $\mathcal{E}$, $\mathcal{E}^{\rm sel}$, $\mathcal{E}^{\rm mig}$, and $\mathcal{C}^{\rm acc}$ for all kinematic variables. The purity is typically about 0.4–0.5. The acceptance correction factor is typically a factor of 2–3, but as large as 5 for some kinematic range. The migration efficiency for all variables is higher than 0.4. The selection efficiency is about 0.2.

6.2.2 QED radiative correction

The measured cross sections at this stage obtained with $\mathcal{C}^{\rm acc}$ does not remove the effects of photon radiations from the electron. For a comparison with the theory, which does not calculate the photon radiation effect, they are converted to the Born level cross sections for the Quantum-Electro-Dynamics (QED) processes. The QED radiative correction factor is estimated by using both SATRAP MC with and without radiation from the following formula;

$$\mathcal{C}_i^{\rm rad} = \frac{N^{\rm had}_{\rm without\ rad}}{N^{\rm had}_{\rm with\ rad}} \ , \tag{6.9}$$

where $N^{\rm had}_{\rm without\ rad}$ is the number of events at the hadron level from the MC without QED radiative correction, and $N^{\rm had}_{\rm with\ rad}$ is the number of events at the hadron level with QED radiative correction. The value of $\mathcal{C}^{\rm rad}$ are shown in Table 6.1, 6.3, 6.5, 6.7, 6.9, 6.11, 6.13, 6.15, 6.17. They are about 5–10 %.

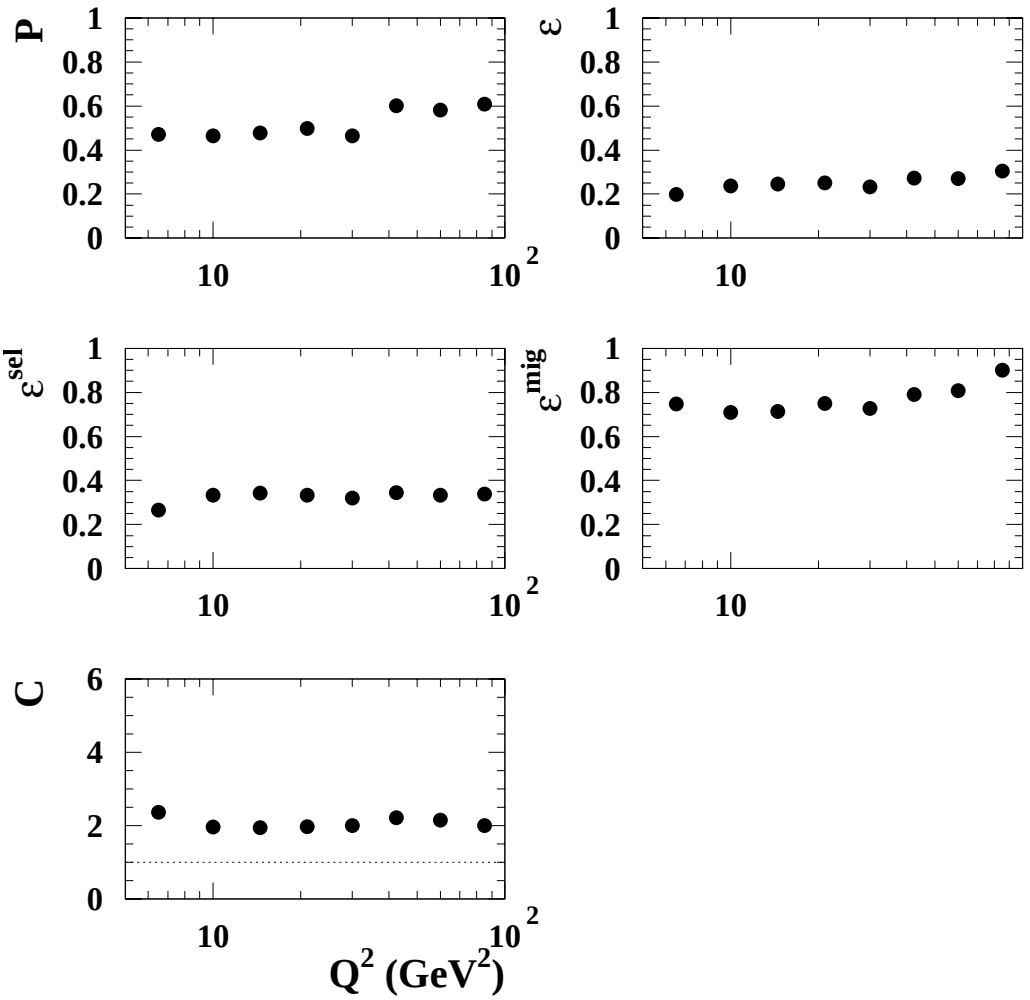

Figure 6.1: The purity $\mathcal{P}$, the efficiency $\mathcal{E}$, the selection efficiency $\mathcal{E}^{\rm sel}$, the migration efficiency $\mathcal{E}^{\rm mig}$, and the acceptance correction factor $\mathcal{C}^{\rm acc}$ of Q^2

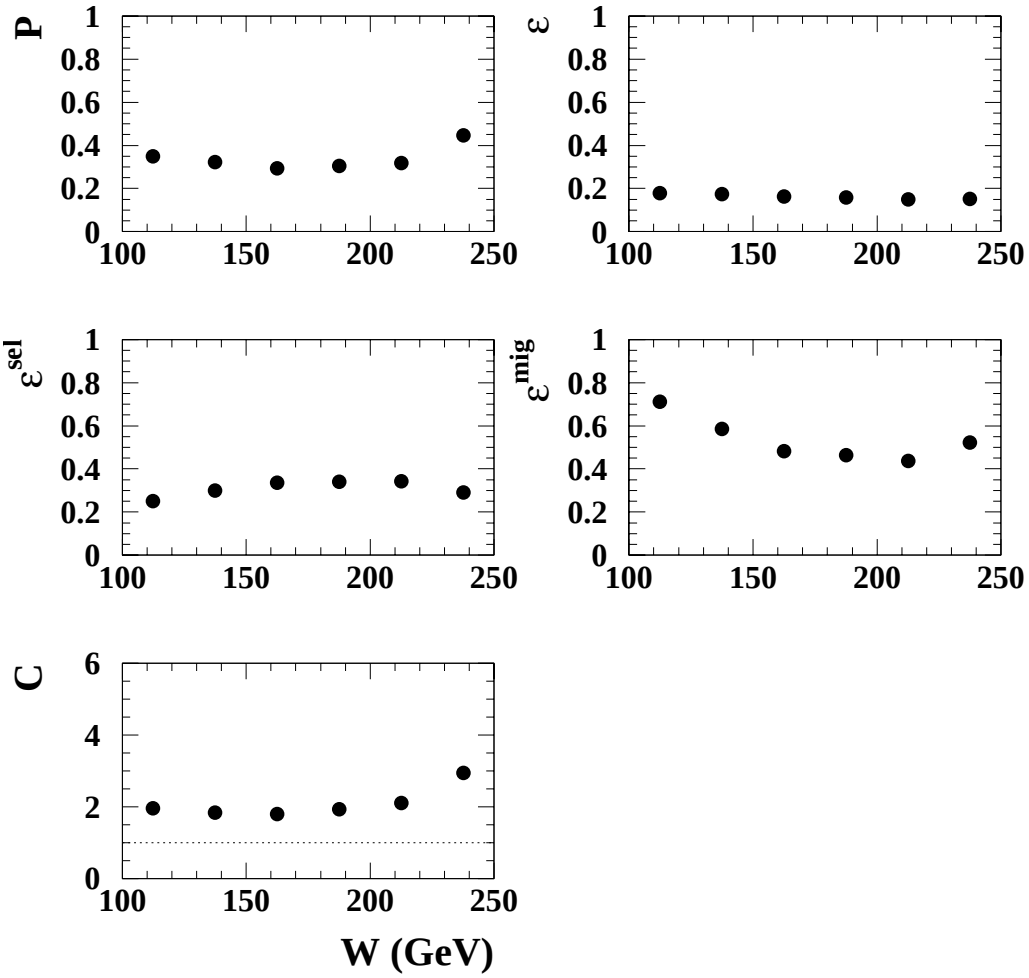

Figure 6.2: The purity $\mathcal{P}$, the efficiency $\mathcal{E}$, the selection efficiency $\mathcal{E}^{\rm sel}$, the migration efficiency $\mathcal{E}^{\rm mig}$, and the acceptance correction factor $\mathcal{C}^{\rm acc}$ of W

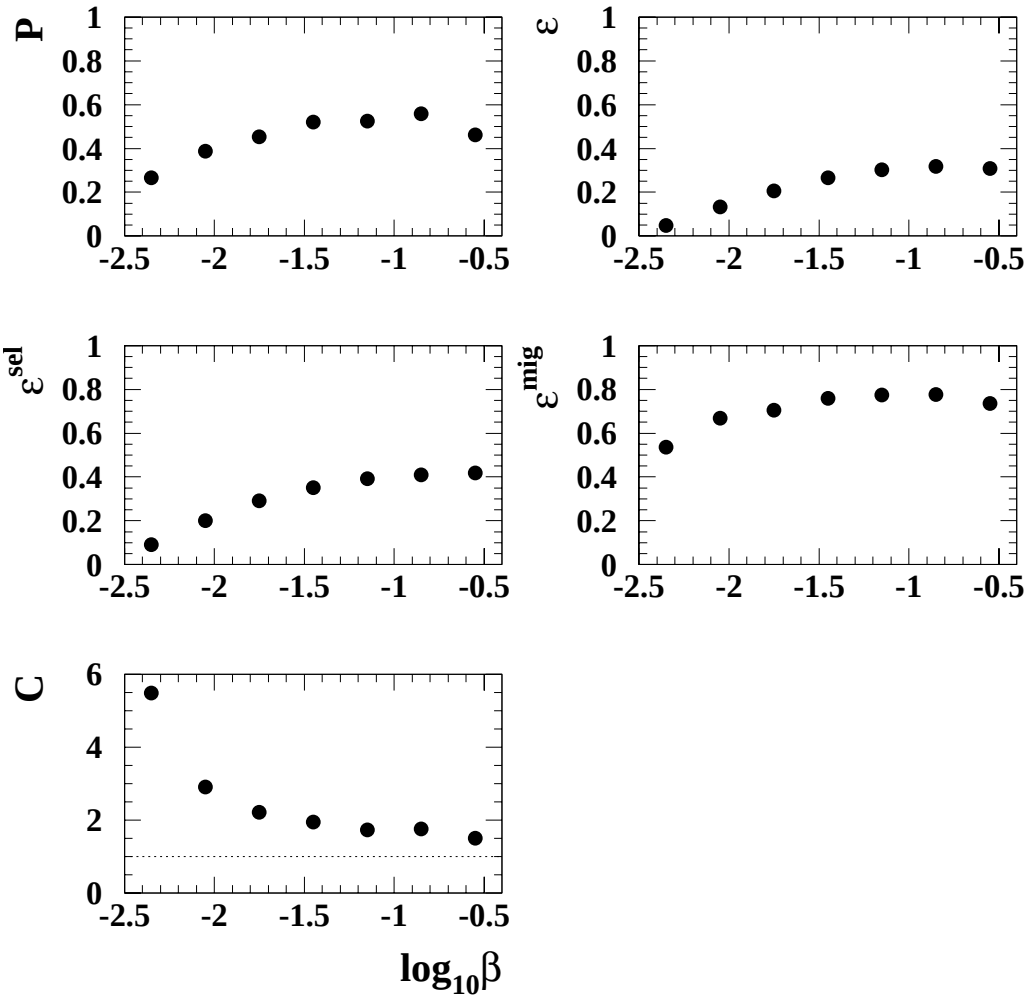

Figure 6.3: The purity $\mathcal{P}$, the efficiency $\mathcal{E}$, the selection efficiency $\mathcal{E}^{\mathrm{sel}}$, the migration efficiency $\mathcal{E}^{\mathrm{mig}}$, and the acceptance correction factor $\mathcal{C}^{\mathrm{acc}}$ of $\log_{10}\beta$

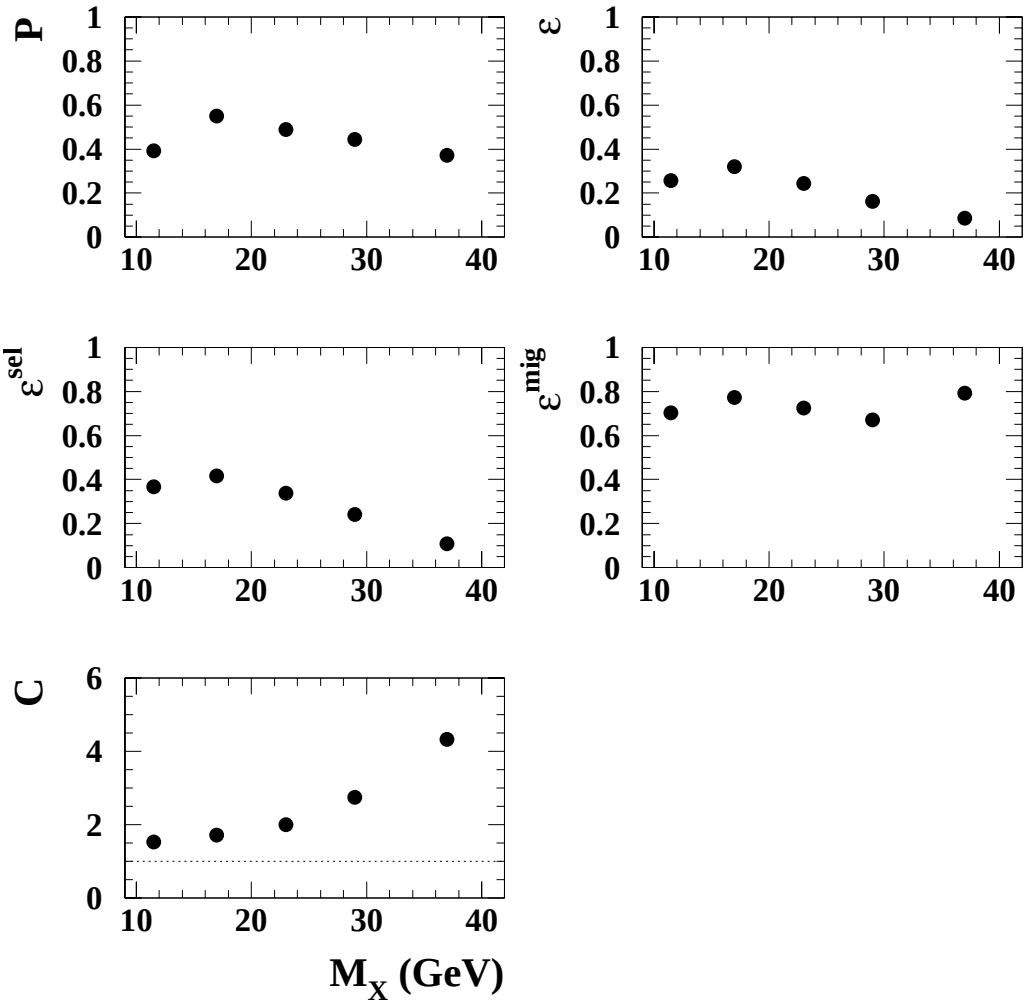

Figure 6.4: The purity $\mathcal{P}$, the efficiency $\mathcal{E}$, the selection efficiency $\mathcal{E}^{\rm sel}$, the migration efficiency $\mathcal{E}^{\rm mig}$, and the acceptance correction factor $\mathcal{C}^{\rm acc}$ of M_X

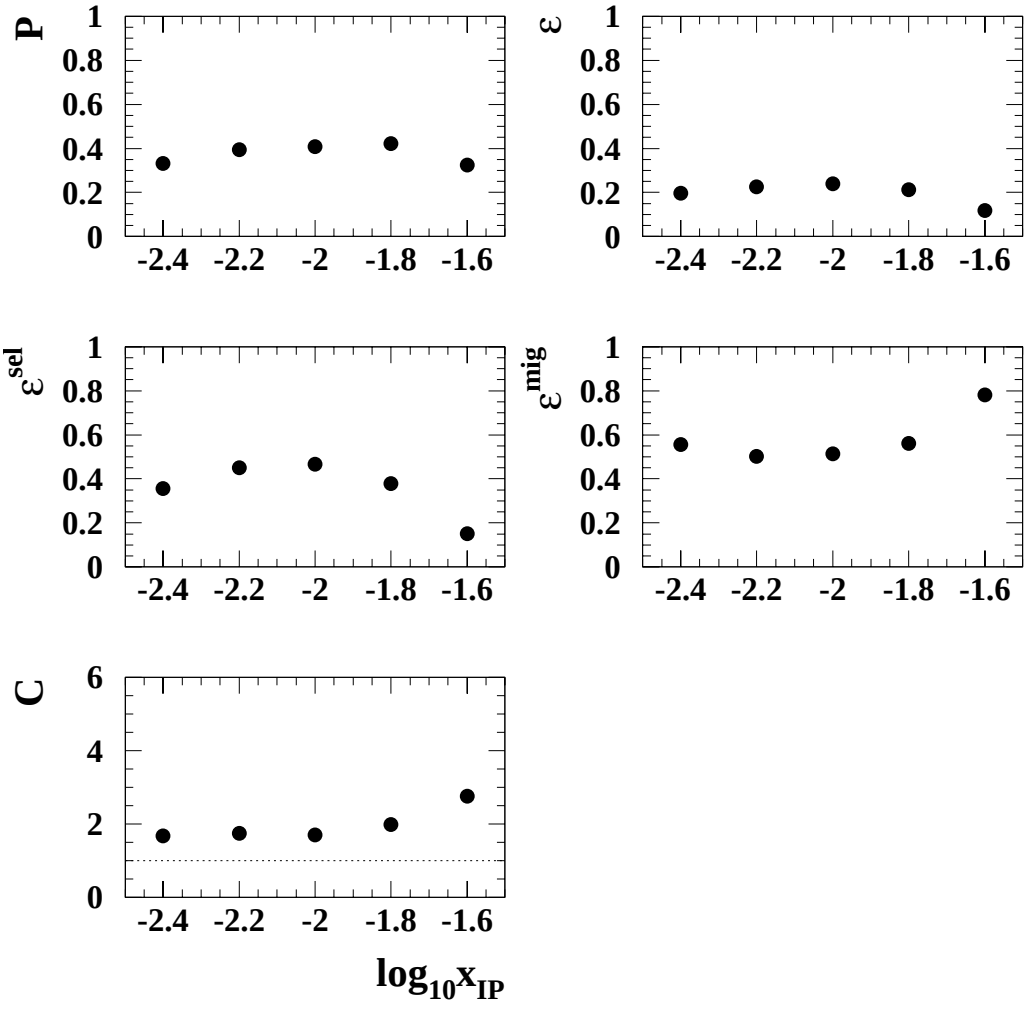

Figure 6.5: The purity $\mathcal{P}$, the efficiency $\mathcal{E}$, the selection efficiency $\mathcal{E}^{\mathrm{sel}}$, the migration efficiency $\mathcal{E}^{\mathrm{mig}}$, and the acceptance correction factor $\mathcal{C}^{\mathrm{acc}}$ of $\log_{10} x_{I\!P}$

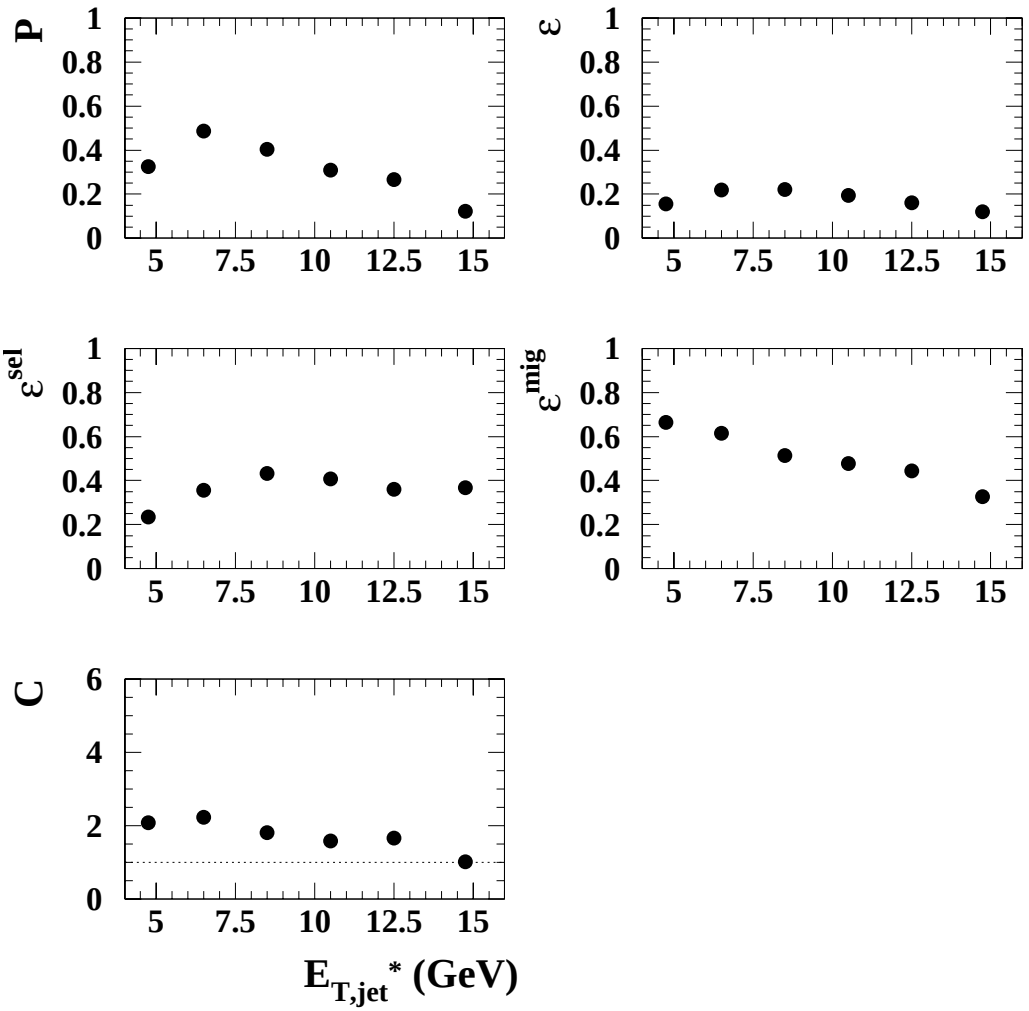

Figure 6.6: The purity $\mathcal{P}$, the efficiency $\mathcal{E}$, the selection efficiency $\mathcal{E}^{\mathrm{sel}}$, the migration efficiency $\mathcal{E}^{\mathrm{mig}}$, and the acceptance correction factor $\mathcal{C}^{\mathrm{acc}}$ of $E^{*}_{T,\mathrm{jets}}$

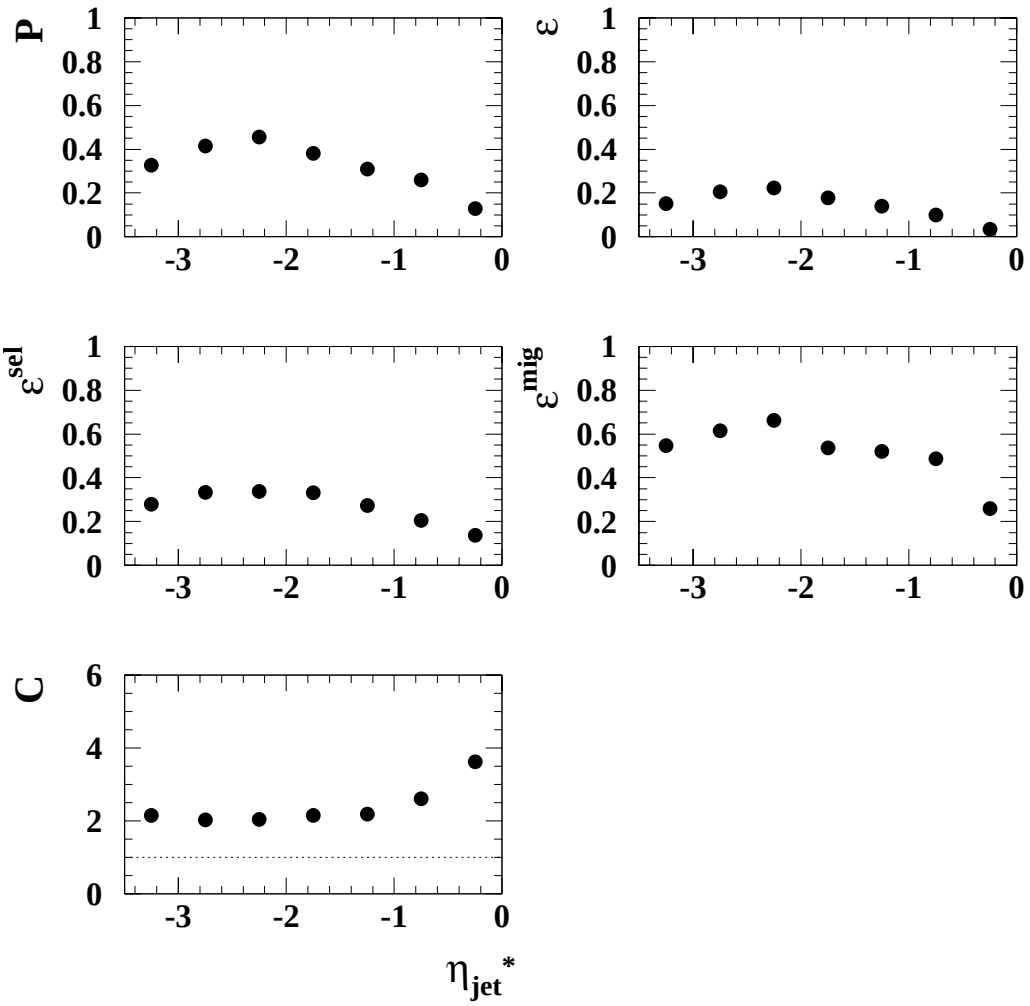

Figure 6.7: The purity $\mathcal{P}$, the efficiency $\mathcal{E}$, the selection efficiency $\mathcal{E}^{\mathrm{sel}}$, the migration efficiency $\mathcal{E}^{\mathrm{mig}}$, and the acceptance correction factor $\mathcal{C}^{\mathrm{acc}}$ of η^{*}_{jets}

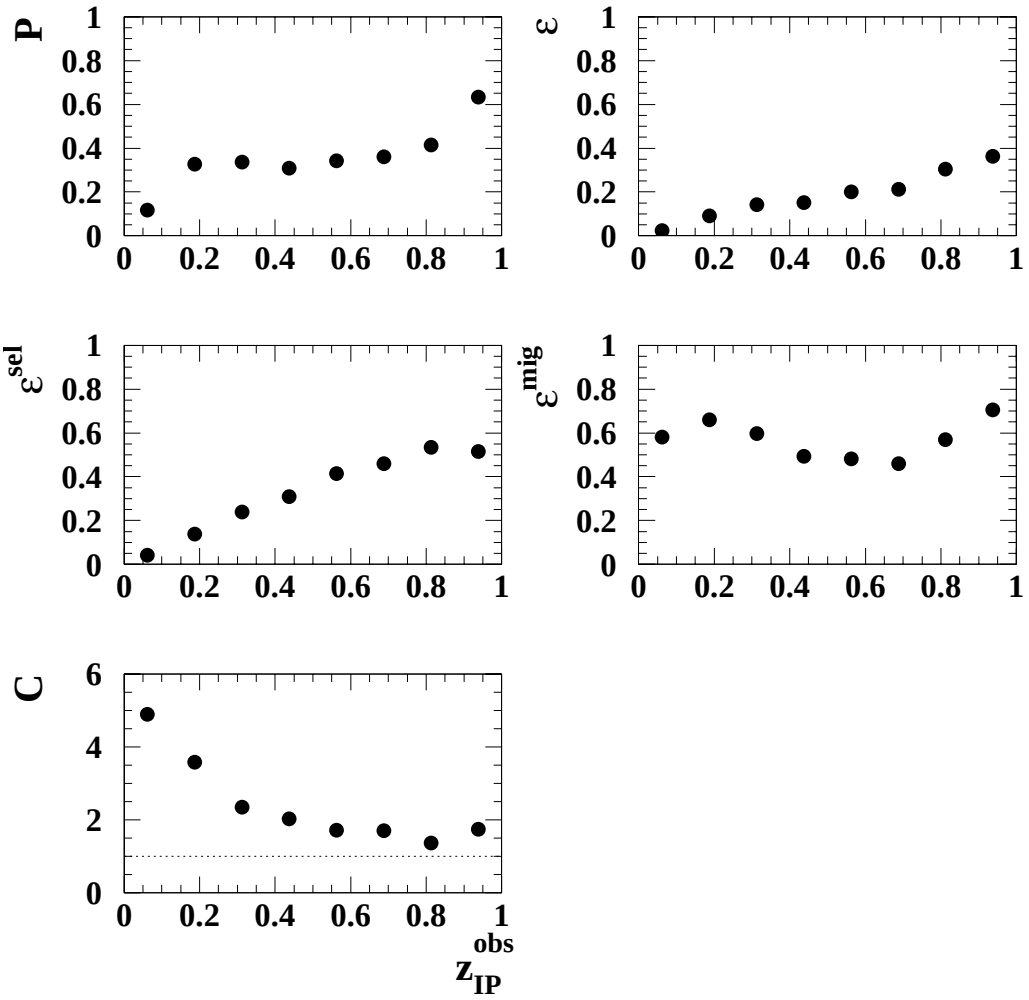

Figure 6.8: The purity $\mathcal{P}$, the efficiency $\mathcal{E}$, the selection efficiency $\mathcal{E}^{\mathrm{sel}}$, the migration efficiency $\mathcal{E}^{\mathrm{mig}}$, and the acceptance correction factor $\mathcal{C}^{\mathrm{acc}}$ of $z_{I\!P}^{\mathrm{obs}}$

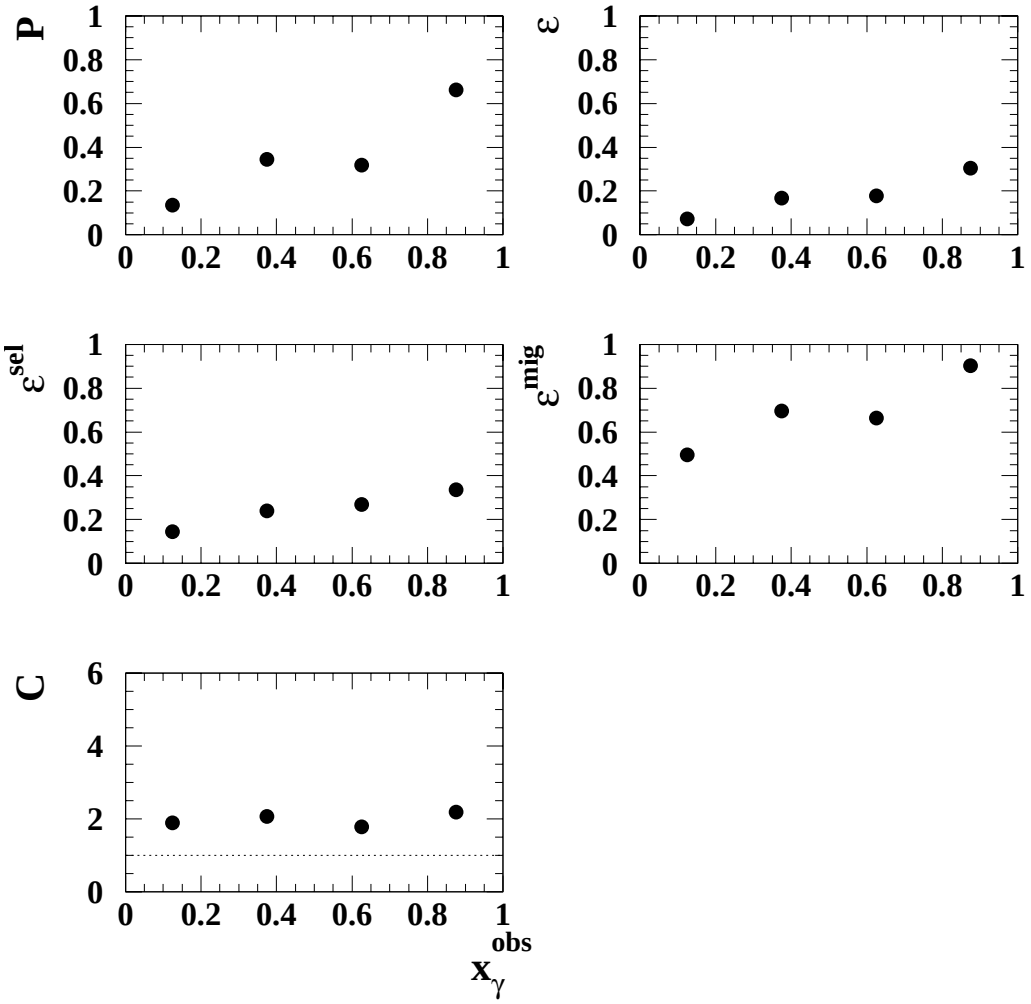

Figure 6.9: The purity $\mathcal{P}$, the efficiency $\mathcal{E}$, the selection efficiency $\mathcal{E}^{\rm sel}$, the migration efficiency $\mathcal{E}^{\rm mig}$, and the acceptance correction factor $\mathcal{C}^{\rm acc}$ of $x_\gamma^{\rm obs}$

6.3 Systematic uncertainties

The systematic uncertainties are estimated by changing the procedure of the measurements of the cross sections. Sources of the systematic uncertainty investigated in this analysis is listed below.

- **Cut on the energy of the scattered electron**
  The cut on the corrected energy of the scattered electron was changed from 10 GeV to 8 GeV.

- $E - p_Z$ **cut**
  The uncertainties related to the rejection of the photoproduction background was estimated by changing the lower cut of $E - p_Z$ from 45 GeV to 43 GeV.

- $\eta^{\mathbf{lab}}_{\mathbf{jets}}$ **cut**
  The cut on $\eta^{\rm lab}_{\rm jets}$ was changed from $-2.0 < \eta^{\rm lab}_{\rm jets} < 2.0$ to $-1.9 < \eta^{\rm lab}_{\rm jets} < 1.9$ or $-2.1 < \eta^{\rm lab}_{\rm jets} < 2.1$.

- $x_{I\!P}$ **cut**
  The cut of $x_{I\!P}$ was changed from 0.03 to 0.025 (0.035).

- $\eta_{\mathbf{max}}$ **cut**
  The cut of $\eta_{\rm max}$ related to the selection of the diffractive events was changed from 2.8 to 2.6 or 3.0.

- **Energy threshold cut of** $\eta_{\mathbf{max}}$
  The energy threshold of EFOs used to calculate $\eta_{\rm max}$, $E_{\rm EFO}$, was changed from 400 MeV to 300 or 500 MeV.

For above changes, the cut parameters are shifted for both data and MC.

- **SRTD alignment**
  The alignment uncertainties of the X and Y position of SRTD is known to be about 2 mm. In order to estimate the effect, the X and Y position of SRTD in the MC was changed by $\pm$3 mm.

- **Uncertainty on the energy measurement of electro-magnetic clusters in the CAL**
  The energy scale of the scattered electron in the MC was changed by $\pm$ 2 % according to the estimated uncertainties.

- **Uncertainty on the energy measurement of hadronic clusters in the CAL**
  The energy scale of the CAL in the MC was changed by $\pm$ 3 % according to the estimated uncertainties.

- **Model dependence between MEPS and CDM**
  The systematic uncertainties of the estimated acceptance correction factor $C^{\rm acc}$ due to the modeling of higher order QCD radiation was estimated by changing the MC from RAPGAP-MEPS to SATRAP-CDM.

For each source of the systematic uncertainties, the cross sections are re-calculated after changing above conditions. Then, the difference (δ_i) between the nominal value of the cross section $\sigma_{\rm nominal}$ and the value of the cross section σ_i for a certain systematic source i is calculated;

$$\delta_i = \sigma_i - \sigma_{\rm nominal} \ . \tag{6.10}$$

The upper error δ_i^+ and the lower error δ_i^- for the systematic source i are set according to the sign of δ_i as;

$$\delta_i^+ = \begin{cases} \delta_i & (\text{if } \delta_i > 0) \\ 0 & (\text{if } \delta_i \leq 0) \end{cases} \ , \tag{6.11}$$

$$\delta_i^- = \begin{cases} 0 & (\text{if } \delta_i \geq 0) \\ \delta_i & (\text{if } \delta_i < 0) \end{cases} \ . \tag{6.12}$$

Each source of the systematic uncertainties for the cross sections is shown on Figure B.1–B.9 in Appendix B. In the figures, the solid lines represent the statistical uncertainties and the points represent the systematic uncertainties. The uncertainties from the hadronic and electron energy scale are larger than other systematic source. The effect of the systematic uncertainties of the model dependence between MEPS and CDM is the second largest among the other systematic uncertainties. The uncertainty of the models and $\eta_{\rm max}$ cut are larger than statistical uncertainties for some kinematical ranges. For most of the cases, systematic uncertainties are smaller than the statistical uncertainties.

The upper value Δ^+ and the lower value Δ^- of the total systematic uncertainties are calculated respectively by added in quadrature;

$$\Delta^+ = \sqrt{\sum_i (\delta_i^+)^2} \ , \tag{6.13}$$

$$\Delta^- = -\sqrt{\sum_i (\delta_i^-)^2} \ . \tag{6.14}$$

These values are used as the total systematic uncertainties except for the electron and hadron energy scale uncertainties, and plotted in the results. The electron and hadron energy scale uncertainties are included in the correlated uncertainties.

6.4 Results

Figure 6.10, 6.11 and 6.12 are the results of the cross sections as functions of Q^2, W, M_X, $\log_{10}\beta$, $\log_{10} x_{I\!P}$, $E^*_{T,\mathrm{jets}}$, η^*_{jets}, $z^{\mathrm{obs}}_{I\!P}$ and $x^{\mathrm{obs}}_{\gamma}$. The values of the cross section are listed in Table 6.2, 6.4, 6.6, 6.8, 6.10, 6.12, 6.14, 6.16, 6.18.

The proton dissociation background was subtracted from the final results. The correlated uncertainties are shown as a shaded band in Figure 6.10, 6.11 and 6.12. The correlated uncertainties include the energy scale uncertainties and the uncertainty of proton dissociation background ($\pm 4\%$). These two sets of uncertainty were added linearly and plotted separately from the other uncertainties. The main sources of the systematic uncertainties are these correlated ones.

The cross sections are compared with the two kind of MC model, SATRAP and RAPGAP. Because such leading-order (LO) predictions are not expected to describe the normalization, both MCs were normalized to data. In Chapter 7, we will discuss the absolute normalization when we compare the results with the NLO predictions. These normalization factors for RAPGAP and SATRAP were 0.92 and 1.12, respectively, so that, the normalization of the LO MC is not so bad in any case. Both LO MCs describe the shape of the data reasonably well. It is surprising that both MC models reproduce the shape of the data according to the different approach where RAPGAP is based on the resolved pomeron model, and SATRAP combines the $q\overline{q}$ and $q\overline{q}g$ states. The cross section as a function of $x^{\mathrm{obs}}_{\gamma}$ is better described by RAPGAP where both direct and resolved photon processes are included. On the other hand, the RAPGAP MC based on only direct photon processes and the SATRAP MC which contains only direct photon processes do not describe the shape of the cross section as a function of $x^{\mathrm{obs}}_{\gamma}$, especially at low $x^{\mathrm{obs}}_{\gamma}$ region, in shown Figure 6.12.

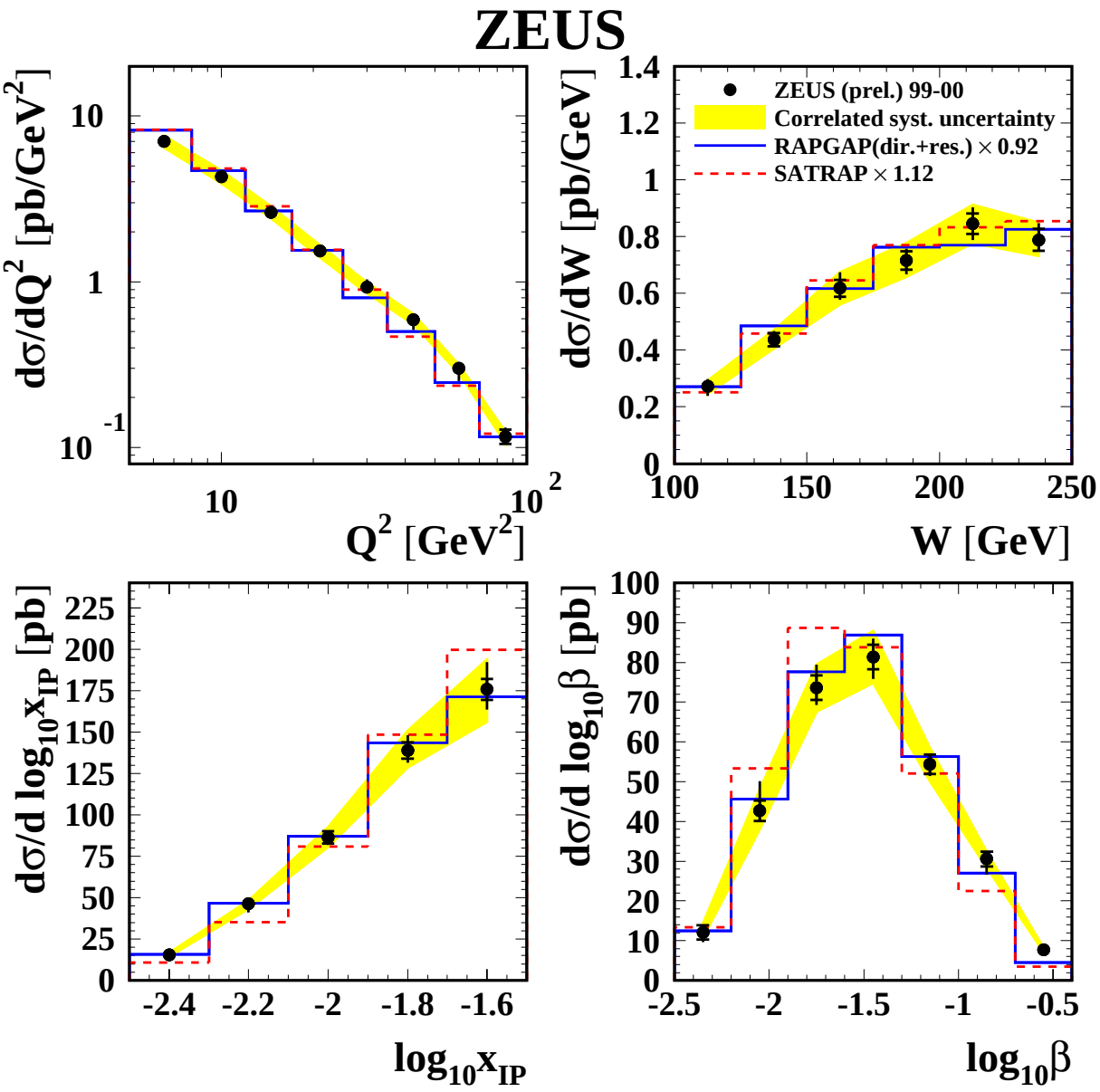

Figure 6.10: The cross sections as a function of Q^2, W, $\log_{10} x_{I\!P}$ and $\log_{10} \beta$. The data are shown as dots; the inner error bars represent the statistical uncertainty while the outer error bars represent the statistical and systematic uncertainties added in quadrature. The shaded band represents the correlated error. The solid lines show the prediction from the LO RAPGAP Monte Carlo normalized by a factor 0.92. SATRAP predictions normalized by a factor 1.12 are shown as dashed lines.

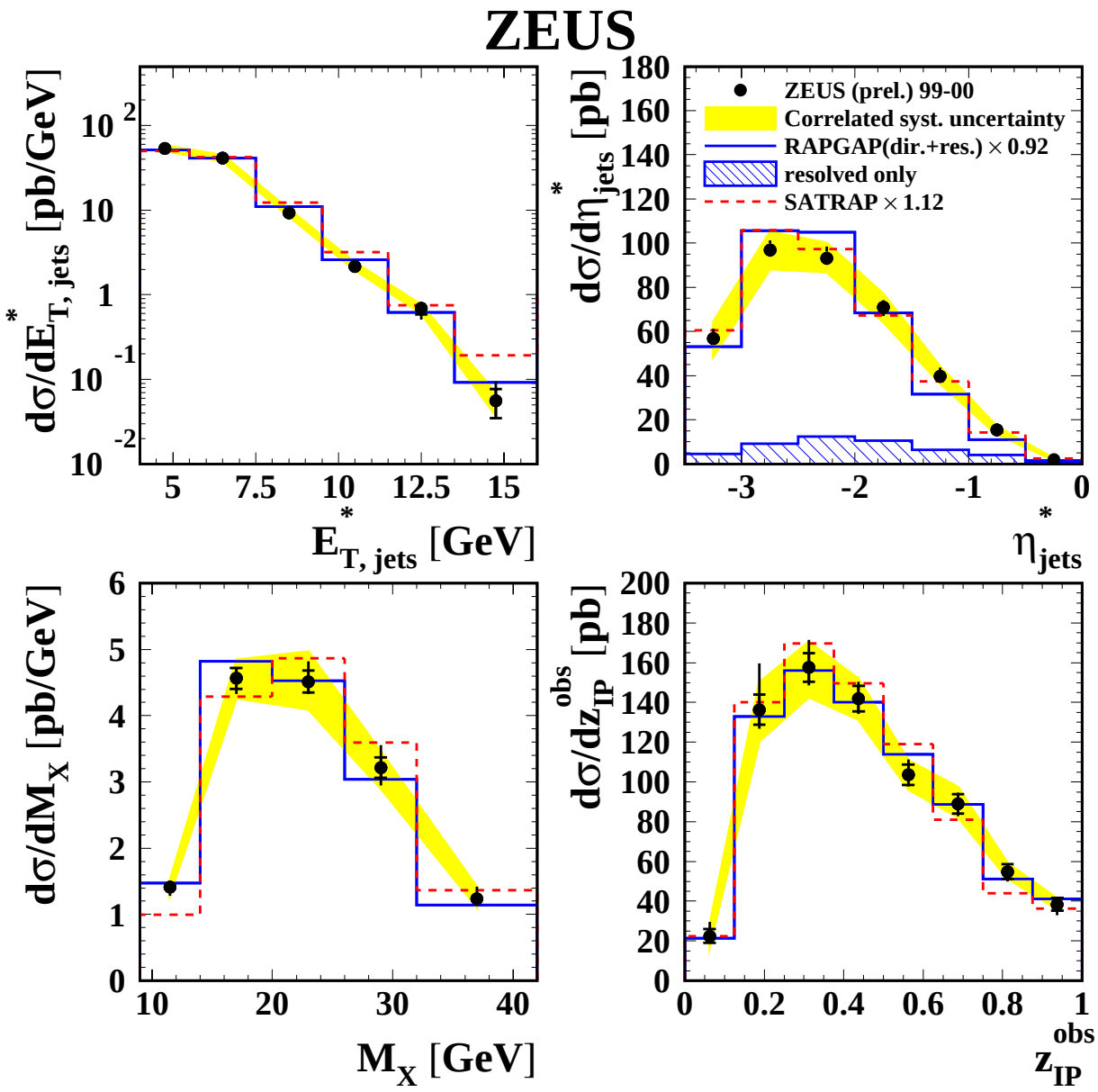

Figure 6.11: The cross sections as a function of $E^*_{T,\text{jets}}$, η^*_{jets}, M_X and $z_{I\!P}^{\text{obs}}$. The data are shown as dots; the inner error bars represent the statistical uncertainty while the outer error bars represent the statistical and systematic uncertainties added in quadrature. The shaded band represents the correlated error. The solid lines show the prediction from the LO RAPGAP Monte Carlo normalized by a factor 0.92. SATRAP predictions normalized by a factor 1.12 are shown as dashed lines. At η^*_{jets} distribution, RAPGAP with resolved photon precess is shown by the hatched area.

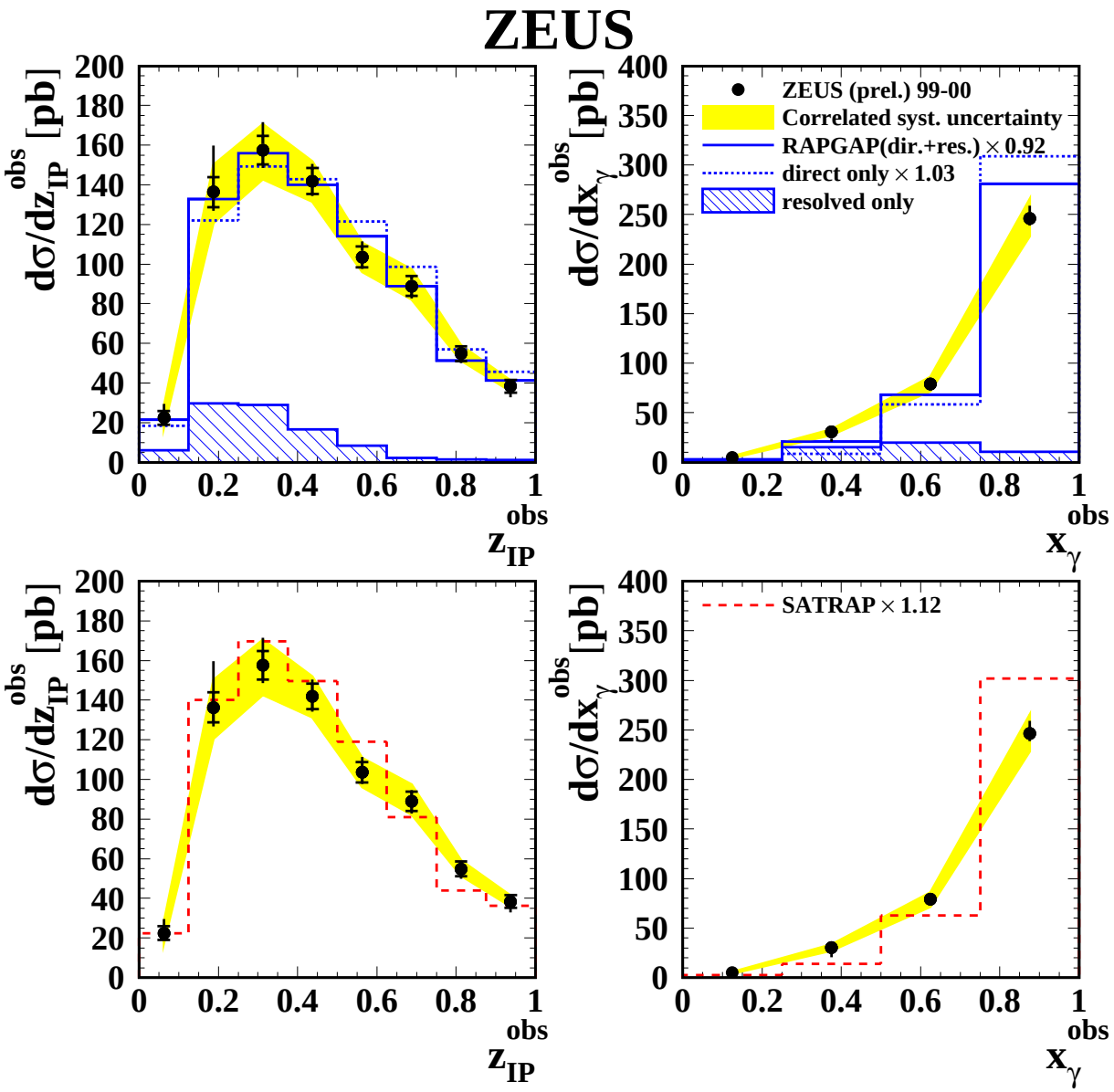

Figure 6.12: The cross sections as a function of $z_{I\!P}^{\rm obs}$ and $x_\gamma^{\rm obs}$. The upper plots show the comparison between data (points) and RAPGAP, both with only direct photon (dashed line) and direct plus resolved contributions (solid line). Direct only cross sections are renormalized by a factor 1.03 and direct plus resolved by a factor 0.92. The resolved component of the latter is also shown by the hatched area in order to emphasize the regions where this kind of processes is more important. The lower plots compare data (points) and the SATRAP predictions renormalized by a factor 1.12; the SATRAP predictions only include direct photon processes.

Q^2[GeV^2]	N_{event}	$\mathcal{E}$	$\mathcal{P}$	$\mathcal{C}^{\text{acc}}$	$\mathcal{C}^{\text{rad}}$
5.0 - 8.0	729	0.199	0.470	2.367	0.945
8.0 - 12.0	739	0.237	0.465	1.962	0.923
12.0 - 17.0	572	0.245	0.477	1.945	0.912
17.0 - 25.0	519	0.251	0.497	1.978	0.929
25.0 - 35.0	402	0.233	0.465	1.998	0.898
35.0 - 50.0	345	0.272	0.602	2.211	0.902
50.0 - 70.0	240	0.270	0.580	2.152	0.904
70.0 - 100.0	165	0.304	0.609	2.004	0.820

Table 6.1: The number of selected event N_{event}, the efficiency $\mathcal{E}$, the purity $\mathcal{P}$, the acceptance correction factor $\mathcal{C}^{\text{acc}}$ and the QED radiative correction factor $\mathcal{C}^{\text{rad}}$ for each bin of $d\sigma/dQ^2$

Q^2[GeV^2]	$\frac{d\sigma}{dQ^2}$ [pb/GeV^2]	stat.	syst.	stat.$\oplus$syst.	Correlated syst.
5.0 - 8.0	7.000	$\pm$0.305	$^{+0.348}_{-0.182}$	$^{+0.463}_{-0.355}$	$^{+0.605}_{-0.559}$
8.0 - 12.0	4.311	$\pm$0.195	$^{+0.297}_{-0.061}$	$^{+0.355}_{-0.204}$	$^{+0.386}_{-0.380}$
12.0 - 17.0	2.615	$\pm$0.137	$^{+0.155}_{-0.065}$	$^{+0.207}_{-0.151}$	$^{+0.235}_{-0.192}$
17.0 - 25.0	1.536	$\pm$0.084	$^{+0.091}_{-0.053}$	$^{+0.124}_{-0.099}$	$^{+0.128}_{-0.136}$
25.0 - 35.0	0.930	$\pm$0.060	$^{+0.088}_{-0.025}$	$^{+0.106}_{-0.065}$	$^{+0.063}_{-0.077}$
35.0 - 50.0	0.591	$\pm$0.040	$^{+0.019}_{-0.069}$	$^{+0.044}_{-0.080}$	$^{+0.046}_{-0.038}$
50.0 - 70.0	0.301	$\pm$0.025	$^{+0.010}_{-0.043}$	$^{+0.027}_{-0.049}$	$^{+0.015}_{-0.021}$
70.0 - 100.0	0.116	$\pm$0.012	$^{+0.011}_{-0.001}$	$^{+0.016}_{-0.012}$	$^{+0.008}_{-0.010}$

Table 6.2: The cross section, the statistical uncertainties, the systematic uncertainties, the statistical and systematic uncertainties added in quadrature and the correlated systematic uncertainties which is the sum of the energy scale and proton dissociation background uncertainties, for each bin of $d\sigma/dQ^2$

W[GeV]	N_{event}	$\mathcal{E}$	$\mathcal{P}$	$\mathcal{C}^{\text{acc}}$	$\mathcal{C}^{\text{rad}}$
100.0 - 125.0	294	0.179	0.350	1.958	0.918
125.0 - 150.0	525	0.175	0.322	1.841	0.877
150.0 - 175.0	705	0.162	0.293	1.804	0.943
175.0 - 200.0	787	0.158	0.304	1.928	0.915
200.0 - 225.0	834	0.150	0.317	2.109	0.932
225.0 - 250.0	566	0.152	0.446	2.941	0.918

Table 6.3: The number of selected event N_{event}, the efficiency $\mathcal{E}$, the purity $\mathcal{P}$, the acceptance correction factor $\mathcal{C}^{\text{acc}}$ and the QED radiative correction factor $\mathcal{C}^{\text{rad}}$ for each bin of $d\sigma/dW$

W[GeV]	$\frac{d\sigma}{dW}$ [pb/GeV]	stat.	syst.	stat.$\oplus$syst.	Correlated syst.
100.0 - 125.0	0.272	$\pm$0.020	$^{+0.015}_{-0.028}$	$^{+0.025}_{-0.034}$	$^{+0.020}_{-0.026}$
125.0 - 150.0	0.437	$\pm$0.024	$^{+0.020}_{-0.004}$	$^{+0.031}_{-0.024}$	$^{+0.034}_{-0.030}$
150.0 - 175.0	0.618	$\pm$0.029	$^{+0.048}_{-0.030}$	$^{+0.056}_{-0.042}$	$^{+0.056}_{-0.057}$
175.0 - 200.0	0.715	$\pm$0.032	$^{+0.027}_{-0.036}$	$^{+0.041}_{-0.048}$	$^{+0.061}_{-0.057}$
200.0 - 225.0	0.845	$\pm$0.037	$^{+0.044}_{-0.043}$	$^{+0.057}_{-0.057}$	$^{+0.067}_{-0.069}$
225.0 - 250.0	0.788	$\pm$0.039	$^{+0.044}_{-0.011}$	$^{+0.058}_{-0.040}$	$^{+0.061}_{-0.057}$

Table 6.4: The cross section, the statistical uncertainties, the systematic uncertainties, the statistical and systematic uncertainties added in quadrature and the correlated systematic uncertainties which is the sum of the energy scale and proton dissociation background uncertainties, for each bin of $d\sigma/dW$

$\log_{10} x_{I\!P}$	N_{event}	$\mathcal{E}$	$\mathcal{P}$	$\mathcal{C}^{\text{acc}}$	$\mathcal{C}^{\text{rad}}$
-2.5 - -2.3	153	0.197	0.331	1.677	0.927
-2.3 - -2.1	428	0.226	0.394	1.740	0.964
-2.1 - -1.9	833	0.240	0.407	1.700	0.947
-1.9 - -1.7	1189	0.212	0.422	1.986	0.913
-1.7 - -1.5	1097	0.118	0.325	2.754	0.903

Table 6.5: The number of selected event N_{event}, the efficiency $\mathcal{E}$, the purity $\mathcal{P}$, the acceptance correction factor $\mathcal{C}^{\text{acc}}$ and the QED radiative correction factor $\mathcal{C}^{\text{rad}}$ for each bin of $d\sigma/d\log_{10} x_{I\!P}$

$\log_{10} x_{I\!P}$	$\frac{d\sigma}{d\log_{10} x_{I\!P}}$ [pb]	stat.	syst.	stat.$\oplus$syst.	Correlated syst.
-2.5 - -2.3	15.323	± 1.583	$^{+0.835}_{-0.107}$	$^{+1.790}_{-1.587}$	$^{+1.345}_{-0.887}$
-2.3 - -2.1	46.270	± 2.828	$^{+0.424}_{-4.480}$	$^{+2.860}_{-5.298}$	$^{+2.021}_{-3.090}$
-2.1 - -1.9	86.423	± 3.817	$^{+0.903}_{-2.854}$	$^{+3.922}_{-4.766}$	$^{+6.247}_{-5.783}$
-1.9 - -1.7	138.832	± 4.998	$^{+7.921}_{-5.609}$	$^{+9.366}_{-7.513}$	$^{+11.896}_{-10.217}$
-1.7 - -1.5	175.717	± 6.317	$^{+15.150}_{-10.470}$	$^{+16.414}_{-12.228}$	$^{+18.176}_{-19.548}$

Table 6.6: The cross section, the statistical uncertainties, the systematic uncertainties, the statistical and systematic uncertainties added in quadrature and the correlated systematic uncertainties which is the sum of the energy scale and proton dissociation background uncertainties, for each bin of $d\sigma/d\log_{10} x_{I\!P}$

$\log_{10}\beta$	N_{event}	$\mathcal{E}$	$\mathcal{P}$	$\mathcal{C}^{\text{acc}}$	$\mathcal{C}^{\text{rad}}$
-2.5 - -2.2	57	0.049	0.267	5.483	0.902
-2.2 - -1.9	367	0.134	0.388	2.902	0.933
-1.9 - -1.6	838	0.205	0.454	2.210	0.927
-1.6 - -1.3	1053	0.267	0.521	1.951	0.922
-1.3 - -1.0	810	0.303	0.525	1.730	0.904
-1.0 - -0.7	453	0.319	0.558	1.752	0.896
-0.7 - -0.4	129	0.308	0.461	1.497	0.924

Table 6.7: The number of selected event N_{event}, the efficiency $\mathcal{E}$, the purity $\mathcal{P}$, the acceptance correction factor $\mathcal{C}^{\text{acc}}$ and the QED radiative correction factor $\mathcal{C}^{\text{rad}}$ for each bin of $d\sigma/d\log_{10}\beta$

$\log_{10}\beta$	$\frac{d\sigma}{d\log_{10}\beta}$ [pb]	stat.	syst.	stat.$\oplus$syst.	Correlated syst.
-2.5 - -2.2	12.103	$\pm$1.755	$^{+0.909}_{-1.678}$	$^{+1.976}_{-2.428}$	$^{+2.269}_{-1.237}$
-2.2 - -1.9	42.678	$\pm$2.588	$^{+6.974}_{-0.627}$	$^{+7.439}_{-2.663}$	$^{+5.404}_{-4.621}$
-1.9 - -1.6	73.697	$\pm$3.086	$^{+4.880}_{-3.194}$	$^{+5.774}_{-4.441}$	$^{+5.767}_{-6.070}$
-1.6 - -1.3	81.374	$\pm$3.099	$^{+3.510}_{-4.582}$	$^{+4.682}_{-5.532}$	$^{+6.540}_{-6.615}$
-1.3 - -1.0	54.416	$\pm$2.438	$^{+1.052}_{-1.756}$	$^{+2.655}_{-3.004}$	$^{+4.094}_{-4.236}$
-1.0 - -0.7	30.552	$\pm$1.889	$^{+0.597}_{-3.499}$	$^{+1.981}_{-3.976}$	$^{+1.812}_{-2.144}$
-0.7 - -0.4	7.666	$\pm$1.014	$^{+0.220}_{-0.337}$	$^{+1.038}_{-1.069}$	$^{+0.461}_{-0.581}$

Table 6.8: The cross section, the statistical uncertainties, the systematic uncertainties, the statistical and systematic uncertainties added in quadrature and the correlated systematic uncertainties which is the sum of the energy scale and proton dissociation background uncertainties, for each bin of $d\sigma/d\log_{10}\beta$

M_X[GeV]	N_{event}	$\mathcal{E}$	$\mathcal{P}$	$\mathcal{C}^{\text{acc}}$	$\mathcal{C}^{\text{rad}}$
9.0 - 14.0	384	0.258	0.392	1.521	0.936
14.0 - 20.0	1341	0.321	0.550	1.713	0.926
20.0 - 26.0	1131	0.244	0.489	2.001	0.929
26.0 - 32.0	596	0.162	0.445	2.746	0.916
32.0 - 42.0	251	0.086	0.371	4.319	0.884

Table 6.9: The number of selected event N_{event}, the efficiency $\mathcal{E}$, the purity $\mathcal{P}$, the acceptance correction factor $\mathcal{C}^{\text{acc}}$ and the QED radiative correction factor $\mathcal{C}^{\text{rad}}$ for each bin of $d\sigma/dM_X$

M_X[GeV]	$\frac{d\sigma}{dM_X}$ [pb/GeV]	stat.	syst.	stat.$\oplus$syst.	Correlated syst.
9.0 - 14.0	1.408	$\pm$0.093	$^{+0.027}_{-0.090}$	$^{+0.097}_{-0.129}$	$^{+0.113}_{-0.101}$
14.0 - 20.0	4.564	$\pm$0.158	$^{+0.070}_{-0.175}$	$^{+0.173}_{-0.235}$	$^{+0.276}_{-0.298}$
20.0 - 26.0	4.514	$\pm$0.167	$^{+0.254}_{-0.090}$	$^{+0.304}_{-0.189}$	$^{+0.455}_{-0.421}$
26.0 - 32.0	3.217	$\pm$0.157	$^{+0.298}_{-0.216}$	$^{+0.337}_{-0.267}$	$^{+0.241}_{-0.319}$
32.0 - 42.0	1.234	$\pm$0.088	$^{+0.160}_{-0.066}$	$^{+0.183}_{-0.110}$	$^{+0.180}_{-0.119}$

Table 6.10: The cross section, the statistical uncertainties, the systematic uncertainties, the statistical and systematic uncertainties added in quadrature and the correlated systematic uncertainties which is the sum of the energy scale and proton dissociation background uncertainties, for each bin of $d\sigma/dM_X$

$E^*_{T,\mathrm{jets}}$[GeV]	N_{event}	$\mathcal{E}$	$\mathcal{P}$	$\mathcal{C}^{\mathrm{acc}}$	$\mathcal{C}^{\mathrm{rad}}$
4.0 - 5.5	3328	0.156	0.325	2.078	0.910
5.5 - 7.5	3129	0.218	0.486	2.227	0.922
7.5 - 9.5	864	0.222	0.403	1.816	0.919
9.5 - 11.5	221	0.195	0.308	1.583	0.965
11.5 - 13.5	64	0.160	0.266	1.661	1.013
13.5 - 16.0	12	0.119	0.122	1.019	0.886

Table 6.11: The number of selected event N_{event}, the efficiency $\mathcal{E}$, the purity $\mathcal{P}$, the acceptance correction factor $\mathcal{C}^{\mathrm{acc}}$ and the QED radiative correction factor $\mathcal{C}^{\mathrm{rad}}$ for each bin of $d\sigma/dE^*_{T,\mathrm{jets}}$

$E^*_{T,\mathrm{jets}}$[GeV]	$\frac{d\sigma}{dE^*_{T,\mathrm{jets}}}$ [pb/GeV]	stat.	syst.	stat.$\oplus$syst.	Correlated syst.
4.0 - 5.5	54.066	$\pm$1.173	$^{+2.494}_{-1.488}$	$^{+2.756}_{-1.895}$	$^{+4.013}_{-3.906}$
5.5 - 7.5	41.391	$\pm$0.904	$^{+1.490}_{-1.160}$	$^{+1.743}_{-1.471}$	$^{+3.395}_{-3.397}$
7.5 - 9.5	9.288	$\pm$0.389	$^{+0.696}_{-0.238}$	$^{+0.797}_{-0.456}$	$^{+0.913}_{-0.852}$
9.5 - 11.5	2.173	$\pm$0.183	$^{+0.186}_{-0.059}$	$^{+0.261}_{-0.192}$	$^{+0.231}_{-0.210}$
11.5 - 13.5	0.694	$\pm$0.112	$^{+0.058}_{-0.148}$	$^{+0.126}_{-0.186}$	$^{+0.067}_{-0.095}$
13.5 - 16.0	0.056	$\pm$0.021	$^{+0.032}_{-0.004}$	$^{+0.038}_{-0.021}$	$^{+0.013}_{-0.018}$

Table 6.12: The cross section, the statistical uncertainties, the systematic uncertainties, the statistical and systematic uncertainties added in quadrature and the correlated systematic uncertainties which is the sum of the energy scale and proton dissociation background uncertainties, for each bin of $d\sigma/dE^*_{T,\mathrm{jets}}$

$\eta^*_{\rm jets}$	$N_{\rm event}$	$\mathcal{E}$	$\mathcal{P}$	$\mathcal{C}^{\rm acc}$	$\mathcal{C}^{\rm rad}$
-3.5 - -3.0	999	0.153	0.328	2.148	1.026
-3.0 - -2.5	1986	0.205	0.415	2.026	0.935
-2.5 - -2.0	1975	0.223	0.456	2.045	0.896
-2.0 - -1.5	1416	0.178	0.382	2.146	0.906
-1.5 - -1.0	832	0.141	0.309	2.190	0.846
-1.0 - -0.5	300	0.100	0.261	2.614	0.761
-0.5 - 0.0	37	0.035	0.128	3.621	0.578

Table 6.13: The number of selected event $N_{\rm event}$, the efficiency $\mathcal{E}$, the purity $\mathcal{P}$, the acceptance correction factor $\mathcal{C}^{\rm acc}$ and the QED radiative correction factor $\mathcal{C}^{\rm rad}$ for each bin of $d\sigma/d\eta^*_{\rm jets}$

$\eta^*_{\rm jets}$	$\frac{d\sigma}{d\eta^*_{\rm jets}}$ [pb]	stat.	syst.	stat.$\oplus$syst.	Correlated syst.
-3.5 - -3.0	56.728	$\pm$2.191	$^{+3.826}_{-1.099}$	$^{+4.409}_{-2.451}$	$^{+7.724}_{-8.005}$
-3.0 - -2.5	96.944	$\pm$2.656	$^{+3.353}_{-1.745}$	$^{+4.277}_{-3.178}$	$^{+8.225}_{-8.771}$
-2.5 - -2.0	93.223	$\pm$2.562	$^{+4.562}_{-1.708}$	$^{+5.232}_{-3.079}$	$^{+6.864}_{-6.280}$
-2.0 - -1.5	70.918	$\pm$2.339	$^{+2.282}_{-3.270}$	$^{+3.267}_{-4.020}$	$^{+6.065}_{-6.660}$
-1.5 - -1.0	39.694	$\pm$1.787	$^{+3.395}_{-2.347}$	$^{+3.837}_{-2.950}$	$^{+4.418}_{-3.187}$
-1.0 - -0.5	15.382	$\pm$1.161	$^{+1.188}_{-1.929}$	$^{+1.661}_{-2.251}$	$^{+1.557}_{-1.943}$
-0.5 - 0.0	1.994	$\pm$0.417	$^{+0.808}_{-0.532}$	$^{+0.909}_{-0.676}$	$^{+0.462}_{-0.166}$

Table 6.14: The cross section, the statistical uncertainties, the systematic uncertainties, the statistical and systematic uncertainties added in quadrature and the correlated systematic uncertainties which is the sum of the energy scale and proton dissociation background uncertainties, for each bin of $d\sigma/d\eta^*_{\rm jets}$

$z_{I\!P}^{\rm obs}$	$N_{\rm event}$	$\mathcal{E}$	$\mathcal{P}$	$\mathcal{C}^{\rm acc}$	$\mathcal{C}^{\rm rad}$
0.000 - 0.125	53	0.024	0.117	4.883	0.840
0.125 - 0.250	424	0.092	0.328	3.580	0.872
0.250 - 0.375	711	0.143	0.336	2.355	0.913
0.375 - 0.500	728	0.152	0.309	2.028	0.933
0.500 - 0.625	619	0.200	0.343	1.714	0.948
0.625 - 0.750	538	0.211	0.361	1.706	0.941
0.750 - 0.875	409	0.304	0.414	1.363	0.955
0.875 - 1.000	229	0.364	0.632	1.737	0.936

Table 6.15: The number of selected event $N_{\rm event}$, the efficiency $\mathcal{E}$, the purity $\mathcal{P}$, the acceptance correction factor $\mathcal{C}^{\rm acc}$ and the QED radiative correction factor $\mathcal{C}^{\rm rad}$ for each bin of $d\sigma/dz_{I\!P}^{\rm obs}$

$z_{I\!P}^{\rm obs}$	$\frac{d\sigma}{dz_{I\!P}^{\rm obs}}$ [pb]	stat.	syst.	stat.$\oplus$syst.	Correlated syst.
0.000 - 0.125	22.407	$\pm$3.452	$^{+6.235}_{-0.501}$	$^{+7.127}_{-3.489}$	$^{+5.951}_{-4.530}$
0.125 - 0.250	136.330	$\pm$7.645	$^{+22.098}_{-5.754}$	$^{+23.383}_{-9.568}$	$^{+13.795}_{-15.622}$
0.250 - 0.375	157.545	$\pm$7.177	$^{+12.043}_{-5.482}$	$^{+14.019}_{-9.031}$	$^{+12.940}_{-14.828}$
0.375 - 0.500	141.901	$\pm$6.532	$^{+5.458}_{-3.827}$	$^{+8.513}_{-7.571}$	$^{+9.976}_{-10.511}$
0.500 - 0.625	103.611	$\pm$5.213	$^{+5.723}_{-3.004}$	$^{+7.741}_{-6.016}$	$^{+7.126}_{-7.497}$
0.625 - 0.750	88.963	$\pm$4.900	$^{+2.671}_{-3.893}$	$^{+5.580}_{-6.258}$	$^{+8.441}_{-6.801}$
0.750 - 0.875	54.848	$\pm$3.671	$^{+0.862}_{-3.198}$	$^{+3.771}_{-4.869}$	$^{+4.223}_{-3.497}$
0.875 - 1.000	38.388	$\pm$3.189	$^{+0.629}_{-4.474}$	$^{+3.250}_{-5.494}$	$^{+2.933}_{-2.478}$

Table 6.16: The cross section, the statistical uncertainties, the systematic uncertainties, the statistical and systematic uncertainties added in quadrature and the correlated systematic uncertainties which is the sum of the energy scale and proton dissociation background uncertainties, for each bin of $d\sigma/dz_{I\!P}^{\rm obs}$

$x_\gamma^{\rm obs}$	$N_{\rm event}$	$\mathcal{E}$	$\mathcal{P}$	$\mathcal{C}^{\rm acc}$	$\mathcal{C}^{\rm rad}$
0.00 - 0.25	62	0.072	0.136	1.894	0.824
0.25 - 0.50	359	0.167	0.345	2.067	0.797
0.50 - 0.75	922	0.178	0.319	1.790	0.930
0.75 - 1.00	2368	0.303	0.662	2.183	0.924

Table 6.17: The number of selected event $N_{\rm event}$, the efficiency $\mathcal{E}$, the purity $\mathcal{P}$, the acceptance correction factor $\mathcal{C}^{\rm acc}$ and the QED radiative correction factor $\mathcal{C}^{\rm rad}$ for each bin of $d\sigma/dx_\gamma^{\rm obs}$

$x_\gamma^{\rm obs}$	$\frac{d\sigma}{dx_\gamma^{\rm obs}}$ [pb]	stat.	syst.	stat.$\oplus$syst.	Correlated syst.
0.00 - 0.25	4.987	$\pm$0.937	$^{+0.262}_{-1.077}$	$^{+0.973}_{-1.427}$	$^{+0.958}_{-0.670}$
0.25 - 0.50	30.491	$\pm$2.221	$^{+3.918}_{-9.385}$	$^{+4.504}_{-9.644}$	$^{+2.744}_{-3.030}$
0.50 - 0.75	79.067	$\pm$3.401	$^{+3.801}_{-4.338}$	$^{+5.100}_{-5.512}$	$^{+6.956}_{-7.528}$
0.75 - 1.00	246.215	$\pm$6.070	$^{+11.252}_{-4.317}$	$^{+12.785}_{-7.449}$	$^{+19.165}_{-17.932}$

Table 6.18: The cross section, the statistical uncertainties, the systematic uncertainties, the statistical and systematic uncertainties added in quadrature and the correlated systematic uncertainties which is the sum of the energy scale and proton dissociation background uncertainties, for each bin of $d\sigma/dx_\gamma^{\rm obs}$

Chapter 7

Comparison to NLO QCD calculation

As described in Chapter 6, the cross sections are measured as functions of Q^2, W, $\log_{10} x_{I\!P}$, $\log_{10} \beta$, M_X, $E^*_{T,\mathrm{jets}}$, η^*_{jets}, $z_{I\!P}^{\mathrm{obs}}$ and x_γ^{obs}. In this chapter, the measured cross sections are compared to predictions of perturbative QCD calculation at the next-to-leading order (NLO) in the strong-coupling constant α_s.

7.1 NLO QCD calculation

The DISENT program [54] is used in order to obtain the cross sections predicted by the NLO QCD ($\mathcal{O}(\alpha_s^2)$) calculations. The program is originally for non-diffractive DIS events. This program was adapted to diffractive processes specially for a comparison purpose in this analysis. The following procedure was used for the adaptation.

1. The cross sections at a given fixed value of $x_{I\!P}$ and $t = 0$ is calculated by changing the proton beam energy by a factor $x_{I\!P}$, i.e. $E_{x_{I\!P}} = x_{I\!P} E_p$ (see Figure 7.1).

2. The proton PDF is replaced with the pomeron PDF.

3. The calculated cross sections are multiplied by the t-integrated pomeron flux factor shown in Eq.(2.19), i.e.;

$$f_{I\!P/p}(x_{I\!P}) = \int_{t_{cut}}^{t_{min}} f_{I\!P/p}(x_{I\!P}, t) dt \ , \tag{7.1}$$

   where t_{min} is the minimum kinematically allowed value of $|t|$, and t_{cut} is the limit of the measurement and is chosen to -10 GeV^2.

4. The cross sections at given $x_{I\!P}$ values are summed over with a measured interval in $x_{I\!P}$ by the following formula;

$$\frac{d\sigma}{dX} = \sum_i \left(\frac{d\sigma(x_{I\!P} = a_i)}{dX} \cdot \Delta(x_{I\!P})_i \right) , \tag{7.2}$$

where X is the measured variable, a_i is the fixed value of $x_{I\!P}$ in the bin i, and $\Delta(x_{I\!P})_i$ is the width of $x_{I\!P}$ in the bin i. In this analysis, the $x_{I\!P}$ range was divided into 100 bins.

The NLO calculations is performed in the $\overline{\text{MS}}$ renormalisation and factorisation schemes using a generalized version [54] of the subtraction method [55]. The number of quark flavours is set to four. The renormalisation scale (μ_R) is chosen to be $\mu_R = E^*_{T,\text{jet1}}$, and the factorisation scale (μ_F) is chosen to be $\mu_F = 6.8$ GeV corresponding to the average of the highest $E^*_{T,\text{jet}}$ in the data. The $\alpha_s(M_Z)$ was set to the value used in the extraction of the diffractive PDFs in the DGLAP QCD fit to keep a consistency. The values were described in Section 2.7. The calculation of running α_s was performed with the QCDNUM program with version 16.13 [56]. The jets are reconstructed from the partons in the events generated by DISENT program to calculate the NLO prediction of the dijets cross section. Inclusive k_T algorithm, described in Section 5.7.2, was applied. To estimate the effect of the higher order terms beyond the NLO, μ_R is varied between $E^*_{T,\text{jet1}}/2$ and $2E^*_{T,\text{jet1}}$. This was quoted as a scale uncertainty, while μ_F is unchanged.

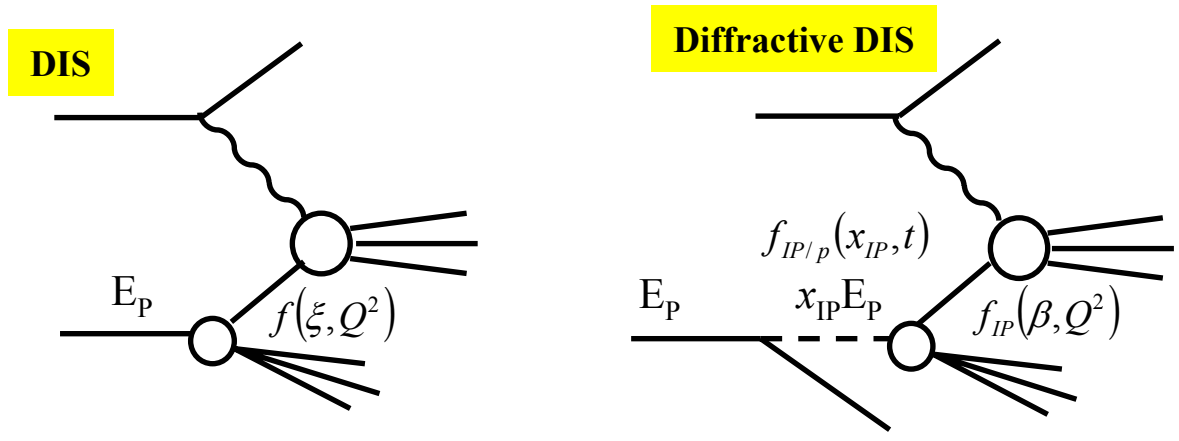

Figure 7.1: Diagram of DIS and diffractive DIS processes in DISENT NLO program.

7.2 Hadronization correction

Since the cross sections calculated by DISENT are at the parton level, they need to be converted to the cross sections at hadron level before the comparison to the measurements. A hadronization correction factor $\mathcal{C}^{\rm had}$ for each measured bin is determined with RAPGAP MC samples as the following as;

$$\mathcal{C}^{\rm had} = \frac{\sigma^{\rm had}}{\sigma^{\rm par}} \ , \tag{7.3}$$

where $\sigma^{\rm had}$ is the hadron level cross section and $\sigma^{\rm par}$ is the parton level cross section calculated after the parton shower. RAPGAP MC samples was used with both direct and resolved photon process included. Figure 7.2 shows the hadronization correction factors as functions of Q^2, W, $\log_{10} x_{I\!P}$, $E^*_{T,\rm jets}$, $\eta^*_{\rm jets}$, $z^{\rm obs}_{I\!P}$ and $x^{\rm obs}_\gamma$ using the RAPGAP MC with direct and resolved photon processes.

The hadronization correction factors are mostly constant with kinematic variables. $\eta^*_{\rm jets}$ and $z^{\rm obs}_{I\!P}$ have some dependence. $\mathcal{C}^{\rm had}$ of $x^{\rm obs}_\gamma$ shows fluctuation since the parton level in $x^{\rm obs}_\gamma$ has almost the peak at 1, hence the migration from the parton to the hadron level moves the events in a particular direction.

7.3 Comparison with NLO calculation with diffractive PDFs

The measured cross sections, shown in Section 6.4, are compared with the NLO QCD predictions in Figure 7.3 and 7.4 by using the ZEUS-LPS diffractive PDFs which is described in Section 2.7. These plots are the cross sections as functions of Q^2, W, $\log_{10}\beta$, M_X, $\log_{10} x_{I\!P}$, $E^*_{T,\rm jets}$, $\eta^*_{T,\rm jets}$, $z^{\rm obs}_{I\!P}$ and $x^{\rm obs}_\gamma$. The dash lines are the NLO prediction at the parton level, and the solid lines are the NLO prediction after the hadronization correction. The hatched area represents the scale uncertainty. The renormalisation scale μ_R was changed by a factor from 1/2 or 2, the scale uncertainties are typically $\sim$ 20–30%. The uncertainty from the diffractive PDFs are not included. The effects of the hadronization correction seems to be small in all kinematic variables.

A more detailed comparison between the data and the NLO predictions with ZEUS-LPS fit can be seen in Figure 7.5, 7.6 and 7.7. These plots are the ratios of data to the ZEUS-LPS NLO predictions.

The NLO prediction with ZEUS-LPS diffractive PDFs describes data fairly well considering the scale uncertainty. Slight deviations in this comparison are observed, which are discussed below.

$d\sigma/dz^{\rm obs}_{I\!P}$ is the important cross section since it directly reflects the diffractive PDFs. The data is reasonably in agreement with the NLO prediction. At highest bin of $z^{\rm obs}_{I\!P}$, the

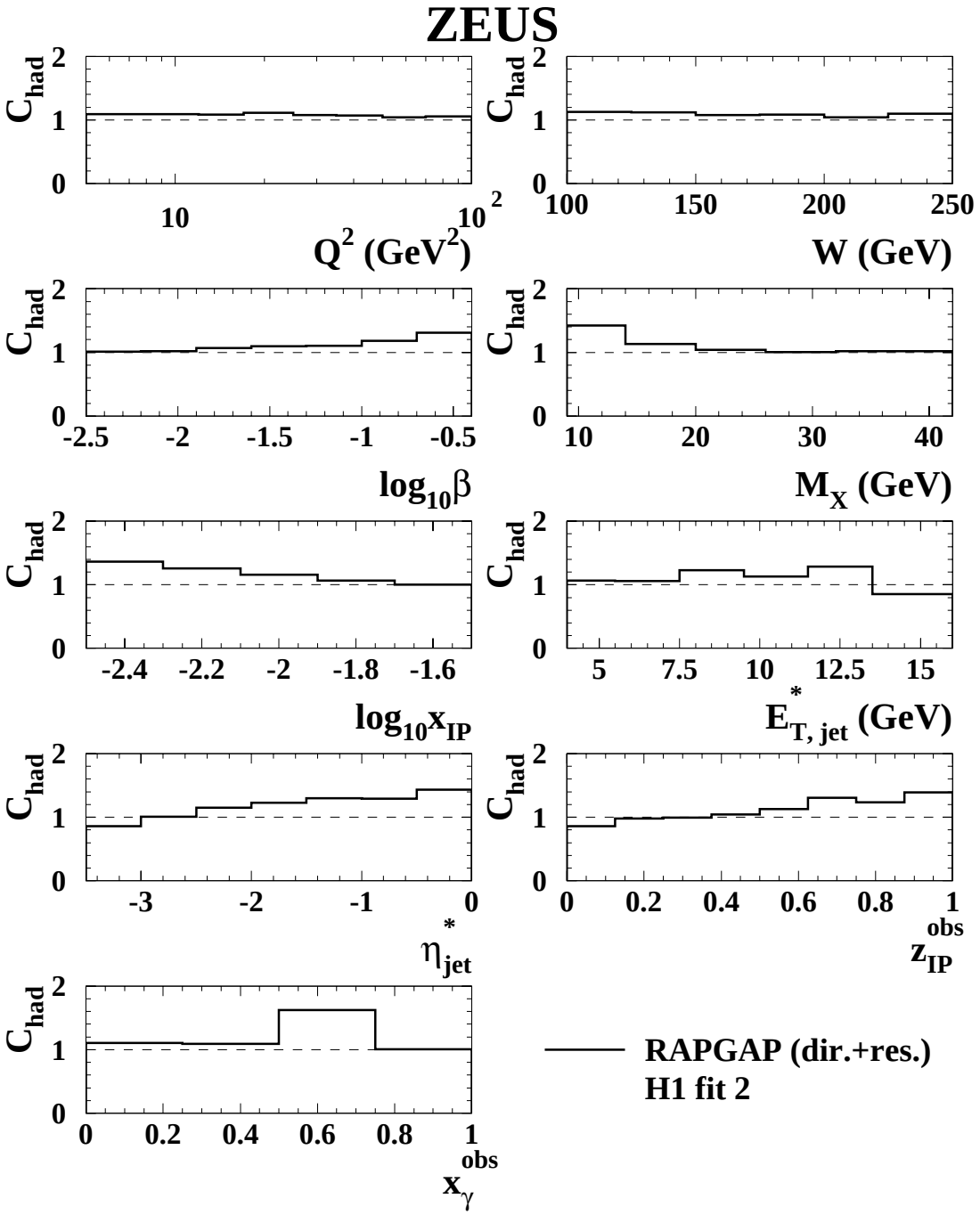

Figure 7.2: The hadronization correction factor $\mathcal{C}^{\rm had}$ as function of Q^2, W, $\log_{10} x_{I\!P}$, $E^*_{T,\rm jets}$, $\eta^*_{\rm jets}$, $z^{\rm obs}_{I\!P}$ and $x^{\rm obs}_\gamma$.

NLO prediction is slightly smaller than data, but still within the scale uncertainty.

$x_{I\!P}$ distribution is well reproduced with the prediction. The NLO prediction has a trend to be higher at high Q^2 and β.

The largest difference is found in $x_\gamma^{\rm obs}$ distribution. The ZEUS-LPS NLO predictions underestimates the data at low $x_\gamma^{\rm obs}$ region. Considering Figure 6.12 that low $x_\gamma^{\rm obs}$ region is dominated by the resolved photon contribution in the LO Monte Carlo model, this might be due to the fact that this NLO prediction does not include resolved photon contribution explicitly. The $\eta^*_{\rm jet}$ distribution of the NLO prediction is shifted to the backward direction. This can be also improved if the resolve photon component is included (see Figure 6.11 for LO MC case.)

In Figure 7.8 and 7.9, data are compared with NLO predictions with the three different diffractive PDFs shown in Section 2.7. To compare in more detail, Figure 7.10, 7.11 and 7.12 shows the ratios of data to the ZEUS-LPS NLO predictions.

For all kinematic variables, the overall absolute normalization of the NLO prediction with H1 2002 fit is slightly larger than the NLO prediction with ZEUS-LPS fit. This is expected since the PDF gives the higher gluon density at large z. The NLO prediction based on ZEUS-LPS fit is the closest to the data than H1 2002 fit. On the other hand, the NLO predictions with GLP fit underestimate the data. They are typically about half of the NLO prediction of ZEUS-LPS fit.

One of the reasons why the ZEUS-LPS fit is better is that the PDF is made including the experimental data on the charm production. Since the heavy quark is copiously produced with the boson gluon processes, the data also has a good sensitivity to the gluon distribution. The good agreement with the ZEUS LPS data implies that the dijet result and charm result give a consistent result.

Dijet cross section in diffractive DIS obtained in this analysis clearly demonstrates that the significant gluon contents in the pomeron at high z. The data can give a constraint to the diffractive PDFs. In future, better diffractive PDFs can be obtained using this data to the DGLAP QCD fit.

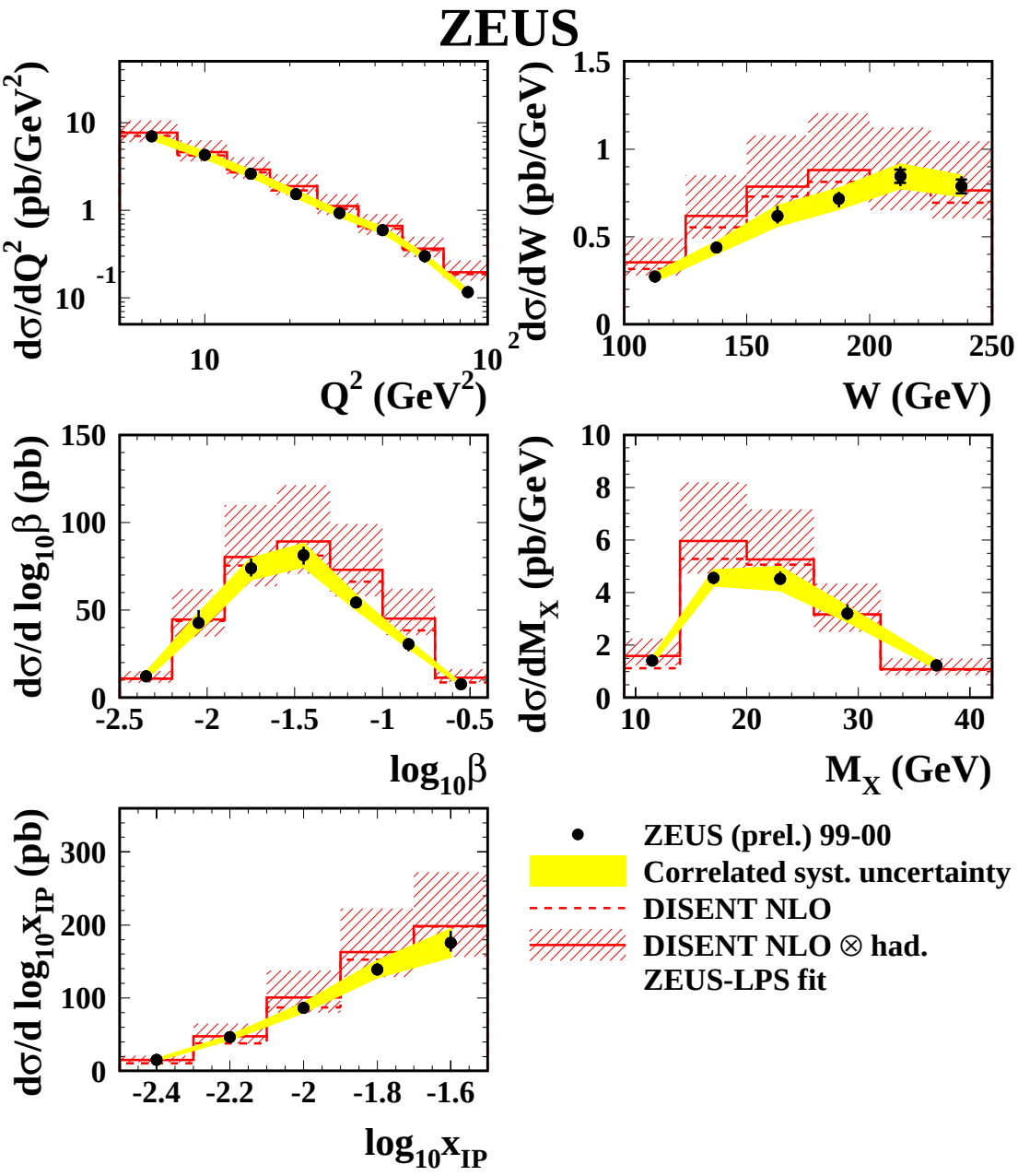

Figure 7.3: The cross sections in Q^2, W, $\log_{10}\beta$, M_X and $\log_{10} x_{I\!P}$ compared to the NLO QCD prediction from ZEUS-LPS fit. The data are shown as dots; the inner error bars represent the statistical uncertainty while the outer error bars represent the statistical and systematic uncertainties added in quadrature. The shaded band represents the correlated error. The solid lines represent the NLO cross sections from the ZEUS-LPS fit; dashed lines show the same NLO predictions before hadronization corrections. Uncertainty on these calculation due to the renormalisation scale choice is shown as a hatched area around the NLO predictions corrected for the hadronization effects.

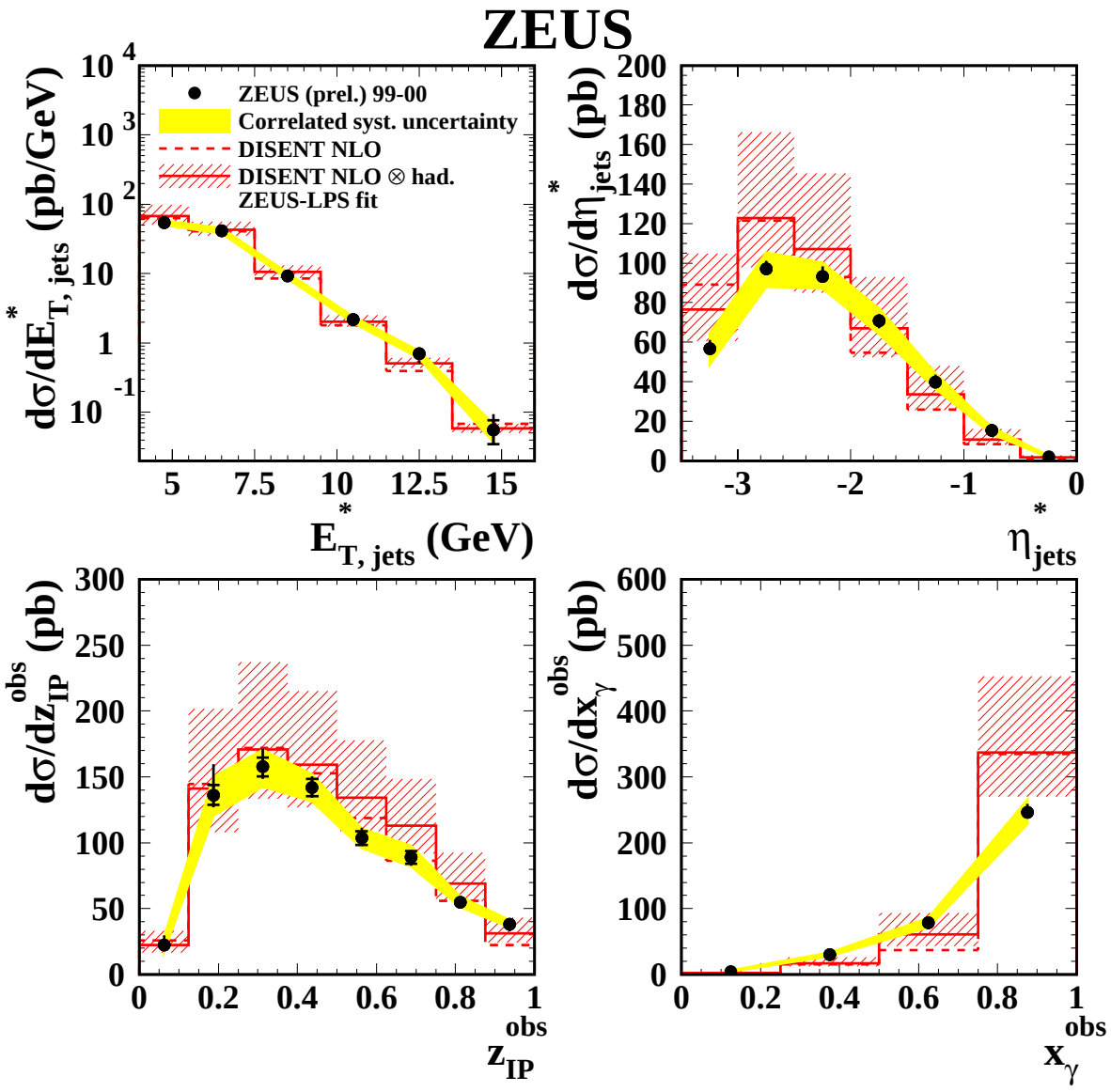

Figure 7.4: The cross sections in $E^*_{T,\text{jets}}$, η^*_{jets}, $z_{I\!P}^{\text{obs}}$ and x_γ^{obs} compared to the NLO QCD prediction from ZEUS-LPS fit. The data are shown as dots; the inner error bars represent the statistical uncertainty while the outer error bars represent the statistical and systematic uncertainties added in quadrature. The shaded band represents the correlated error. The solid lines represent the NLO cross sections from the ZEUS-LPS fit; dashed lines show the same NLO predictions before hadronization corrections. Uncertainty on these calculation due to the renormalisation scale choice is shown as a hatched area around the NLO predictions corrected for the hadronization effects.

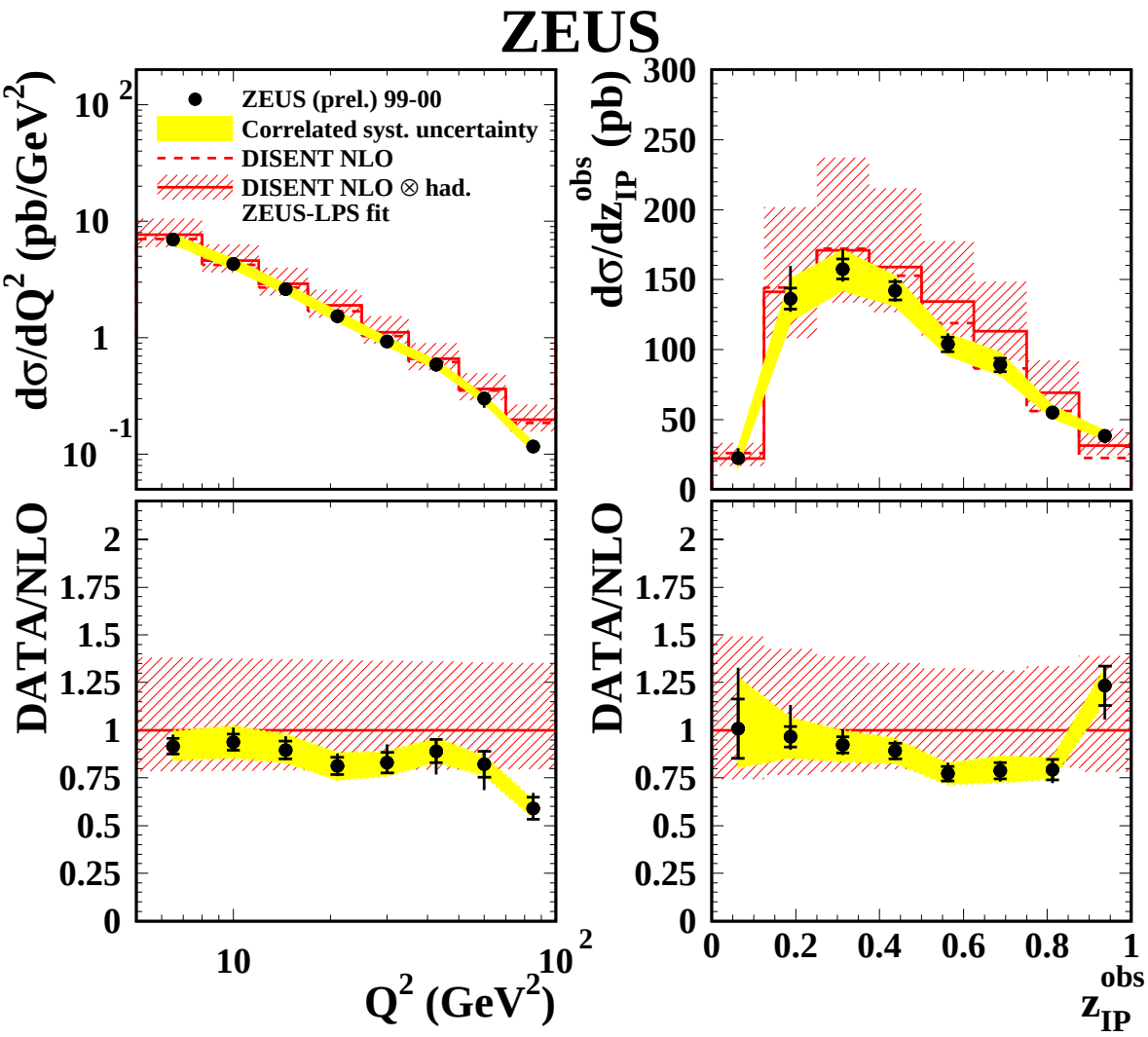

Figure 7.5: Comparisons between data and NLO QCD prediction from ZEUS-LPS fit in Q^2 and $z_{I\!P}^{\rm obs}$. The upper plots show the cross sections compared to the NLO QCD prediction, while the lower plots show the ratio of data cross sections over NLO prediction from ZEUS-LPS fit. The shaded band represents the correlated error. The solid lines represent NLO cross sections from ZEUS-LPS fit.

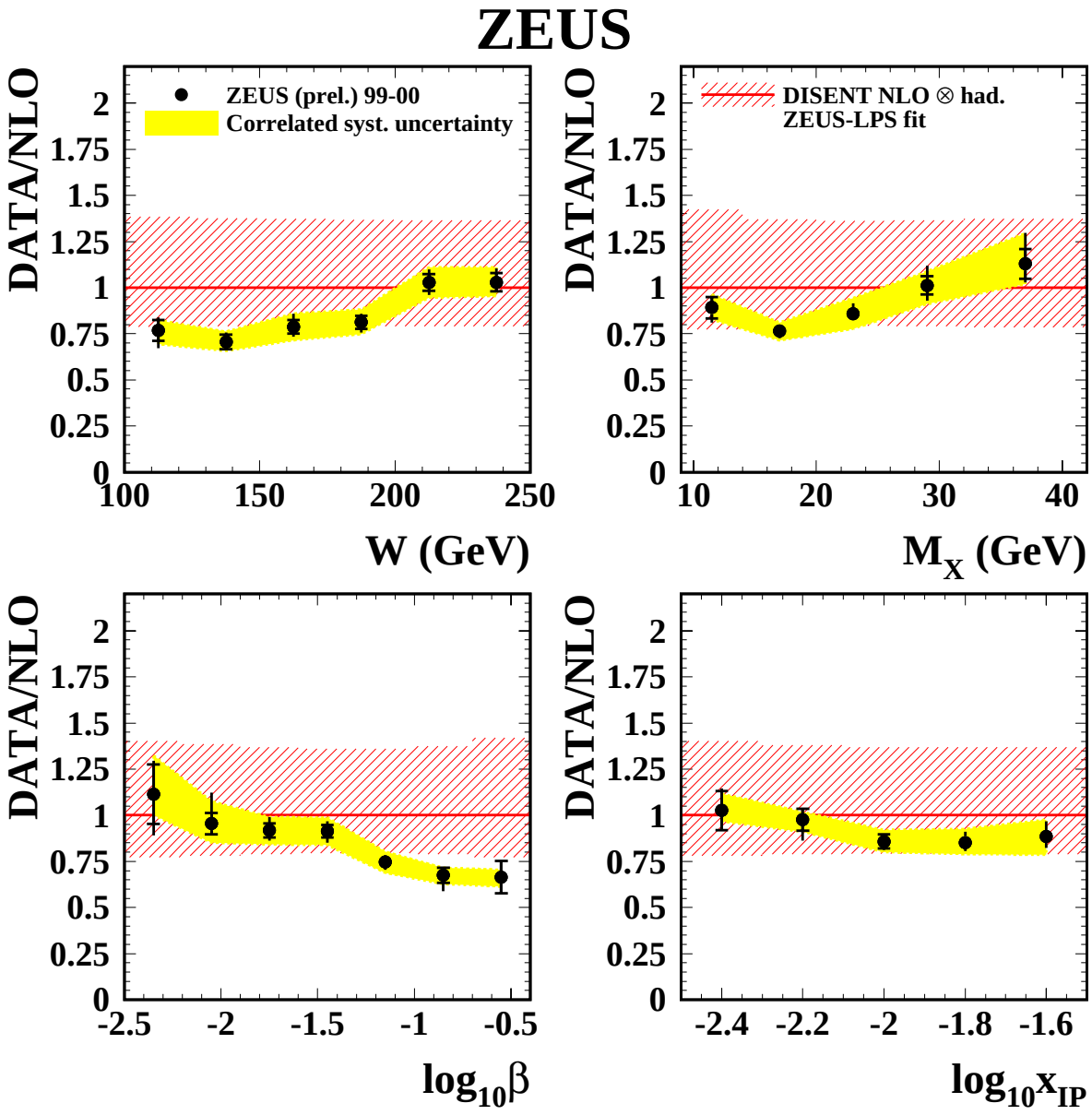

Figure 7.6: Comparisons between data and NLO QCD prediction from ZEUS-LPS fit in W, M_X, $\log_{10}\beta$ and $\log_{10} x_{I\!P}$. The upper plots show the cross sections compared to the NLO QCD prediction, while the lower plots show the ratio of data cross sections over NLO prediction from ZEUS-LPS fit. The shaded band represents the correlated error. The solid lines represent NLO cross sections from ZEUS-LPS fit.

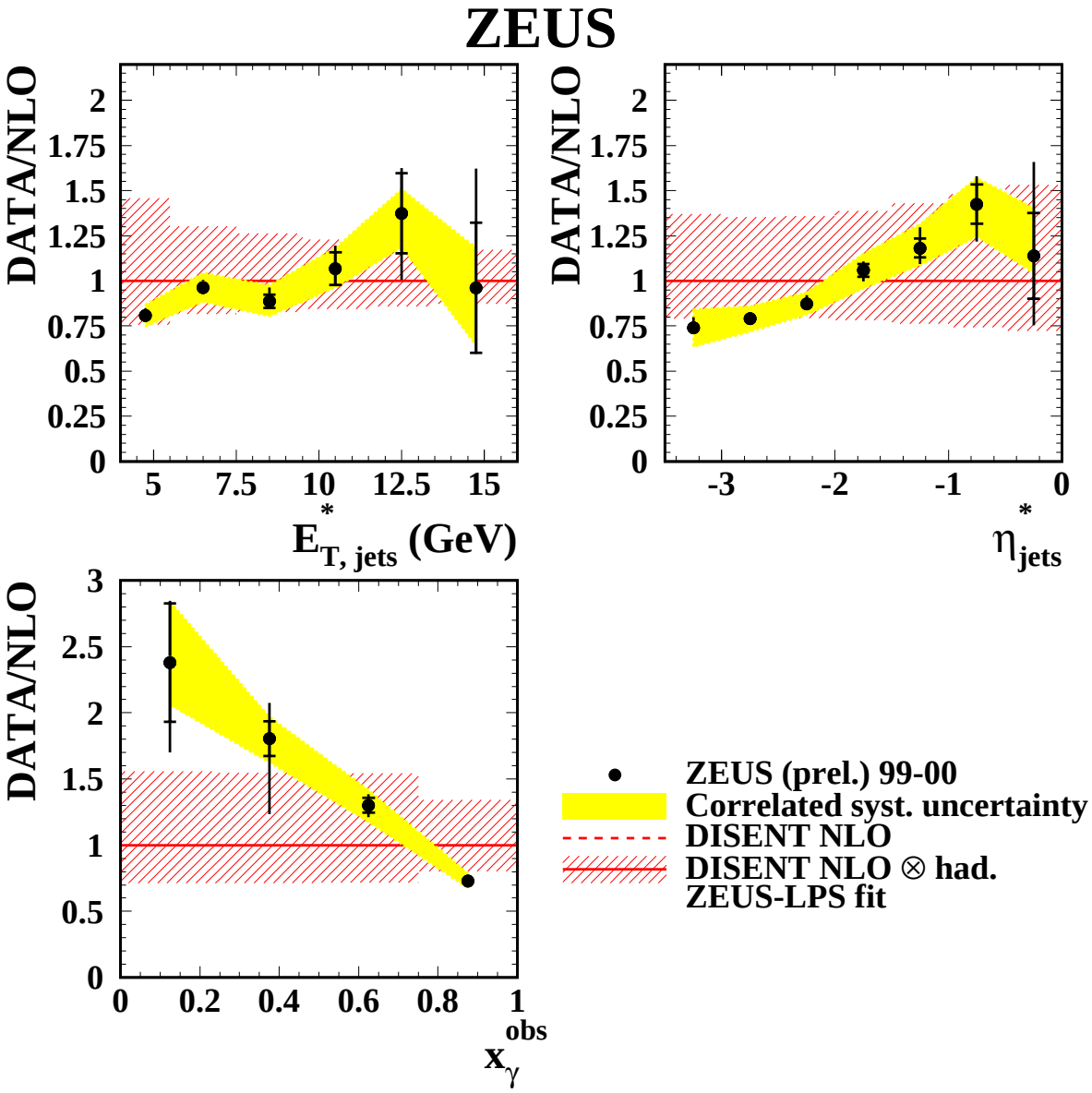

Figure 7.7: Comparisons between data and NLO QCD prediction from ZEUS-LPS fit in $E^*_{T,\text{jets}}$, η^*_{jets} and x_γ^{obs}. The upper plots show the cross sections compared to the NLO QCD prediction, while the lower plots show the ratio of data cross sections over NLO prediction from ZEUS-LPS fit. The shaded band represents the correlated error. The solid lines represent NLO cross sections from ZEUS-LPS fit.

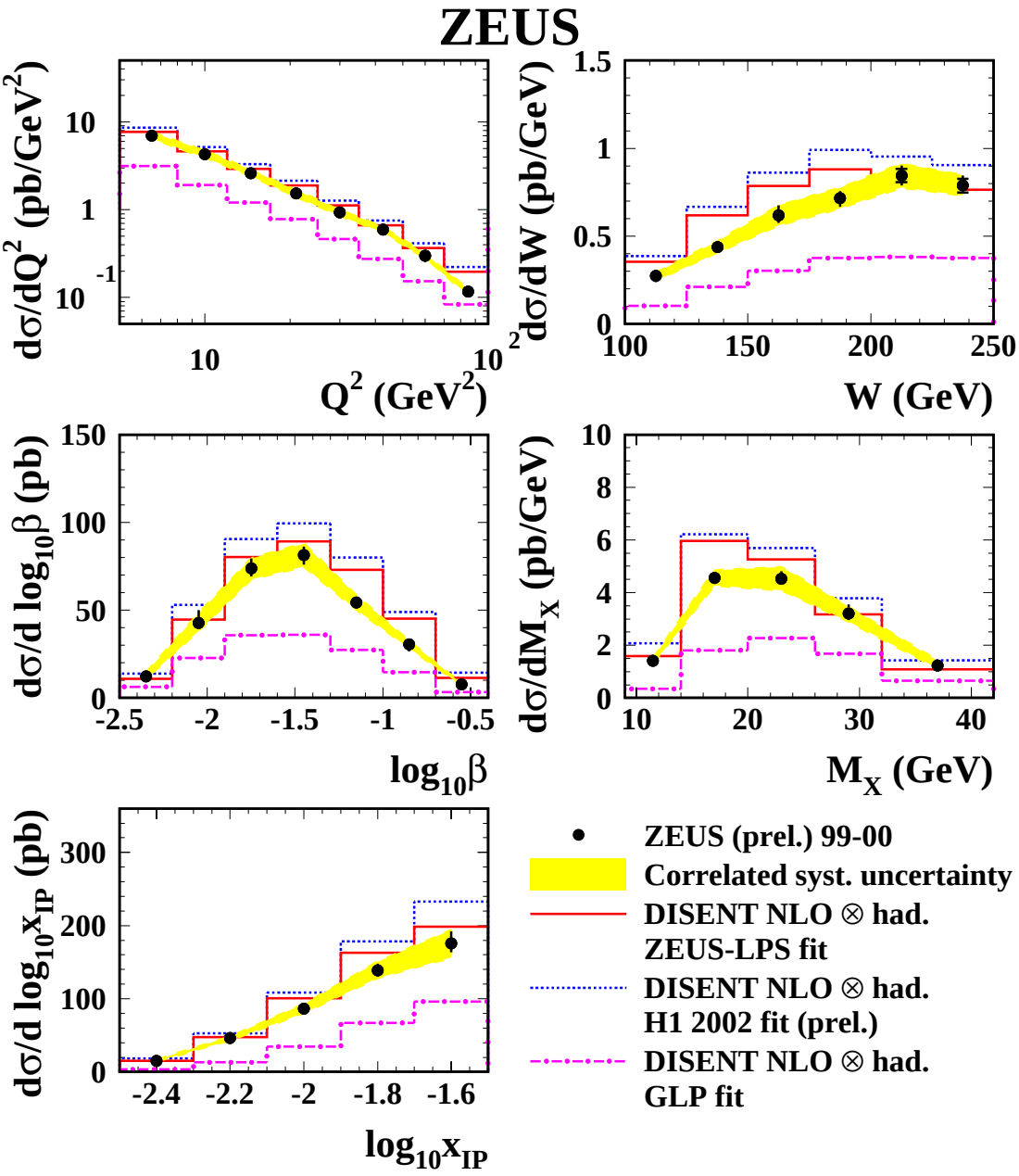

Figure 7.8: The cross sections in Q^2, W, $\log_{10}\beta$, M_X and $\log_{10} x_{I\!P}$ compared to the three NLO QCD predictions. The diffractive PDFs from ZEUS-LPS fit, H1 2002 fit and GLP fit are used for NLO predictions. The data are shown as dots; the inner error bars represent the statistical uncertainty while the outer error bars represent the statistical and systematic uncertainties added in quadrature. The shaded band represents the correlated error.

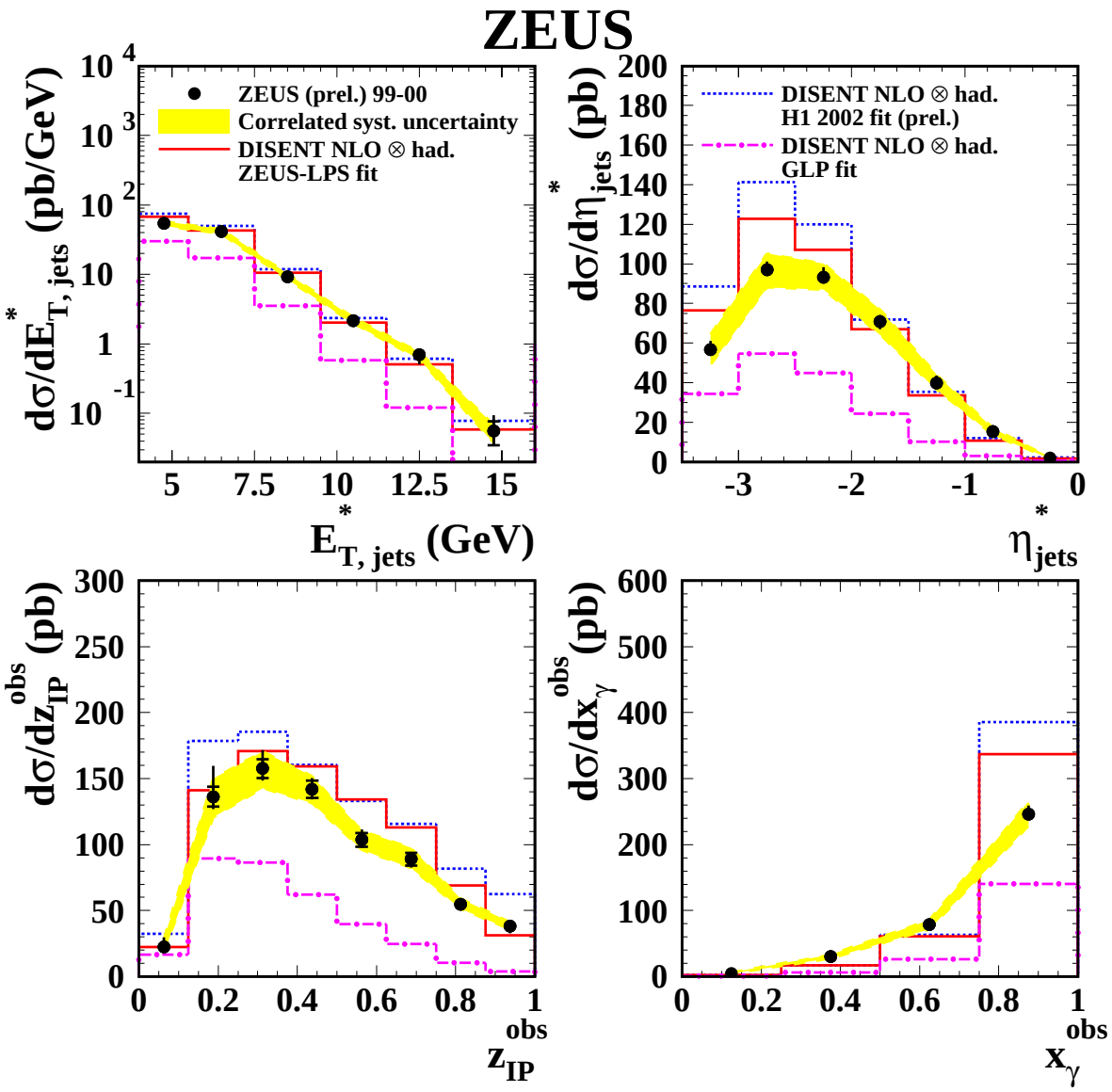

Figure 7.9: The cross sections in $E^*_{T,\mathrm{jets}}$, η^*_{jets}, $z_{I\!P}^{\mathrm{obs}}$ and x_γ^{obs} compared to the three NLO QCD predictions. The data are shown as dots; the inner error bars represent the statistical uncertainty while the outer error bars represent the statistical and systematic uncertainties added in quadrature. The shaded band represents the correlated error. The solid lines represent NLO cross sections from ZEUS-LPS fit, while NLO predictions from H1 2002 fit are drawn with a dotted line. The new predictions based on GLP fit are shown as a dash-dotted line.

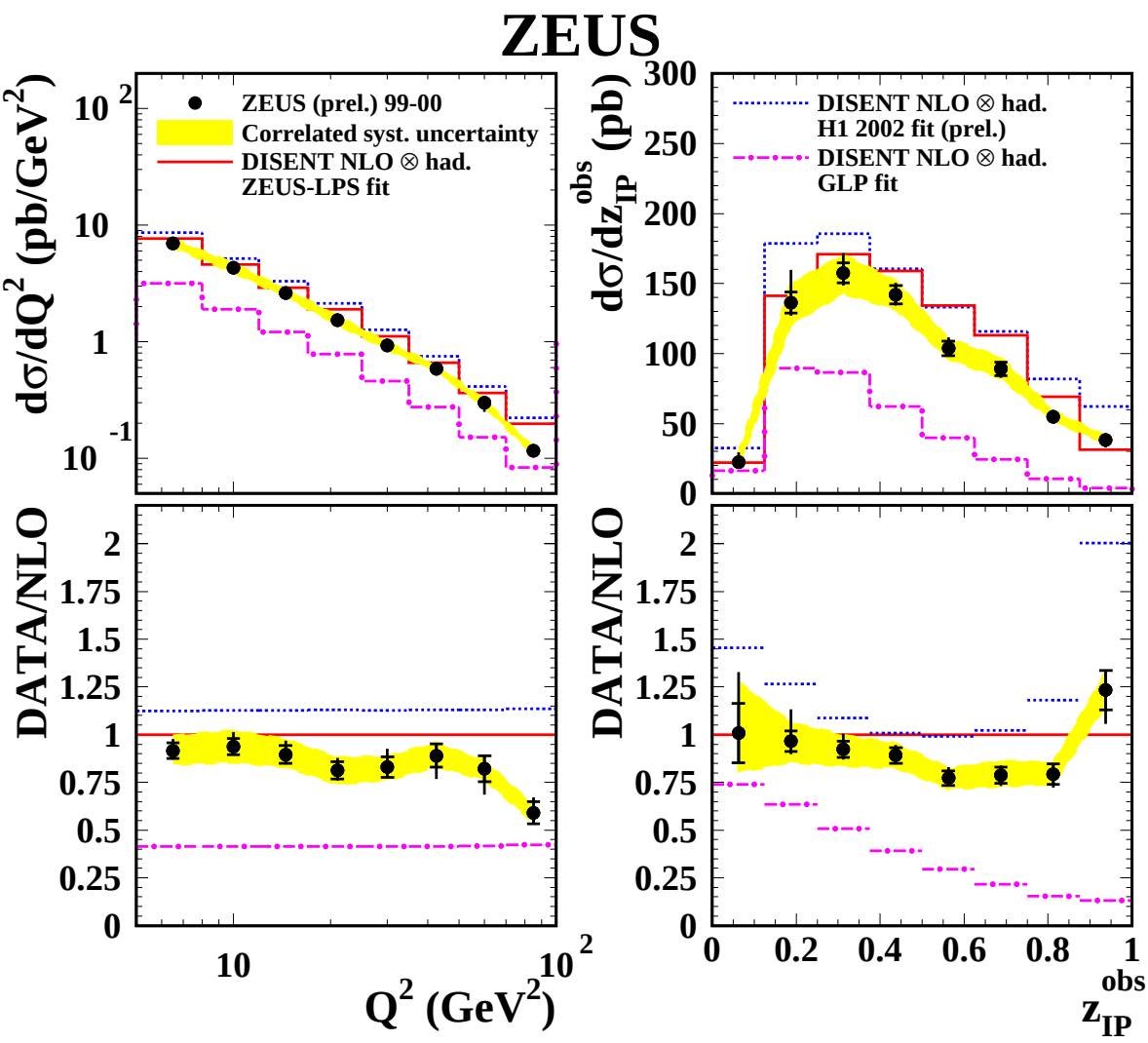

Figure 7.10: Comparisons between data and NLO QCD predictions in Q^2 and $z_{I\!P}^{\rm obs}$. The upper plots show the single differential cross sections compared to the three NLO QCD predictions, while the lower plots show the ratio of data cross sections over NLO predictions from ZEUS-LPS fit. The shaded band represents the correlated error. The solid lines represent NLO cross sections from ZEUS-LPS fit, while NLO predictions from H1 2002 fit are drawn with a dotted line. The new predictions based on GLP fit are shown as a dash-dotted line.

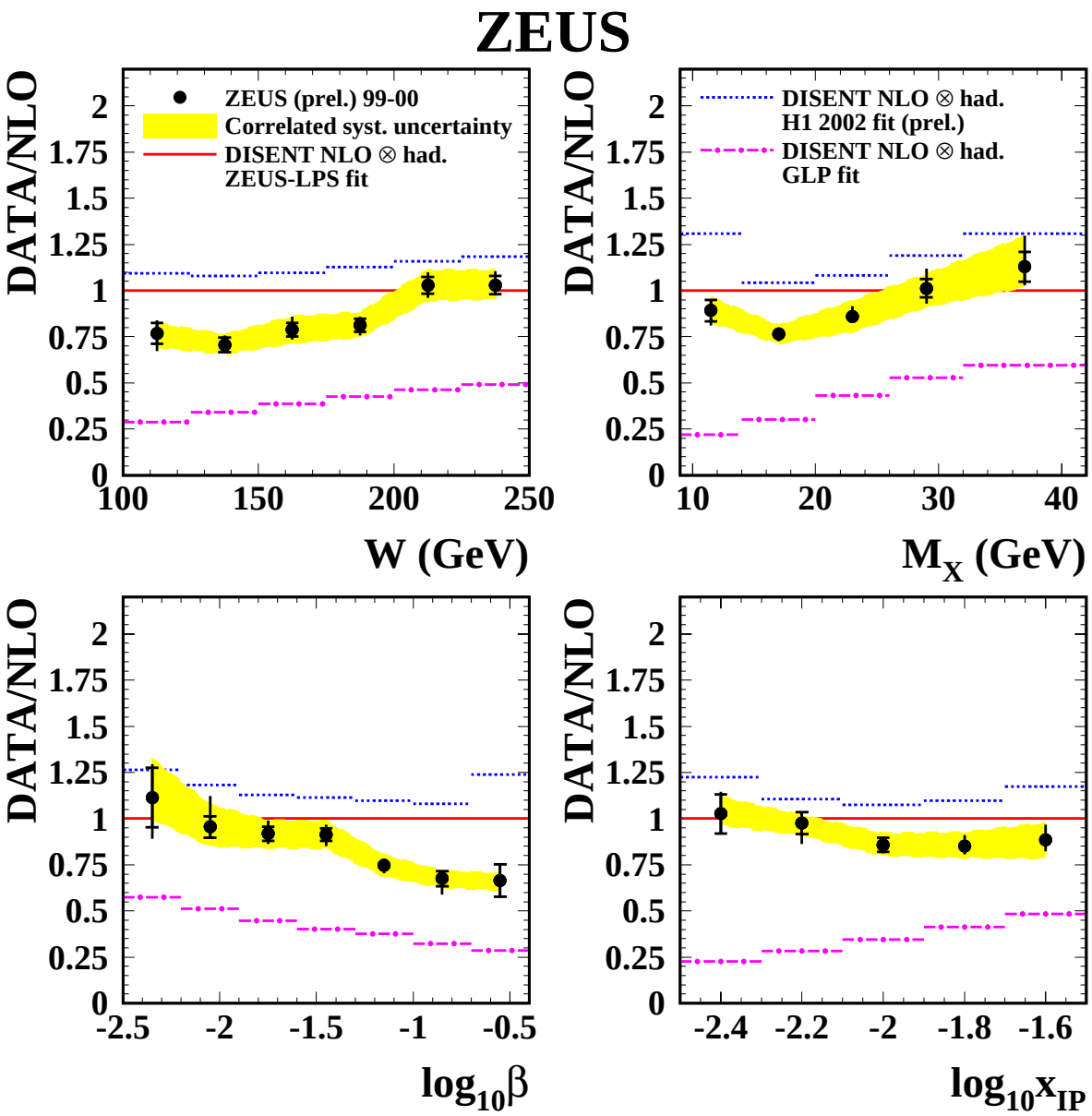

Figure 7.11: Comparisons between data and NLO QCD predictions in W, M_X, $\log_{10}\beta$ and $\log_{10} x_{I\!P}$. The upper plots show the cross sections compared to the three NLO QCD predictions, while the lower plots show the ratio of data cross sections over NLO predictions from ZEUS-LPS fit. The shaded band represents the correlated error. The solid lines represent NLO cross sections from ZEUS-LPS fit, while NLO predictions from H1 2002 fit are drawn with a dotted line. The new predictions based on GLP fit are shown as a dash-dotted line.

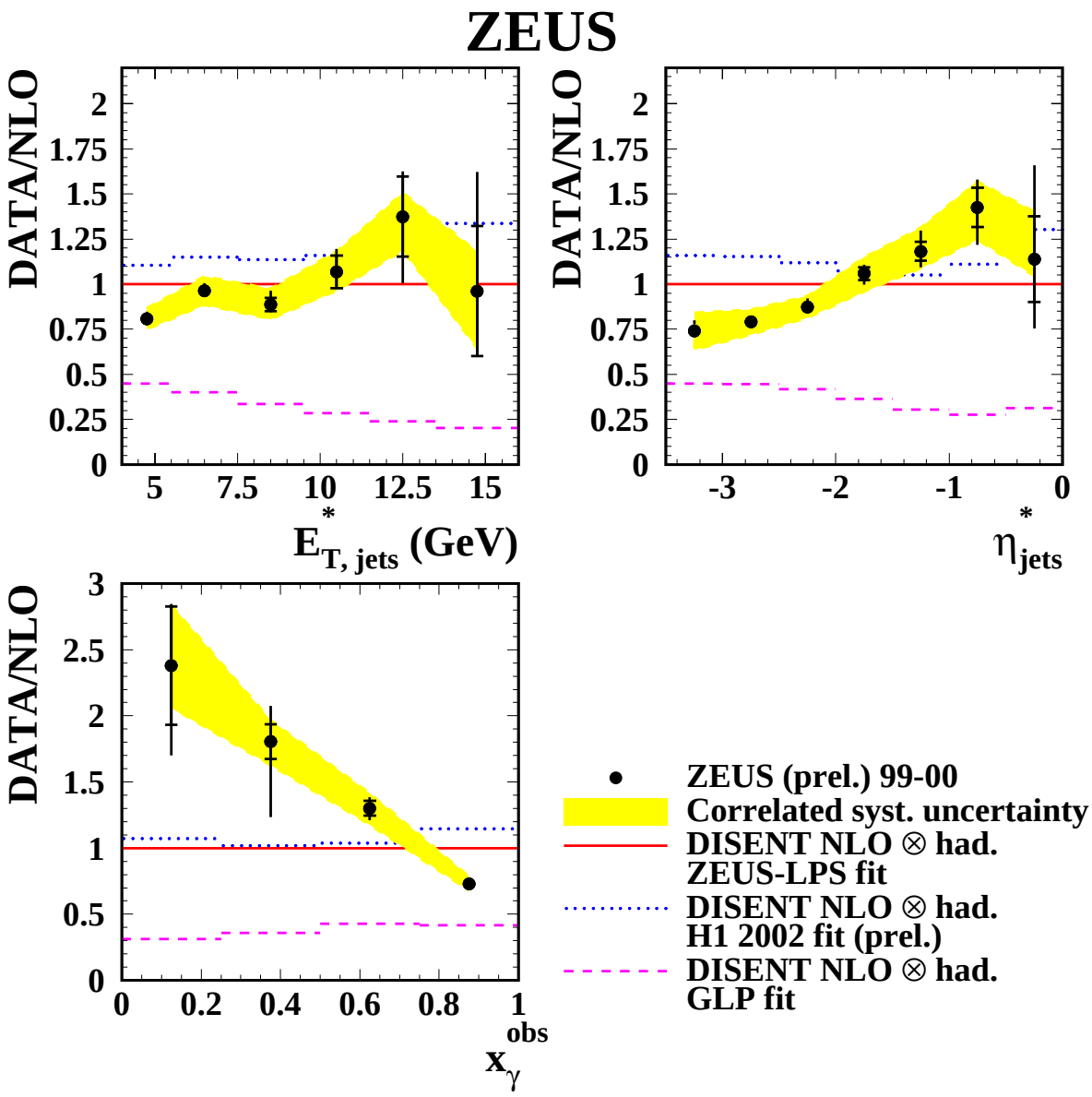

Figure 7.12: Comparisons between data and NLO QCD predictions in $E^*_{T,\text{jets}}$, η^*_{jets} and x_γ^{obs}. The upper plots show the single differential cross sections compared to the three NLO QCD predictions, while the lower plots show the ratio of data cross sections over NLO predictions from ZEUS-LPS fit. The shaded band represents the correlated error. The solid lines represent NLO cross sections from ZEUS-LPS fit, while NLO predictions from H1 2002 fit are drawn with a dotted line. The new predictions based on GLP fit are shown as a dash-dotted line.

Chapter 8

Conclusions

The cross sections of dijet processes in diffractive DIS have been measured using $e^- p$ and $e^+ p$ data taken by ZEUS detector in year 1999–2000. The cross sections are measured in the following kinematic range; $5 < Q^2 < 100$ GeV^2, $100 < W < 250$ GeV, $x_{I\!P} < 0.03$, $N^*_{\rm jets} \geq 2$, $E^*_{T,{\rm jet1}} > 5$ GeV, $E^*_{T,{\rm jet2}} > 4$ GeV, and $-3.5 < \eta^*_{\rm jet} < 0$. Jets are reconstructed with the inclusive k_T algorithm in γ^*-p frame. The cross sections of dijet in diffractive DIS are measured as functions of Q^2, W, $\log_{10} x_{I\!P}$, $\log_{10} \beta$, $E^*_{T,{\rm jets}}$, $\eta^*_{\rm jets}$, M_X, $z^{\rm obs}_{I\!P}$ and $x^{\rm obs}_\gamma$.

These cross sections are compared with two kinds of the leading-order (LO) Monte Carlo predictions; the resolved pomeron model and a model based on QCD. The resolved pomeron models the jet production through a parton-parton collision between the pomeron and the virtual photon. Another model produces jets through two gluon interactions between the proton and the photon based on QCD. Both models reproduced data reasonably well.

The cross sections are also compared to the next-to-leading order (NLO) QCD predictions with three different diffractive parton density functions (PDFs) extracted from different HERA F_2^D measurements. They are the H1 2002 fit which is extracted from the H1 F_2^D data, the ZEUS-LPS fit which is extracted from the diffractive events with ZEUS Leading Proton Spectrometer and the charm contribution to F_2^D, and the GLP fit which is extracted from the ZEUS F_2^D data with the M_X method. The NLO prediction with the ZEUS-LPS fit describes the data better than the other PDFs. The NLO prediction with GLP fit underestimates data by about a factor of 2. At high $z^{\rm obs}_{I\!P}$, the amount of gluon density for GLP fit is smaller than other two diffractive PDF fits.

From the comparison to three different diffractive PDFs, one could conclude that the measured dijet cross sections show the significant contribution of the gluon in the pomeron, especially at high $z^{\rm obs}_{I\!P}$ region. A better diffractive PDFs can be extracted by including these measured cross sections to the global NLO QCD fit.

Appendix A

Trigger selection

A.1 FLT

This analysis used many trigger logics, slot 23, slot 28, slot 30, slot 40, slot 41, slot 43, slot 44, slot 46, slot 47, slot 50 in order to take the DIS events. For the Q^2 range of this analysis ($5 < Q^2 < 100$ GeV^2), almost all the events pass the logic of slot 30, which requires the following condition:

- At least one isolated electron candidate in RCAL region,
- Energy deposit in CAL
  $E_{\rm EMC}^{\rm RCAL\ exc.\ 1st\ IR} > 2032$ MeV or $E_{\rm EMC}^{\rm RCAL} > 3750$ MeV or $E^{\rm CAL} > 464$ MeV,
- Veto condition on the timing information measured by C5, VETO and SRTD,

where $E_{\rm EMC}^{\rm RCAL\ exc.\ 1st\ IR}$ is the energy of RCAL EMC section excluding the first inner ring of CAL tower, $E_{\rm EMC}^{\rm RCAL}$ is the energy of RCAL EMC section, and $E^{\rm CAL}$ is the energy sum of HAC and EMC sections excluding the first three inner rings of FCAL towers and the first inner ring of RCAL tower.

A.2 SLT

The SLT required the following conditions.

- $E_{\rm EMC}^{\rm RCAL} > 2.5$ GeV or $E_{\rm EMC}^{\rm BCAL} > 2.5$ GeV or $E_{\rm EMC}^{\rm FCAL} > 10$ GeV or $E_{\rm HAC}^{\rm FCAL} > 10$ GeV
- $E - p_Z + 2E_\gamma > 24$ GeV

where $E_{\rm EMC}^{\rm RCAL}$ is the energy of RCAL EMC section, $E_{\rm EMC}^{\rm BCAL}$ is the energy of BCAL EMC section, $E_{\rm EMC}^{\rm FCAL}$ is the energy of FCAL EMC section, $E_{\rm HAC}^{\rm FCAL}$ is the energy of FCAL HAC section, $E - p_Z$ is the total $E - p_Z$ measured in CAL, and E_γ is the energy of the photon calorimeter of the luminosity monitors.

A.3 TLT

The TLT for the $e^- p$ data required the following conditions.

- 30 GeV $< E - p_Z <$ 100 GeV
- $E_{e'} > 7$ GeV
- The electron was found in RCAL and the position of the electron candidate was outside of $-12 < X < 12$ cm and $-6 < Y < 6$ cm.
- $Q^2_{\rm el} > 2$ GeV

where $E_{e'}$ is the energy of the electron candidate and $Q^2_{\rm el}$ is the Q^2 calculated by the electron method: $Q^2_{\rm el} = 2E_e E_{e'}(1 + \cos\theta_e)$, where E_e is the electron beam energy and θ_e is the polar angle of the electron candidate.

The TLT for the $e^+ p$ data required the following conditions.

- $E - p_Z > 30$ GeV
- $E_{e'} > 4$ GeV
- The electron was found in RCAL and the position of the electron candidate was outside of $-12 < X < 12$ cm and $-6 < Y < 6$ cm.
- $E_{\rm FPC} < 20$ GeV

where $E_{e'}$ is the energy of the electron candidate and $E_{\rm FPC}$ is the energy of FPC detector. This trigger was designed to take the events with a rapidity gap in the FPC region: $3.8 < \eta < 5$.

Appendix B

Systematic uncertainties

The systematic uncertainties of the measured cross sections of dijets in diffractive DIS as functions of Q^2, W, $\log_{10} x_{I\!P}$, $\log_{10} \beta$, $E^*_{T,\text{jets}}$, η^*_{jets}, M_X, $z^{\text{obs}}_{I\!P}$ and x^{obs}_{γ} are estimated. Each source of the systematic uncertainties for each kinematic variable is shown on Figure B.1–B.9.

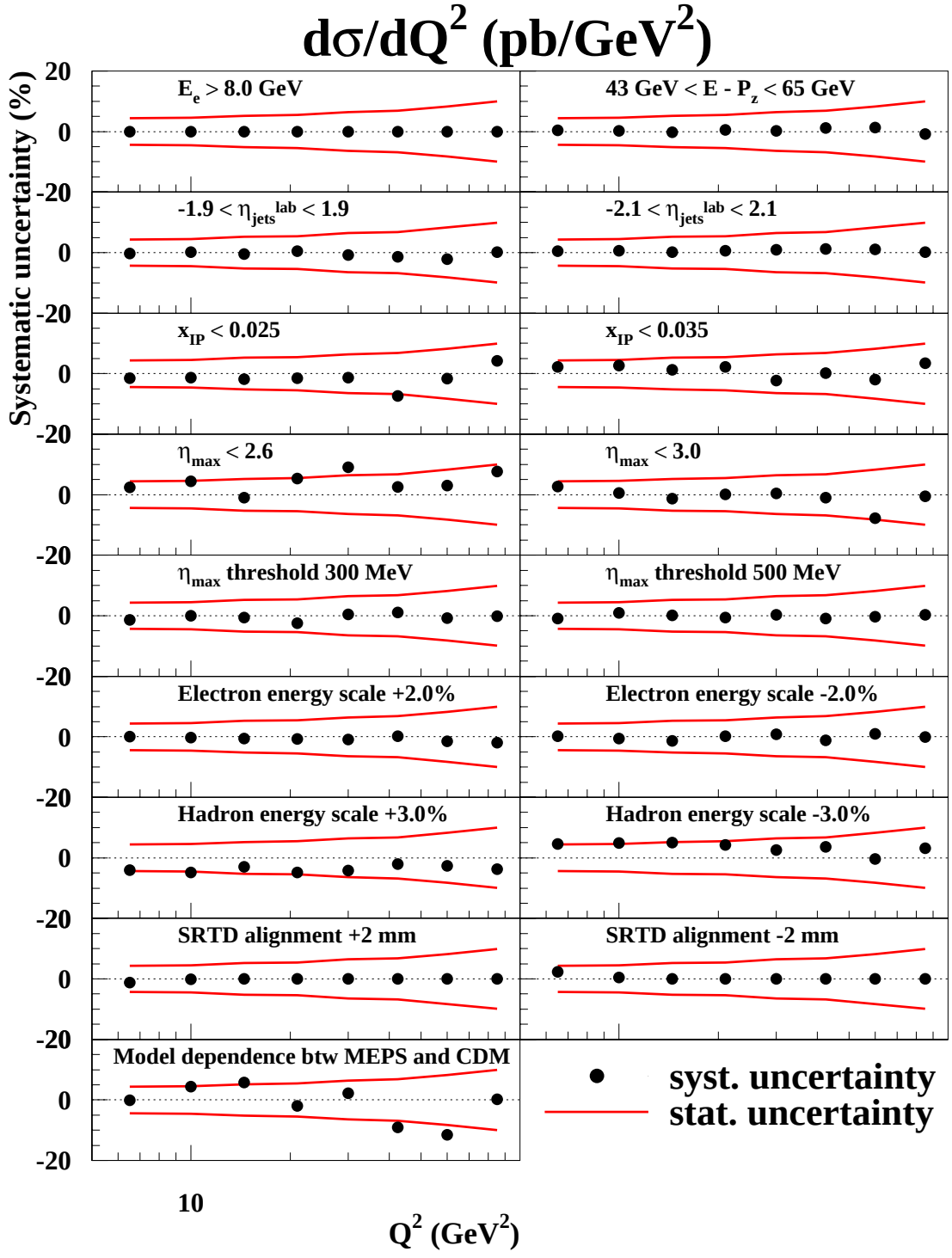

Figure B.1: The systematic uncertainties for $d\sigma/dQ^2$. The points show systematic uncertainties, while the lines are statistical uncertainties.

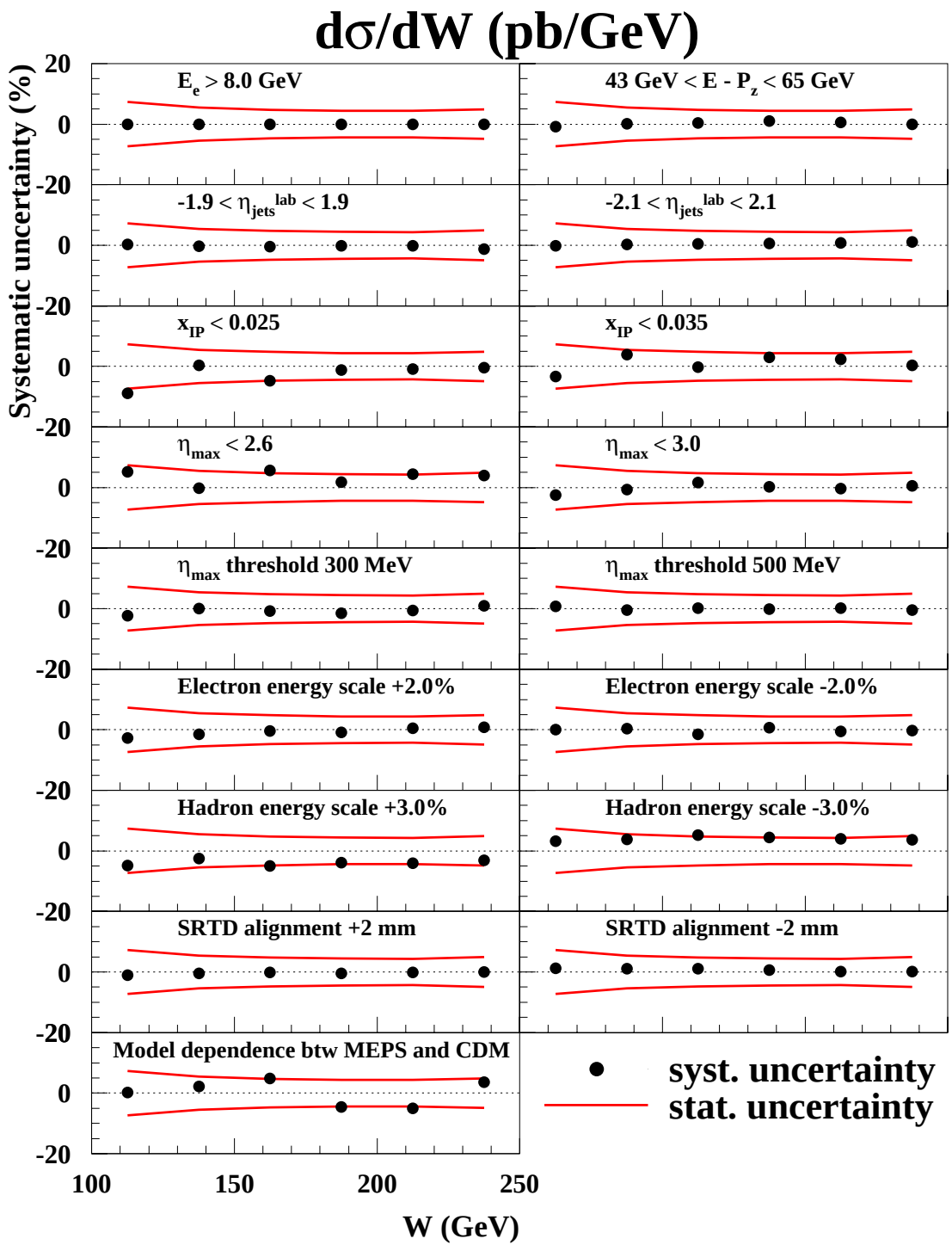

Figure B.2: The systematic uncertainties for $d\sigma/dW$. The points show systematic uncertainties, while the lines are statistical uncertainties.

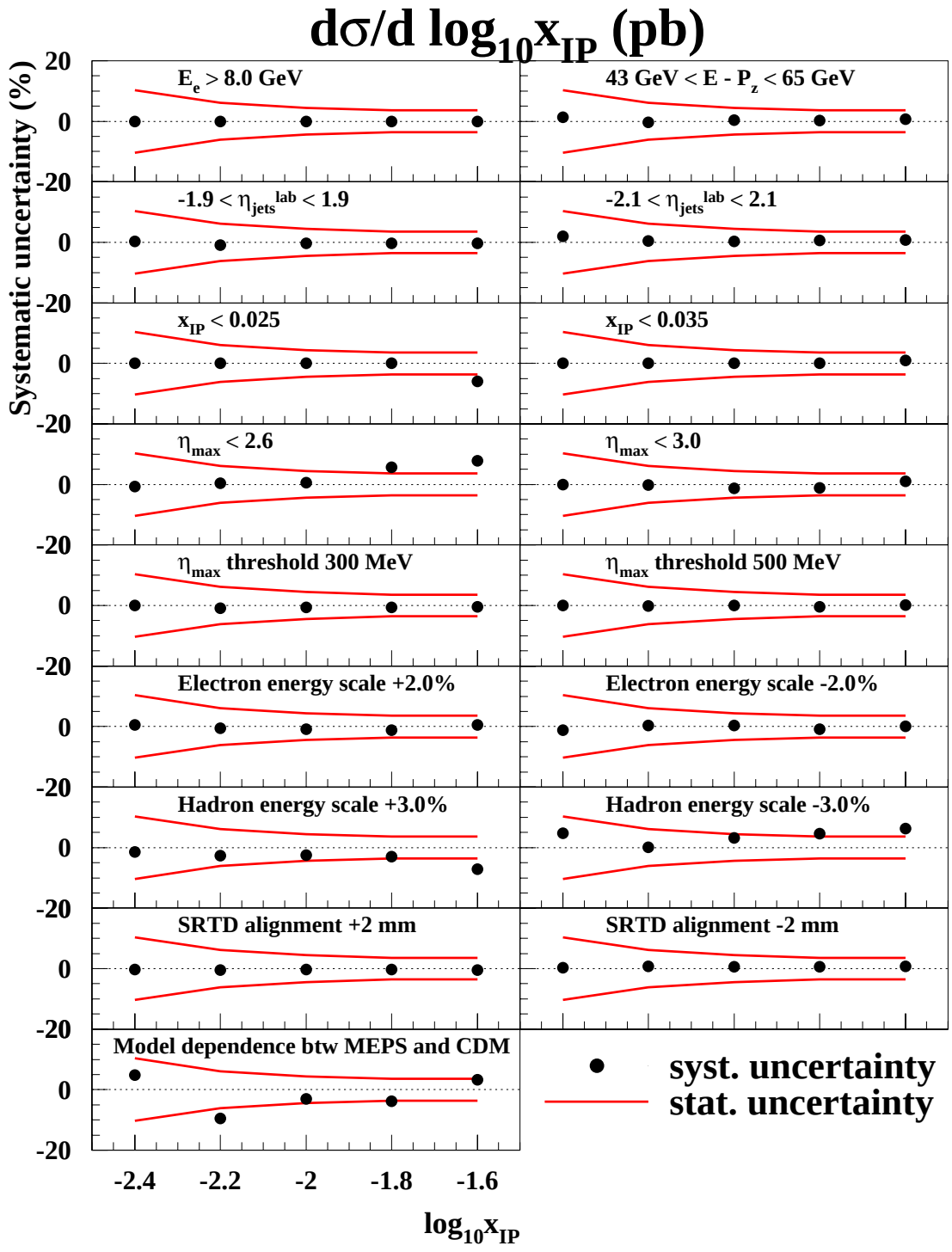

Figure B.3: The systematic uncertainties for $d\sigma/d\log_{10} x_{I\!P}$. The points show systematic uncertainties, while the lines are statistical uncertainties.

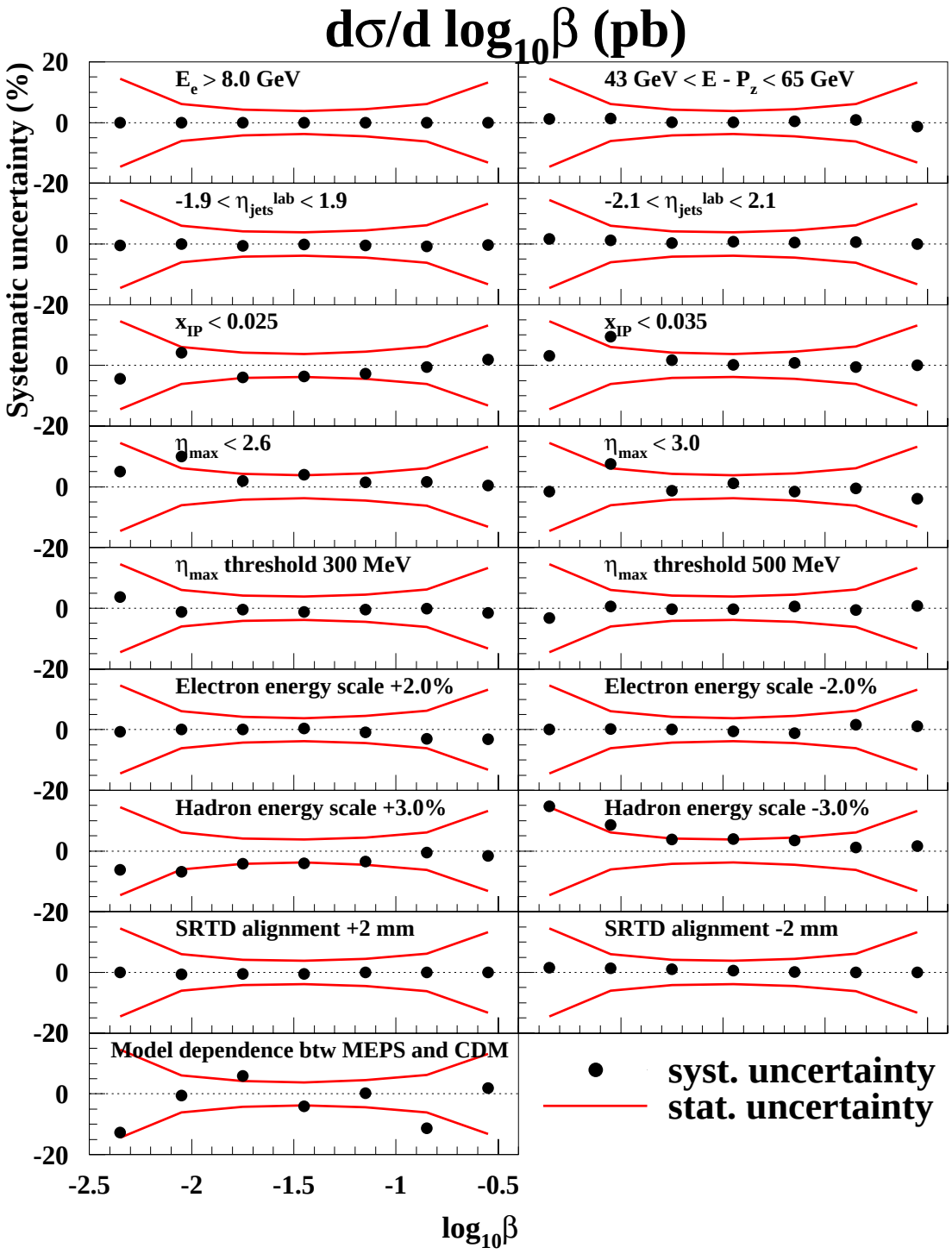

Figure B.4: The systematic uncertainties for $d\sigma/d\log_{10}\beta$. The points show systematic uncertainties, while the lines are statistical uncertainties.

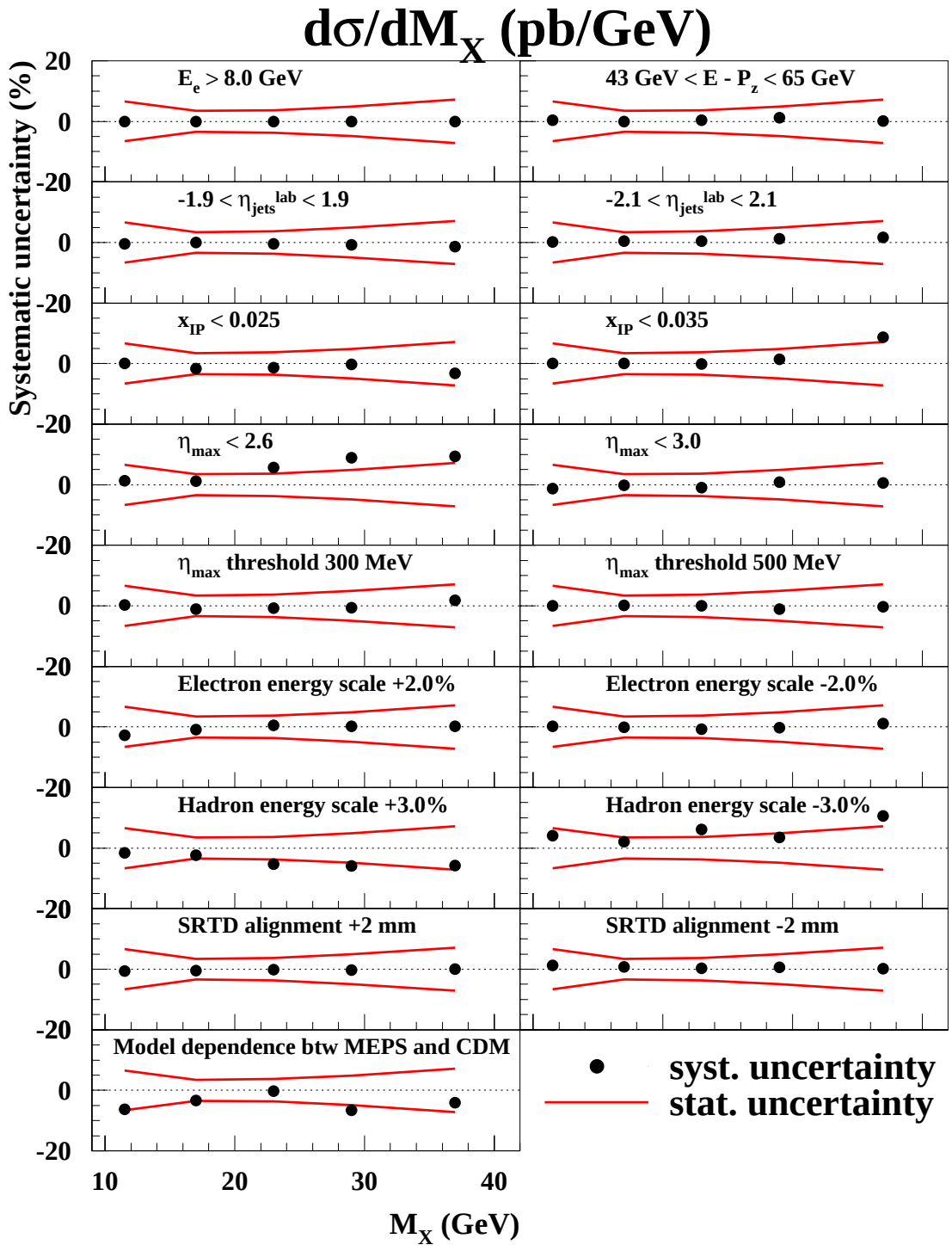

Figure B.5: The systematic uncertainties for $d\sigma/dM_X$. The points show systematic uncertainties, while the lines are statistical uncertainties.

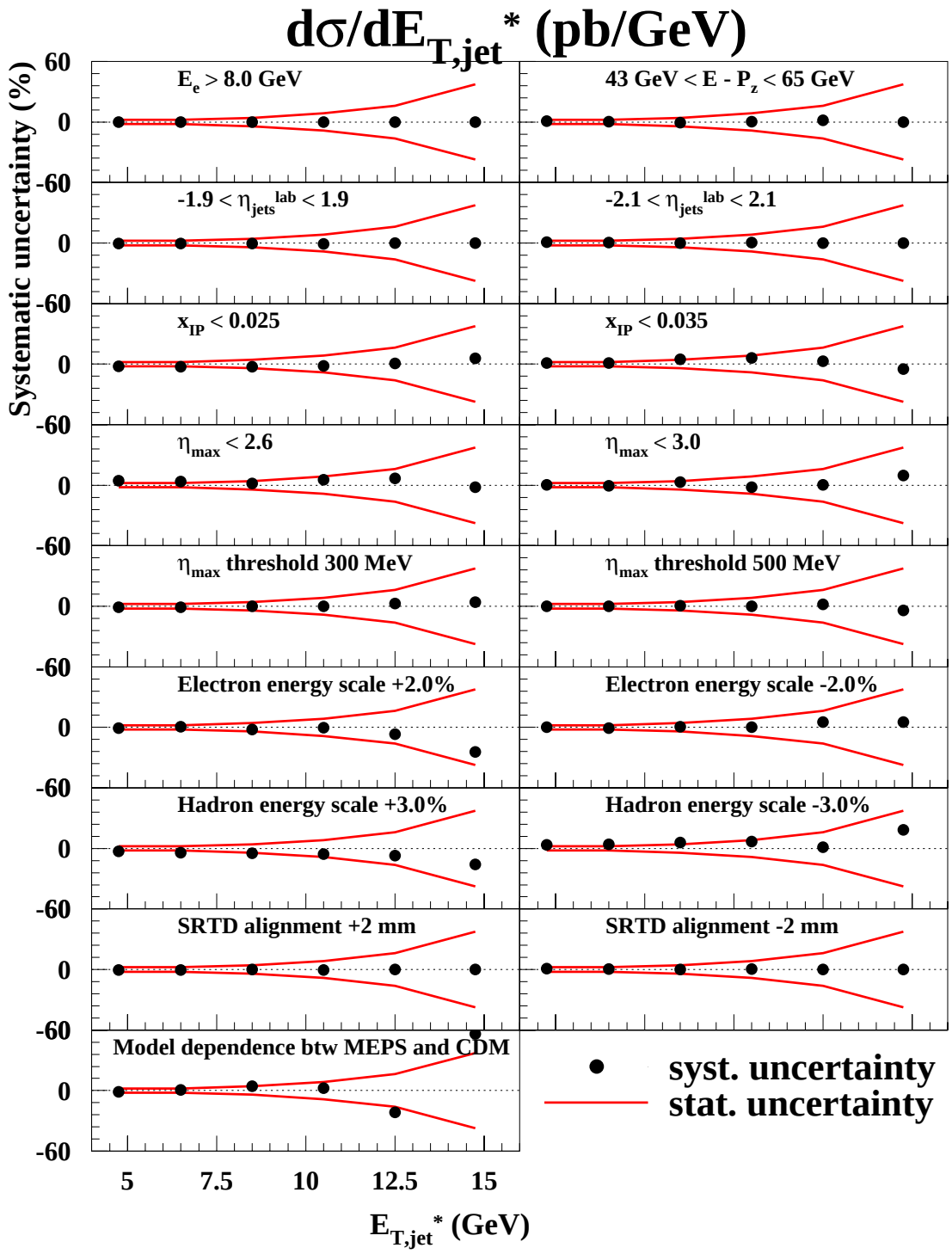

Figure B.6: The systematic uncertainties for $d\sigma/dE^*_{T,\mathrm{jets}}$. The points show systematic uncertainties, while the lines are statistical uncertainties.

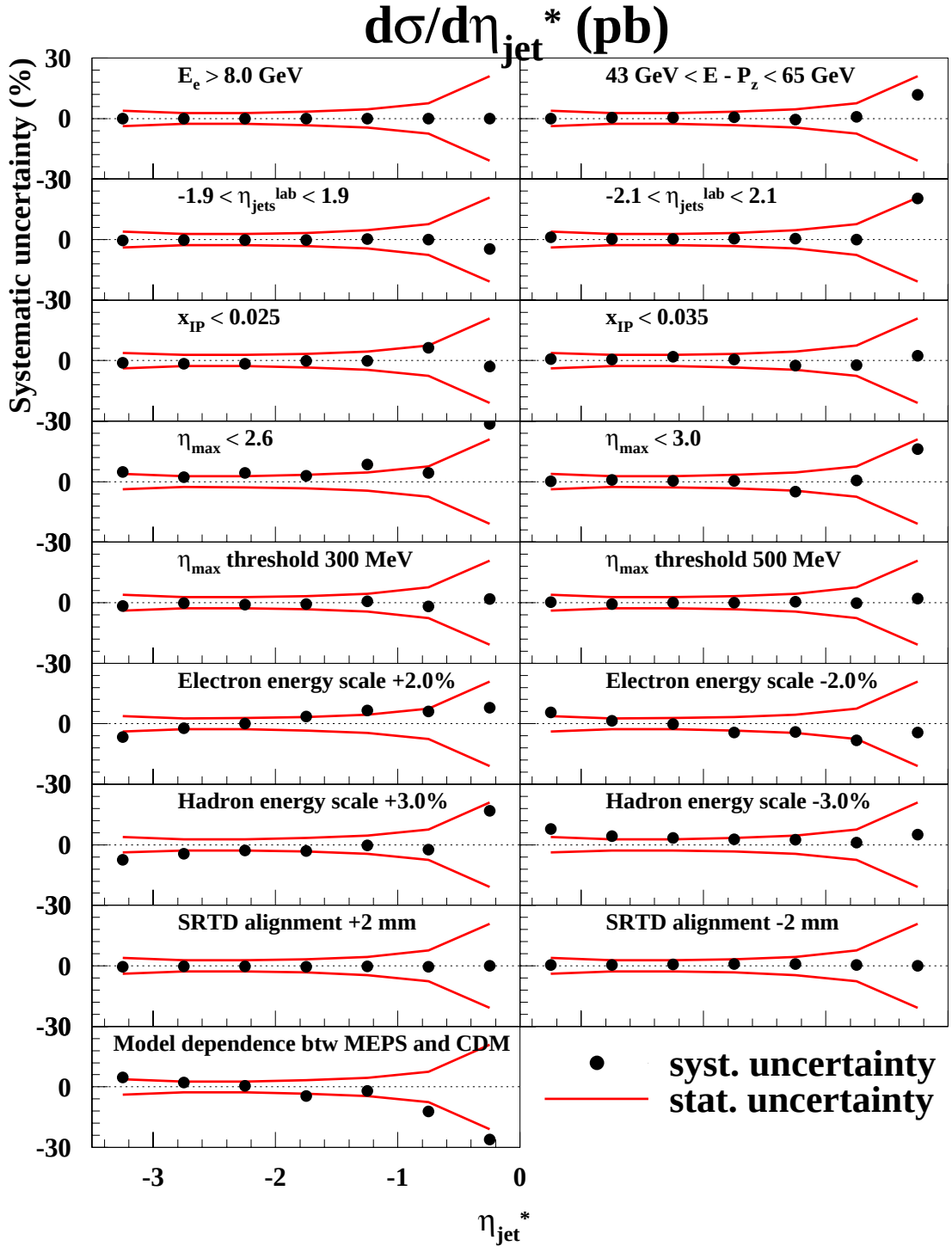

Figure B.7: The systematic uncertainties for $d\sigma/d\eta^*_{\rm jets}$. The points show systematic uncertainties, while the lines are statistical uncertainties.

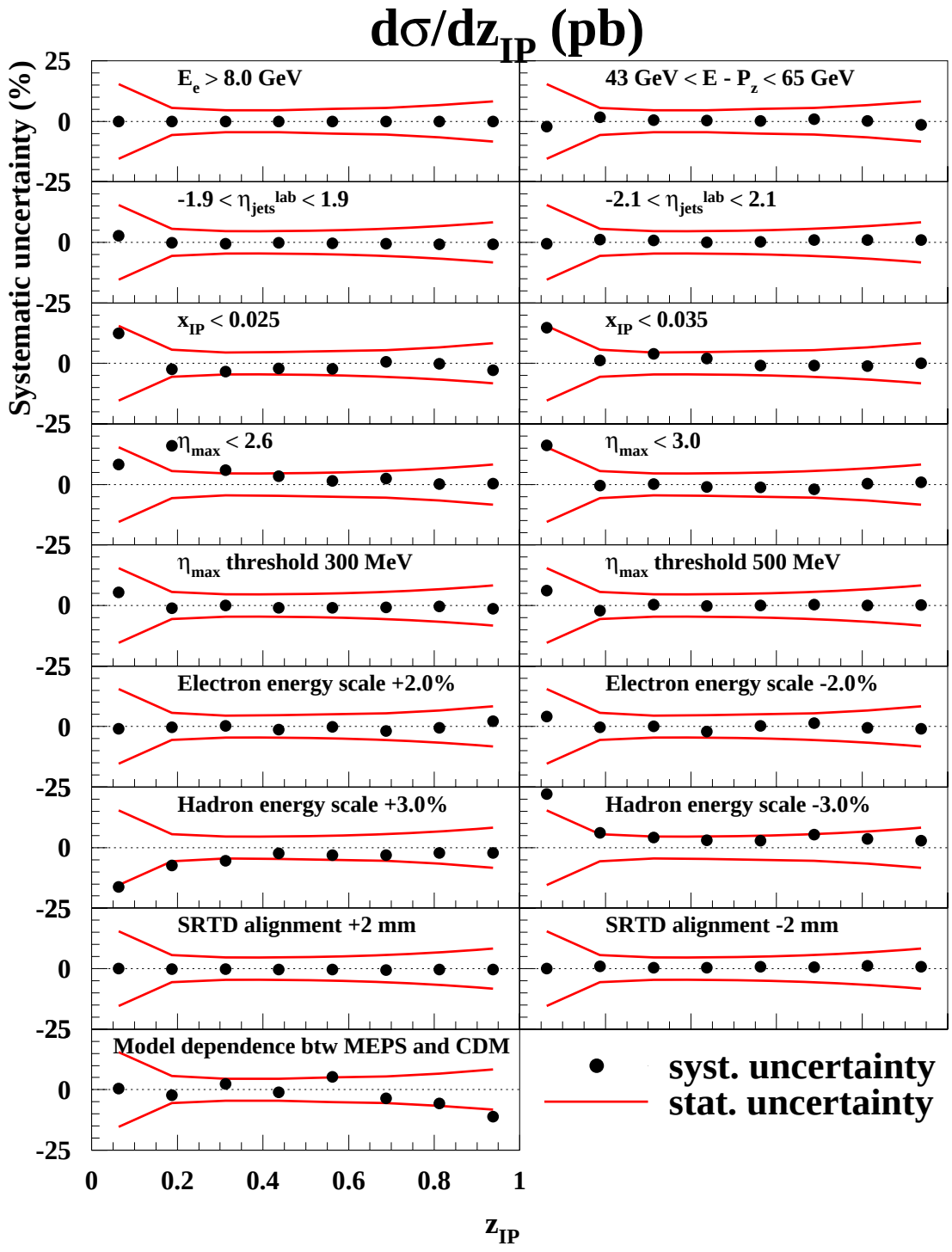

Figure B.8: The systematic uncertainties for $d\sigma/dz_{I\!P}^{\rm obs}$. The points show systematic uncertainties, while the lines are statistical uncertainties.

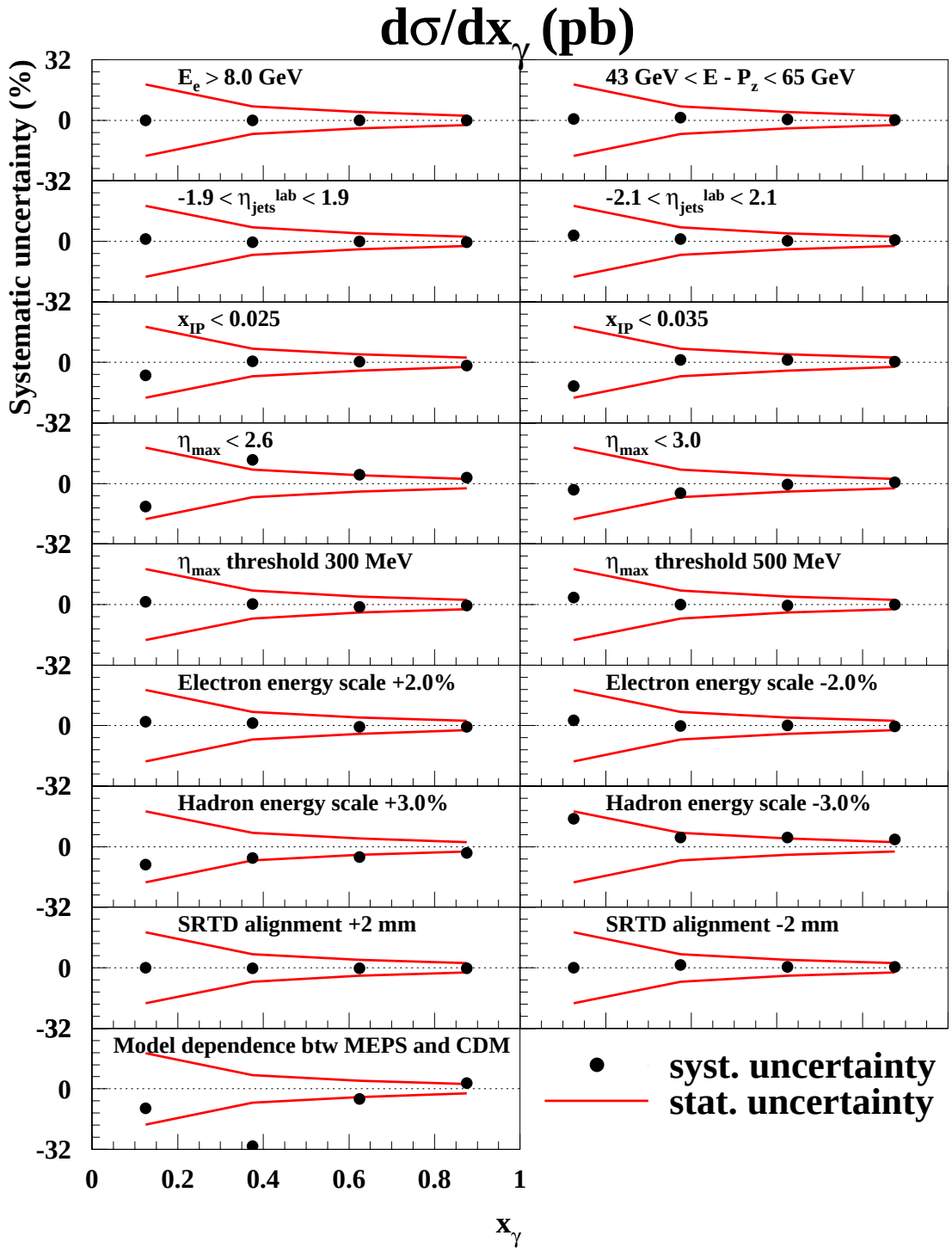

Figure B.9: The systematic uncertainties for $d\sigma/dx_\gamma^{\rm obs}$. The points show systematic uncertainties, while the lines are statistical uncertainties.

Bibliography

[1] P.D.B. Collins, *An Introduction to Regge Theory and High Energy Physics*. Cambridge University Press, 1977.

[2] A. Donnachie and P.V. Landshoff, Nucl. Phys. **B 231**, 189 (1984);
A. Donnachie and P.V. Landshoff, Phys. Lett. **B 296**, 227 (1992).

[3] G. Ingelman and P.E. Schlein, Phys. Lett. **B 152**, 256 (1985).

[4] UA8 Coll., A. Brandt et al., Phys. Lett. **B 211**, 239 (1988);
UA8 Coll., A. Brandt et al., Phys. Lett. **B 297**, 417 (1992).

[5] H1 Coll., T. Ahmed et al., Nucl. Phys. **B 429**, 477 (1994).

[6] ZEUS Coll., M. Derrick et al., Phys. Lett. **B 315**, 481 (1993).

[7] J. Collins, Phys. Rev. **D 57**, 3051 (1998);
J. Collins, J. Phys. **G 28**, 1069 (2002).

[8] V.N. Gribov and L.N. Lipatov, Sov. J. Nucl. Phys. **15**, 438 (1972).

[9] L.N. Lipatov, Sov. J. Nucl. Phys. **20**, 94 (1975).

[10] G. Altarelli and G. Parisi, Nucl. Phys. **B 126**, 298 (1977).

[11] H1 Coll., C. Adloff et al., Z. Phys. **C 74**, 221 (1997).

[12] H1 Coll., *Measurement and NLO DGLAP QCD Interpretation of Diffractive Deep-Inelastic Scattering at HERA*. Abstract 089, International Europhysics Conference on High Energy Physics, EPS03, 2003.

[13] ZEUS Coll., S. Chekanov et al., Eur. Phys. J. **C 38**, 43 (2004).

[14] ZEUS Coll., S. Chekanov et al., Phys. Rev. **D 69**, 012004 (2004).

[15] A. Donnachie and P.V. Landshoff, Nucl. Phys. **B 303**, 634 (1988).

[16] M. Groys, A. Levy and A. Proskuryakov, *Proc. HERA AND THE LHC, A workshop on the implications of HERA for LHC physics, March 2004 - March 2005*, A. De Roeck (CERN) and H. Jung (DESY) (eds.), p. 499. CERN and DESY (2005). Also in preprint CERN-2005-014, DESY-PROC-2005-001 (hep-ph/0601013).

[17] ZEUS Coll., S. Chekanov et al., Nucl. Phys. **B 713**, 3 (2005).

[18] ZEUS Coll., S. Chekanov et al., Eur. Phys. J. **C 35**, 487 (2004).

[19] ZEUS Coll., U. Holm (ed.), *The ZEUS Detector*. Status Report (unpublished), DESY (1993), available on `http://www-zeus.desy.de/bluebook/bluebook.html`.

[20] N. Harnew et al., Nucl. Inst. Meth. **A 279**, 290 (1989);
B. Foster et al., Nucl. Phys. Proc. Suppl. **B 32**, 181 (1993);
B. Foster et al., Nucl. Inst. Meth. **A 338**, 254 (1994).

[21] R. Hall-Wilton et al., *The CTD Tracking Resolution* (unpublished). ZEUS-99-024, internal ZEUS-note, 1999.

[22] M. Derrick et al., Nucl. Inst. Meth. **A 309**, 77 (1991);
A. Andresen et al., Nucl. Inst. Meth. **A 309**, 101 (1991);
A. Caldwell et al., Nucl. Inst. Meth. **A 321**, 356 (1992);
A. Bernstein et al., Nucl. Inst. Meth. **A 336**, 23 (1993).

[23] ZEUS Coll., Calorimeter group, U. Behrens et al., Nucl. Inst. Meth. **A 289**, 115 (1990).

[24] ZEUS Coll., FPC group, A. Bamberger et al., Nucl. Inst. Meth. **A 450**, 235 (2000).

[25] ZEUS Coll., S. Chekanov et al., Eur. Phys. J. **C 21**, 443 (2001).

[26] A. Bamberger et al., Nucl. Inst. Meth. **A 401**, 63 (1997).

[27] J. Andruszków et al., Preprint DESY-92-066, DESY, 1992;
ZEUS Coll., M. Derrick et al., Z. Phys. **C 63**, 391 (1994);
J. Andruszków et al., Acta Phys. Pol. **B 32**, 2025 (2001).

[28] W. H. Smith, K. Tokushuku and L. W. Wiggers, *Proc. Computing in High-Energy Physics (CHEP), Annecy, France, Sept. 1992*, C. Verkerk and W. Wojcik (eds.), p. 222. CERN, Geneva, Switzerland (1992). Also in preprint DESY 92-150B.

[29] H. Jung, *The RAPGAP Monte Carlo for Deep Inelastic Scattering version 2.08/00*, 2001, available on `http://www.desy.de/~jung/rapgap/`.

[30] G. Ingelman, A. Edin and J. Rathsman, Comp. Phys. Comm. **101**, 108 (1997).

[31] A. Kwiatkowski, H. Spiesberger and H.-J. Möhring, Comp. Phys. Comm. **69**, 155 (1992). Also in *Proc. Workshop Physics at HERA*, eds. W. Buchmüller and G.Ingelman, (DESY, Hamburg, 1991).

[32] T. Sjöstrand and M. Bengtsson, Comp. Phys. Comm. **43**, 367 (1987).

[33] B. Andersson et al., Phys. Rep. **97**, 31 (1983).

[34] H1 Coll., C. Adloff et al., Z. Phys. **C 76**, 613 (1997).

[35] M. Glück, E. Reya and A. Vogt, Phys. Rev. **D 45**, 3986 (1992);
M. Glück, E. Reya and A. Vogt, Phys. Rev. **D 46**, 1973 (1992).

[36] K. Golec-Biernat and M. Wüsthoff, Phys. Rev. **D 59**, 014017 (1999).

[37] K. Golec-Biernat and M. Wüsthoff, Phys. Rev. **D 60**, 114023 (1999).

[38] G. Gustafson and U. Pettersson, Nucl. Phys. **B 306**, 746 (1988).

[39] L. Lönnblad, Comp. Phys. Comm. **71**, 15 (1992).

[40] T. Sjöstrand, Comp. Phys. Comm. **82**, 74 (1994).

[41] K. Charchula, G.A. Schuler and H. Spiesberger, Comp. Phys. Comm. **81**, 381 (1994).

[42] M. Kasprzak, *Inclusive Properties of Diffractive and Non-diffractive Photoproduction at HERA*. Ph.D. Thesis, Warsaw University, Warsaw, Poland, Report DESY F35D-96-16, DESY, 1996.

[43] G. Marchesini et al., Comp. Phys. Comm. **67**, 465 (1992).

[44] R. Brun et al., GEANT3, Technical Report CERN-DD/EE/84-1, CERN, 1987.

[45] H. Abramowicz, A. Caldwell and R. Sinkus, Nucl. Inst. Meth. **A 365**, 508 (1995);
R. Sinkus and T. Voss, Nucl. Inst. Meth. **A 391**, 360 (1997).

[46] M. Wodarczyk, *Measurement of the F_2 Structure Function of the Proton at HERA from 1996 and 1997 ZEUS Data*. Ph.D. Thesis, University of Wisconsin, 1999.

[47] G.M. Briskin, *Diffractive Dissociation in ep Deep Inelastic Scattering*. Ph.D. Thesis, Tel Aviv University, Report DESY-THESIS 1998-036, 1998.

[48] S. Bentvelsen, J. Engelen and P. Kooijman, *Proc. Workshop on Physics at HERA*, W. Buchmüller and G. Ingelman (eds.), Vol. 1, p. 23. Hamburg, Germany, DESY (1992).

[49] T. Yamashita, *Study of Three-jet Production in ep Diffractive Deep Inelastic Scattering at HERA*. Ph.D. Thesis, University of Tokyo, Report KEK-REPORT-2002-1, 2002;
H. Lim, *Measurement of the diffractive cross section in deep inelastic ep scattering using the ZEUS Forward Plug Calorimeter at HERA*. Ph.D. Thesis, Kyungpook National University, 2002.

[50] S.Catani et al., Nucl. Phys. **B 406**, 187 (1993).

[51] S. D. Ellis and D. E. Soper, Phys. Rev. **D 48**, 3160 (1993).

[52] ZEUS Coll., S. Chekanov et al., Eur. Phys. J. **C 23**, 13 (2002).

[53] ZEUS Coll., S. Chekanov et al., Nucl. Phys. **B 672**, 3 (2003).

[54] S. Catani and M. H. Seymour, Nucl. Phys. **B 485**, 291 (1997). Erratum in Nucl. Phys **B 510**, 503 (1997);
S. Catani and M.H. Seymour, Nucl. Phys. **B 510**, 503 (1998).

[55] R.K. Ellis, D.A. Ross and A.E. Terrano, Nucl. Phys. **B178**, 421 (1981).

[56] M. Botje, *QCDNUM version 16.12* (unpublished), available on `http://www.nikhef.nl/~h24/qcdcode/index.html`.